공학박사학위논문

Computational models and methods for solving slot coating flow problems

슬롯 코팅 유동 문제 해결을 위한 전산 모사 모델 및 기법

2023년 8월

서울대학교 대학원

화학생물공학부

곽 형 렬

Computational models and methods for solving slot coating flow problems

슬롯 코팅 유동 문제 해결을 위한 전산 모사 모델 및 기법

지도교수 남재욱

이 논문을 공학박사 학위논문으로 제출함

2023년 8월

서울대학교 대학원

화학생물공학부

곽형렬

곽형렬의 공학박사 학위 논문을 인준함

2023년 6월

위원장	안경현	(인)
부위원장	남재욱	(인)
위원	이원보	(인)
위원	최장욱	(인)
위원	김동재	(인)

Abstract

Computational models and methods for solving slot coating flow problems

Hyungyeol Kwak
School of Chemical and Biological Engineering
The Graduate School
Seoul National University

Slot coating process is a high-precision method for depositing a thin layer of liquid film onto a moving substrate. Owing to its versatility, slot coating process has been employed by many industries for manufacturing a wide range of high-value film products including optical films, solar cells, and battery electrodes. The process consists of three main stages: solution preparation, application, and drying. In this study, we focus mainly on the slot coating flow, or the coating flow that occurs during the application step.

Slot coating flow is a two-dimensional flow with two liquid-gas interfaces that bound the flow domain. There are many adjustable parameters associated with the flow, and it is only through an adequate control over these parameters, that it is possible to maintain a stable coating flow and produce defect-free films. The answer to choosing the right values for the parameters comes from solving slot coating flow problems.

One goal of solving slot coating flow problems is to obtain the physical variables associated with the coating flow, such as the velocity and pressure fields, when given the parameter values. Through this type of analysis, it is possible for one to assess the quality of the coating flow that arises from the given set of parameters. On the other hand, in other situations, some information or restriction on the coating flow is given, and the goal is to find the specific set of parameters that results in the flow with given characteristics. With the two-way problem solving, one can gain a comprehensive understanding on the stable operation of slot coating process for producing high-quality products.

The purpose of this study is to widen the perspective on problem solving in slot coating flows by exploring previously unsolved problems and using previously untried methods. In Chapter 2, we examine the effect of slot-die configuration on the coating gap dependence of limiting wet thicknesses, using a simple analytical model of the slot coating flow. Through the analysis, the reason behind a peculiar phenomenon where the maximum wet thickness decreases with increasing coating gap is revealed. In Chapter 3, we obtain the critical operating conditions for vortex to form inside the slot coating flows. The study involves several types of flow models and vortex formation conditions (both numerical and analytical) are obtained for the coating flows of fluids with shear rate dependent viscosities. In Chapter 4, a machine learning based method is used to model the slot coating flow. Exemplary problems are solved with this method to demonstrate its flexibility in handling problems with partially missing data.

keywords: Slot coating process, Generalized Newtonian fluids, Finite element method, Couette-Poiseuille flow, Physics-informed neural networks

student number: 2018-28363

Contents

Abstract **i**

Contents **iii**

List of Tables **vi**

List of Figures **vii**

1 Introduction **1**

- 1.1 Slot coating process and slot coating flow 1
- 1.2 Slot coating flow problems 4
- 1.3 Mathematical and computational models for modeling slot coating flows 7

2 Effect of slot-die geometry on coating gap dependence of wet thicknesses **9**

- 2.1 Introduction 9
- 2.2 Mathematical formulation 12
- 2.3 Numerical validation 15
- 2.4 Results and discussion 18
  - 2.4.1 Minimum wet thickness (Bead-breakup limit) 18
  - 2.4.2 Maximum wet thickness (Weeping limit) 20
- 2.5 Conclusions 27

3 Conditions for vortex formation in slot coating flows 29

3.1 Introduction 29

3.2 Vortex formation condition in coating bead flow of power-law fluids 31

3.2.1 Two-dimensional (2-D) computational flow model 32

3.2.2 Solution methods 36

3.2.3 Results and discussion 39

3.3 Flow reversal condition in one-dimensional flow model 44

3.3.1 Mathematical formulation 45

3.3.2 Comparison with 2-D model 49

3.4 Local power-law approximation method 54

3.4.1 Results and discussion 56

3.5 Semi-analytical method 66

3.5.1 Source of error in local power-law approximation method revisited 69

3.6 Conclusions 73

4 Physics-informed machine learning of slot coating flows 74

4.1 Introduction 74

4.2 Comparison with regression problems 76

4.3 Network architecture 79

4.4 Loss function 81

4.5 Optimization method 84

4.6 Results and discussion 85

4.6.1 Problem 1: missing physics 86

4.6.2 Problem 2: missing data 90

4.7 Conclusions 92

5 Concluding remarks 94

Abstract (In Korean) 103

List of Tables

2.1 Operating conditions and geometric parameters used in numerical validation. 16

3.1 Operating conditions and geometric parameters used in 2-D computational flow model. 35
3.2 Dimensionless velocity profile, pressure gradient, and flow rate conditions for different flow states in 1-D C-P flow of power-law fluids. 50
3.3 Values of model parameters. 58

4.1 Operating parameters considered in the analysis. 87

List of Figures

1.1 A schematic diagram of slot coating process. 2

1.2 Typical dimensions in slot coating flows. 4

1.3 Adjustable parameters associated with slot coating flows. 4

1.4 Slot-dies with tilted configuration. 6

1.5 Relationships between different groups of variables associated with slot coating flows. 7

2.1 Coating bead flow in slot coating process. 9

2.2 Operating limits associated with position of upstream meniscus. . . 10

2.3 Parameters associated with coating bead flow. 13

2.4 Slot-die configurations considered in this chapter. 14

2.5 Boundary conditions used for numerical validation. 17

2.6 Dependence of the wet thickness on coating gap at bead-breakup limit derived by the simple model. 19

2.7 Streamline plot of coating bead flow at bead-breakup limit under the uniform configuration. 20

2.8 Dependence of wet thickness on coating gap at bead-breakup limit under three different slot-die configurations: uniform, underbite, and overbite, computed using the 2-D computational model. 21

2.9 Dependence of wet thickness on coating gap at weeping limit under the uniform configuration, derived from the simple model. 22
2.10 Dependence of wet thickness on coating gap at weeping limit under the underbite configuration, derived from the simple model. 24
2.11 Dependence of wet thickness on coating gap at weeping limit under the overbite configuration, derived from the simple model. 25
2.12 Dependence of wet thickness on coating gap at weeping limit under three different slot-die configurations: uniform, underbite, and overbite, computed using the 2-D computational model. 26

3.1 Microvortices found in the coating bead flow. 30
3.2 Computational mesh used for 2-D flow model. 33
3.3 Schematic diagram of the coating bead flow and boundary conditions associated with the governing equations. 34
3.4 Two different types of vortices found in the slot coating flow. 40
3.5 Operating conditions at the moment of vortex birth in the upstream region. (2-D FEM computations) 42
3.6 Operating conditions at the moment of vortex birth in the downstream region. (2-D FEM computations) 44
3.7 Configuration of the planar Couette–Poiseuille (C-P) flow considered in 1-D flow analysis. 45
3.8 Four distinguishing flow states, dependent on operating conditions. . 49
3.9 Operating conditions that divides the flow states in the C-P flow of power-law fluids. 50
3.10 Dimensionless flow rate at the moment of vortex birth (2-D FEM computations) and flow reversal (1-D model prediction) plotted together against the power-law index. 51

3.11 Velocity profiles under the downstream die lip, as predicted by the 1-D rectilinear flow model. 53
3.12 Flow curve plotted in log–log scale. Fluid is approximated as power–law fluid at a representative shear rate. 55
3.13 Flow curves of Carreau–Yasuda (C–Y) and Bingham–Carreau–Yasuda (B–C–Y) fluids. 57
3.14 Tree diagram showing cases where LPLA method is applied to approximate critical flow reversal conditions. 58
3.15 Normalized velocity profiles of Couette–Poiseuille (C–P) flow of Carreau–Yasuda (C–Y) and Bingham–Carreau–Yasuda (B–C–Y) fluid at the onset of flow reversal, under different values of operating conditions. 59
3.16 Dimensionless critical flow rate per width for C–Y fluid predicted using LPLA method. 61
3.17 Dimensionless critical flow rate per width for B-C–Y fluid predicted using LPLA method. 61
3.18 Dimensionless critical pressure gradient for C–Y fluid predicted using LPLA method by approximating wall shear rate. 64
3.19 Dimensionless critical pressure gradient for C–Y fluid predicted using LPLA method by approximating wall shear stress. 64
3.20 Dimensionless critical pressure gradient for B-C–Y fluid predicted using LPLA method by approximating wall shear rate. 65
3.21 Dimensionless critical pressure gradient for B-C–Y fluid predicted using LPLA method by approximating wall shear stress. 65
3.22 Configuration of flow considered in the derivation of semi-analytical method. 66

3.23 (C–Y fluid) Ratio of approximate to exact value of terms constituting the equation from semi-analytical method. 71
3.24 (B–C–Y fluid) Ratio of approximate to exact value of terms constituting the equation from semi-analytical method. 72

4.1 Schematic diagram of solving a regression problem using a neural network. 77
4.2 Schematic diagram of solving a differential equation using physics-informed machine learning technique. 78
4.3 Schematic diagram of two separate neural networks for modeling the flows with liquid-gas interfaces. 79
4.4 Domain decomposition applied to the reference domain and the physical domain. 80
4.5 Swish activation function. 81
4.6 Application of flow rate conditions. 83
4.7 y-component of the velocity predicted by the trained PINN with and without using adaptive weighting scheme. 86
4.8 Cross-section for assessing the accuracy of predicted field variables. 88
4.9 Velocity and pressure fields predicted by using PINN and FEM. . . 89
4.10 Flow visualization setup for obtaining side-view images of coating bead flows and the obtained side-view image of coating bead flow showing the upstream region of the flow. 90
4.11 Uncertainty in the image data is modeled by deliberately omitting part of the given data on meniscus shape and position. 91
4.12 Dynamic contact angle predicted by PINN when only a part of the data is given. 92

Chapter 1

Introduction

1.1 Slot coating process and slot coating flow

Liquid film coating is a process by which a gas previously in contact with a substrate is replaced by a thin film of liquid. It is used in many industrial processes to produce thin films with wet thickness ranging from 1 to 100 microns (Kistler & Schweizer, 1997). One of such coating process is the slot coating process, whose schematic is shown in Figure 1.1.

Slot coating process is a versatile method for producing thin film products with a variety of functionalities. Many industries have successfully employed this process to produce a wide range of high-value film products, including optical films, solar cells, and battery electrodes (Patidar *et al.*, 2020; Schmitt *et al.*, 2014; Ding *et al.*, 2016). Some important and useful characteristics of the process are as follows:

1. It is a roll-to-roll continuous coating process and is thus suitable for mass production.
2. Self-leveling of coated liquid allows uniform thickness to be achieved across a large area.

3. It is a pre-metered coating process that allows a precise control over the film thickness; the wet thickness is pre-determined by the amount of coating fluid provided to the process.

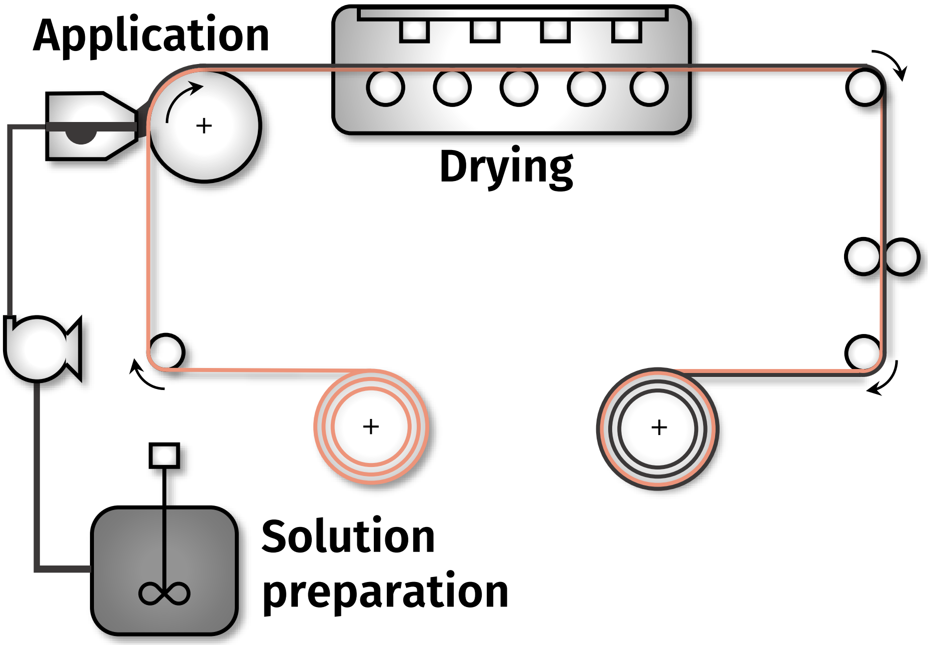

Figure 1.1: A schematic diagram of slot coating process.

As shown in Figure 1.1, the slot coating process typically consists of three main unit operations: solution preparation, application, and drying.

In the *solution preparation* step, the coating solution is prepared by mixing different kinds of components that give the film its desired properties. Solvent is also carefully selected such that the resulting mixture forms a stable coating solution with a desired distribution of active components. When choosing different materials and solvents that compose the coating solution, the processability of the fluid must also be given consideration. Thus, it is not an uncommon practice to add materials that are solely responsible for controlling the rheological properties of the coating solution.

The prepared solution is delivered to the coating station where it goes through the *application* stage of the coating process. The coating solution is first fed into the slot-die and is distributed in the widthwise direction in a cavity within the die. The distributed solution is then extruded out of the die through a thin slit and is deposited onto the moving substrate. The flow that forms in this region is also known as the *coating bead* flow and maintaining its stability is the key to the successful process operation and production of high quality films.

In the *drying* stage, the coated substrate is transported to the drying chamber where the excess solvent is removed through evaporation. When the coating solution is a suspension that contains particles of varying sizes, particle migration can occur during the drying phase, resulting an uneven distribution of particles along the thickness direction of the film (Lim *et al.*, 2013; Zang *et al.*, 2010). A careful control over the evaporation rate is required to minimize this kind of side effect. After being dried, the film may also go through the calendaring step where the dried film is calendared to achieve required thickness and properties.

Among the different phenomena that are found in the three main stages of the slot coating process, we focus mainly on the coating bead flow that occurs during the application stage. Typical dimensions of a coating bead flow are presented in Figure 1.2. Because the width of the flow is typically far larger than the height or the streamwise length, the two-dimensional (2-D) approximation on the flow is valid under most situations. Another important characteristics of the flow is the existence of the liquid-gas menisci in the upstream and downstream (relative to the substrate motion) regions. The upstream meniscus connects two solid surfaces — the slot-die lip and the moving substrate — and forms two separate contact lines. Also, due to the small height which serves as the characteristic length of the flow, the Reynolds number is typically within the order of 10, which makes the flow laminar.

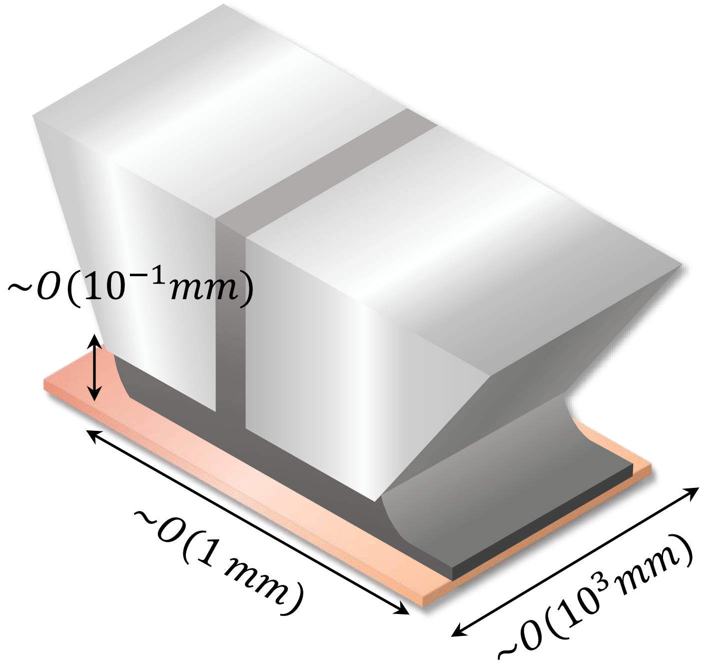

Figure 1.2: Typical dimensions in slot coating flows.

1.2 Slot coating flow problems

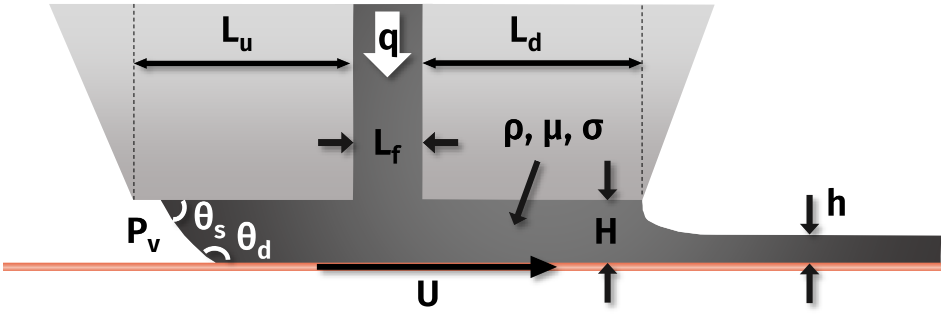

Figure 1.3: Adjustable parameters associated with slot coating flows.

As illustrated in Figure 1.3, there are a number of adjustable parameters associated with the coating bead flow. Different sets of parameters can be thought as separate points residing in the vast *parameter space*. They can be categorized into three groups: operating parameters, geometric parameters, and material properties.

Operating parameters are the variables that can be readily and directly controlled by the operator to result in a stable coating bead flow. For example, the coating gap, H_u or H_d, can be changed by adjusting the relative position of slot-die with respect to the moving substrate; the prescribed flow rate (per width), q, can be controlled by adjusting the feed rate of the pump; and the substrate speed, U, can be adjusted by controlling the rotation speed of the backup roll. Sometimes a slight vacuum, P_v, is applied at the upstream meniscus to offset forces that pushes the meniscus towards the feed slot and destroys the stable coating bead (Gates, 1999). The wet thickness of the coated film, h, can also be considered as an operating parameter since it is pre-metered by the amount of supplied coating solution and the substrate speed. The three variables are related simply by $h = q/U$.

Geometric parameters are the design parameters of the slot-die. It is possible to adjust the length of the die lip, L_u or L_d, to control the pressure distribution along the coating bead. Apart from the flat design, the surface of the die lip can also take on different shapes and structures (Sartor, 1990). In addition, the slot-die can be mounted in various ways such that it has a non-zero angle of attack (Lee & Nam, 2015*a*), as shown in Figure 1.4. The lip surfaces in the upstream and downstream regions can also be placed in different planes in such a way that the gap difference $\Delta H = H_\mathrm{d} - H_\mathrm{u}$ has a non-zero value.

Material properties are the variables that represent the physical and chemical properties of the coating fluid, such as density (ρ), viscosity (μ), and surface tension (σ). As shortly discussed in Section 1.1, these properties are readily determined by different materials that are added to the coating solution. The viscosity of the fluid can be modeled using different types of constitutive equation, and the parameter values

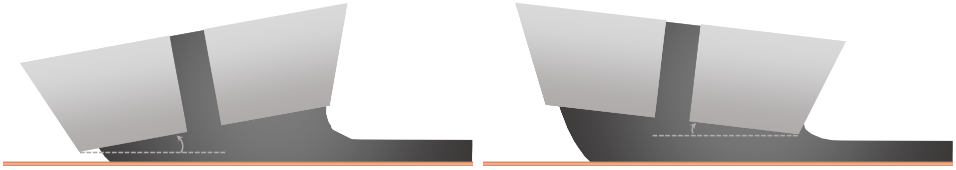

Figure 1.4: Slot-dies with tilted configuration.

are determined by fitting the equation to the rheological measurement data. The static contact angle, θ_s, can be regarded as a material property as it is related to the work of adhesion, W, and the surface tension, σ, of the liquid via the Young–Dupré equation:

$$W = \sigma(1 + \cos\theta_\mathrm{s}). \tag{1.1}$$

The dynamic contact angle, θ_d, can be considered as both a material property and an operating parameter, since it depends on both the choice of material as well as the substrate speed (Cox, 1986).

Once a specific set of parameter values (or a point in the *parameter space*) are fixed, the slot coating process can be operated under that specific set of parameters to give rise to the actual slot coating flow, which can be described by the shape and position (x and y) of menisci, the velocity field (u and v), and the pressure field (p). The flow patterns exhibited by the coating flow and the shape of the coating bead both have profound impact on the stable process operation and the quality of the final film product. Therefore, understanding the interplay between the parameter space and the physical variables (x, y, u, v, p) is crucial for the production of high quality product through a well controlled process operation.

Two types of problems naturally arise when considering the mapping between the parameter space and the physical variables. In the first type of problems, all the necessary parameters are given such that the physical field variables associated with the coating bead flow is obtained. This can be thought as a situation where the operating parameters, choices of coating solution composition and slot-die design are fixed, and one is interested in finding the resultant flow. On the other hand, in the second type of problems, some information on the physical variables of the flow is given and the goal is to find the specific parameters that resulted in the flow with the given characteristics. In this situation, the data given can be the shape and position of the interface, the velocity or pressure of the flow, or both. These may be actual measurements from various sensors and imaging devices, or may even be hypothetical data derived from calculation. The relationships between different groups of variables are summarized in Figure 1.5.

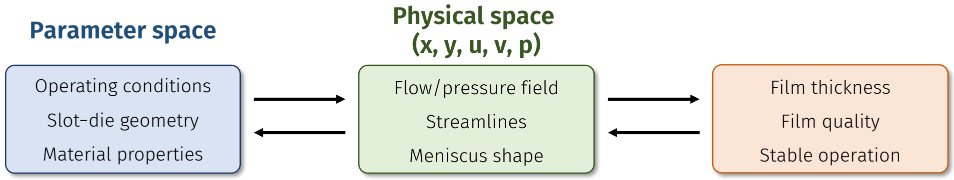

Figure 1.5: Relationships between different groups of variables associated with slot coating flows.

1.3 Mathematical and computational models for modeling slot coating flows

In this thesis, the previously unsolved problems of slot coating flows are addressed using a variety of models and methods.

Chapter 2 focuses on on how the wet thickness limits are dependent on the coating gap for various slot-die geometries. An analytical model derived from one-dimensional (1-D) approximation of the coating bead flow is used to obtain analytical expressions for the maximum and minimum wet thicknesses under different die lip configurations. The derived expression is used to examine the dependence of the wet thicknesses on the coating gap. A two-dimensional (2-D) computational model is also utilized simply for the verification of the 1-D results.

On the other hand, the 2-D computational flow model is introduced in Chapter 3 as a main tool for solving a slot coating flow problem to obtain operating parameters that lead to vortex formation within the coating bead flow. Derivation of analytical expressions for the vortex formation condition is made possible by further simplification of the flow. The derived equations are applied to fluids modeled by more complex constitutive equations, thereby introducing an approximation method for solving the given problem. In addition, a semi-analytical method that solves the problem exactly is also introduced for the given fluids.

In Chapter 4, a machine learning based approach is adopted to solve slot coating flow problem when the given data is missing in parts. Unlike conventional methods which require a complete set of unknowns and equations for the problem to be solved, the machine learning based problem solving provides the flexibility to handle incomplete data. This is demonstrated by solving problems where a boundary condition is deliberately neglected, and where only a part of the meniscus shape data is given.

Chapter 2

Effect of slot-die geometry on coating gap dependence of wet thicknesses

2.1 Introduction

Figure 2.1 shows a schematic of the coating bead flow that occurs within the gap between the slot-die and moving substrate. The feed slot segregates the bead into upstream and downstream regions, and each region is bounded by a liquid–gas interface. Adequate control over the shape and position of this interface is key to achieving stable process operation and defect-free films.

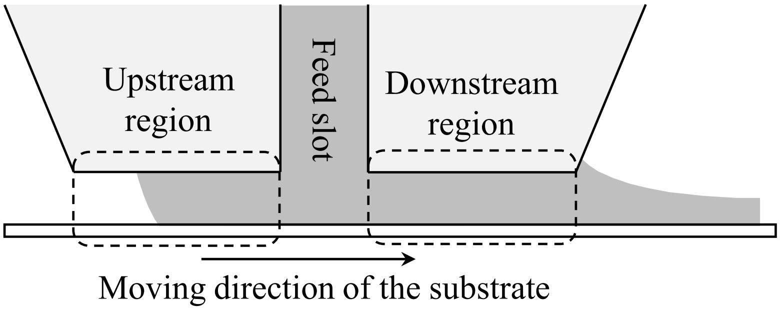

Figure 2.1: Coating bead flow in slot coating process.

Experimental and theoretical studies pertaining to operating limits associated with coating bead menisci are abundant in the literature. For example, Higgins & Scriven (1980) studied the allowable range of operating conditions by considering the bounds for the position of the upstream meniscus. Carvalho & Kheshgi (2000) studied the *low-flow limit*, which is the operating limit associated with highly curved downstream meniscus.

Under various operating conditions, the coating bead adjusts its size accordingly by allowing the upstream meniscus to slide along the upstream die lip. Increasing/decreasing the flow rate or decreasing/increasing the substrate speed results in the extension/shrinkage of the upstream coating bead. When the bead length reaches its maximum, the meniscus is pinned at the upstream corner of the die lip, as depicted in Figure 2.2A. This state is denoted by the *weeping limit*, beyond which may result in loss of the liquid. On the opposite end is the *bead-breakup limit*, where the upstream meniscus is situated beneath the feed-side corner of the upstream die lip, as depicted in Figure 2.2B. Further drawing of the meniscus toward the feed slot results in coating defects (Lee *et al.*, 1992; Yang *et al.*, 2004).

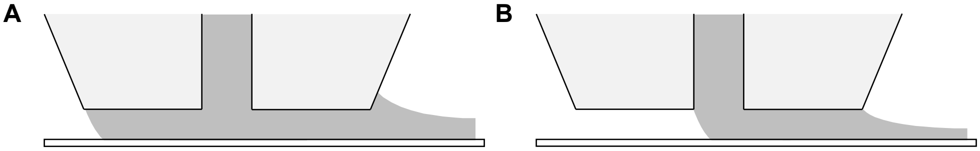

Figure 2.2: Operating limits associated with position of upstream meniscus: A. Weeping limit and B. bead-breakup limit.

The aforementioned operating limits can be similarly described in terms of *wet thickness*, which is obtained by dividing the flow rate per width by the substrate speed. By considering the specific operating conditions that result in the two limits, we find that the maximum and minimum attainable wet thicknesses are determined by the weeping and bead-breakup limits, respectively.

When the coating liquid is confined by a stationary wall, the wet thickness scales with the coating gap (Kim & Nam, 2017). In general, a wider coating gap allows for more coating liquid to flow between the slot-die and substrate; hence, a larger maximum wet thickness is expected. However, we demonstrate that a counterintuitive result can be obtained under a certain slot-die configuration.

Previous studies on different types of slot-die configurations were conducted under a fixed or oscillating coating gap. Koh *et al.* (2012) investigated the effect of slot-die configuration on the operability window expressed in terms of the bead pressure and the substrate speed. Romero & Carvalho (2008) and Lee & Nam (2015*b*) conducted frequency response analyses to study the effect of gap disturbances under different slot-die configurations. In this chapter, we take a closer look at the effect of increasing or decreasing coating gap on the limiting wet thicknesses while varying the slot-die configurations.

In the following sections, a simple model for the coating bead flow is introduced, and expressions for the limiting wet thicknesses at the weeping and bead-breakup limits are derived from the model. The dependency of the wet thicknesses on the coating gap is then derived to demonstrate how it differs under varying slot-die configurations. According to the definition in Section 1.2, the problem covered in this chapter can be categorized as the second type, since the goal of the given problem is to find the expression for the limiting wet thicknesses, given the length of the upstream bead at the operating limits. A two-dimensional (2-D) numerical analysis of the same system using the finite element method (FEM) is also presented to validate the conclusions generated from the simple model.

2.2 Mathematical formulation

The *viscocapillary model* (Ruschak, 1976; Higgins & Scriven, 1980) is a practical and simple analytical model for analyzing coating bead flow. The model expresses the overall pressure difference across the coating bead as a combination of pressure differences at two liquid–gas interfaces and pressure gradients associated with the lubrication flow.

Typically, the pressure jump across the downstream meniscus is modeled using the following equation, which is derived from the Landau-Levich (Landau & Levich, 1942) film coating theory:

$$\Delta P = 1.34 \left(\frac{\mu U}{\sigma}\right)^{2/3} \frac{\sigma}{h_\mathrm{w}}, \tag{2.1}$$

where μ, σ, U, and h_w denote liquid viscosity, surface tension, substrate speed, and wet thickness, respectively. The pressure difference across the upstream meniscus is modeled using the Young-Laplace equation, which can be expressed as follows:

$$\Delta P = -\frac{\sigma}{H_\mathrm{u}}(\cos\theta_\mathrm{d} + \cos\theta_\mathrm{s}), \tag{2.2}$$

where H_u denotes the upstream coating gap and θ_d and θ_s represent the dynamic and static contact angles, respectively.

We assume that the capillary number of the system is sufficiently large such that the contribution of the pressure differences across the menisci is negligible compared with that of the viscous effects. This assumption is valid under sufficiently large viscosity or high substrate speed. Furthermore, we assume that the die lip surface is parallel to the moving substrate, such that the flow in between is strictly rectilinear. Under these assumptions, the viscocapillary model for steady Newtonian coating bead flow can be expressed as follows:

$$\frac{6\mu U}{H_\mathrm{d}}\left(1 - 2\frac{h_\mathrm{w}}{H_\mathrm{d}}\right)\frac{L_\mathrm{d}}{H_\mathrm{d}} + \frac{6\mu U}{H_\mathrm{u}}\frac{x}{H_\mathrm{u}} = P_\mathrm{a} - P_\mathrm{v}. \tag{2.3}$$

Here, H and L denote the coating gap and die lip length, respectively; subscripts d and u represent the downstream and upstream regions of the coating bead, respectively; x denotes the length of the upstream coating bead, which can adjust itself to match the operating conditions; P_a denotes the ambient pressure outside the downstream meniscus; P_v denotes the vacuum pressure, if any, applied to the upstream meniscus. Refer to Figure 2.3 for details.

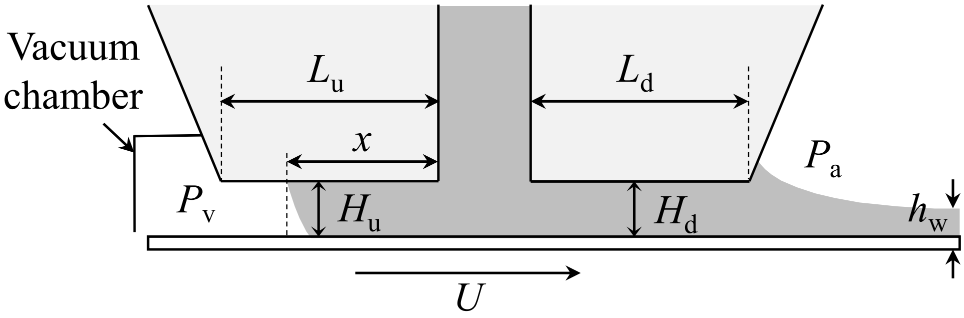

Figure 2.3: Parameters associated with coating bead flow.

When no vacuum is applied, P_v equals P_a, and rearranging Equation (2.3) yields the following expression for the wet thickness, h_w:

$$h_\mathrm{w} = \frac{H_\mathrm{d}}{2}\left[1 + \left(\frac{H_\mathrm{d}}{H_\mathrm{u}}\right)^2 \frac{x}{L_\mathrm{d}}\right]. \tag{2.4}$$

In general, the coating gaps in the upstream and downstream regions are set equal, i.e., $H_\mathrm{u} = H_\mathrm{d}$. However, the two gaps can also be set differently to exploit different slot-die configurations (Romero & Carvalho, 2008; Chin *et al.*, 2010; Lee *et al.*, 2011; Lee & Nam, 2015*a*). The case in which $H_\mathrm{d} > H_\mathrm{u}$ is known as the underbite configuration, whereas the opposite case is referred to as the overbite configuration. The three configurations are illustrated in Figure 2.4.

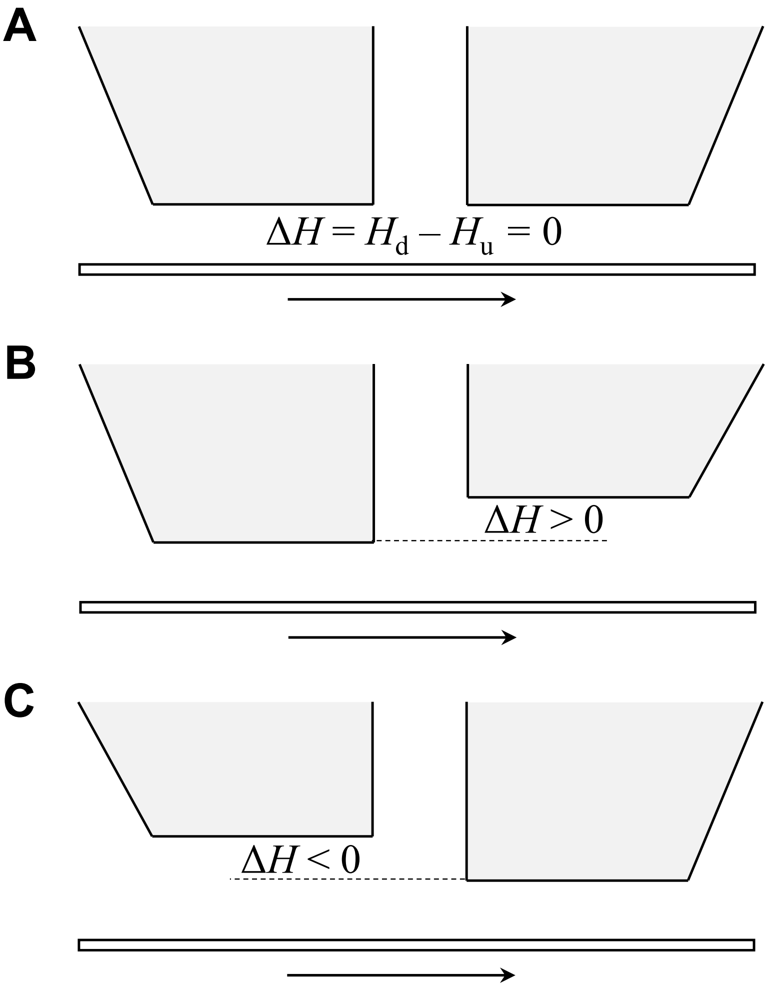

Figure 2.4: Slot-die configurations considered in this chapter: A. Uniform, B. underbite, and C. overbite.

By introducing the gap difference $\Delta H = H_\mathrm{d} - H_\mathrm{u}$, Equation (2.4) becomes

$$h_\mathrm{w} = \frac{H_\mathrm{d}}{2}\left[1 + \left(\frac{H_\mathrm{d}}{H_\mathrm{d} - \Delta H}\right)^2 \frac{x}{L_\mathrm{d}}\right]$$
$$= \frac{H_\mathrm{u} + \Delta H}{2}\left[1 + \left(1 + \frac{\Delta H}{H_\mathrm{u}}\right)^2 \frac{x}{L_\mathrm{d}}\right]. \qquad (2.5)$$

Under a fixed configuration, the derivatives of h_w with respect to H_d and H_u are the same because ΔH remains constant. Therefore, we examine the sensitivity of h_{w} with respect to H_{d} alone.

$$\frac{\partial h_{\mathrm{w}}}{\partial H_{\mathrm{d}}} = \frac{1}{2} + \frac{x H_{\mathrm{d}}^2 (H_{\mathrm{d}} - 3\Delta H)}{2 L_{\mathrm{d}} (H_{\mathrm{d}} - \Delta H)^3}. \tag{2.6}$$

It is noteworthy that the value of this derivative depends not only on the operating limit (associated with x), but also on the slot-die configuration (associated with ΔH).

2.3 Numerical validation

The conclusions derived from the simplified version of the viscocapillary model are also validated by numerical method, which involves fewer assumptions on the system and is considered more accurate.

The governing equations of the system of interest are the 2-D steady momentum conservation equation (with the body force neglected) and the continuity equation, which can be expressed as follows:

$$\rho \mathbf{u} \cdot \nabla \mathbf{u} = \nabla \cdot \mathbf{T}, \tag{2.7}$$

$$\nabla \cdot \mathbf{u} = 0, \tag{2.8}$$

where ρ, μ, $\mathbf{u}$, and p represent density, viscosity, velocity field, and pressure field, respectively. $\mathbf{T}$ denotes the total stress tensor which is given by $\mathbf{T} = -p\mathbf{I} + \mu \left[\nabla \mathbf{u} + (\nabla \mathbf{u})^{\mathsf{T}}\right]$ for the incompressible Newtonian fluid, where $\mathbf{I}$ denotes the identity tensor. The associated boundary conditions are illustrated in Figure 2.5.

The operating parameters used in numerical validation are listed in Table 2.1. Note that the flow rate per width is not provided as an input to the system but is instead obtained as an outcome of the computation, such that the corresponding coating bead flow is either in the bead-breakup or weeping limit. The resulting wet thickness is in the order of several hundred micrometers (µm), which is observed in thick-film-coating applications, such as the production of thick battery electrodes (Diehm *et al.*, 2020; Li *et al.*, 2021). Viscosity is chosen to have a value that a shear-thinning polymer solution would exhibit when exposed to a high-shear flow.

The governing equations, together with the boundary conditions are discretized and solved using the Galerkin finite element method (G/FEM). The detailed description on the solution method is deferred to Chapter 3, where the 2-D computational flow model is used as the main method for solving the given problem.

Table 2.1: Operating conditions and geometric parameters used in numerical validation.

Operating parameters	Unit	Value or Range
Density (ρ)	$\mathrm{g/cm^3}$	1
Viscosity (μ)	$\mathrm{Pa \cdot s}$	1
Surface tension (σ)	$\mathrm{mN/m}$	70
Substrate speed (U)	$\mathrm{mm/s}$	75
Flow rate per width (q)	$\mathrm{mm^2/s}$	8.736 - 36.85
Static contact angle (θ_s)	$^\circ$	50
Dynamic contact angle (θ_d)	$^\circ$	160
Geometric parameters	**Unit**	**Value or Range**
Downstream die lip length (L_d)	mm	1.0
Upstream die lip length (L_u)	mm	1.0
Feed slot height (L_f)	mm	1.0
Downstream coating gap (H_d)	mm	0.2 - 0.5
Gap difference (ΔH)	mm	-0.2, 0.0, 0.1

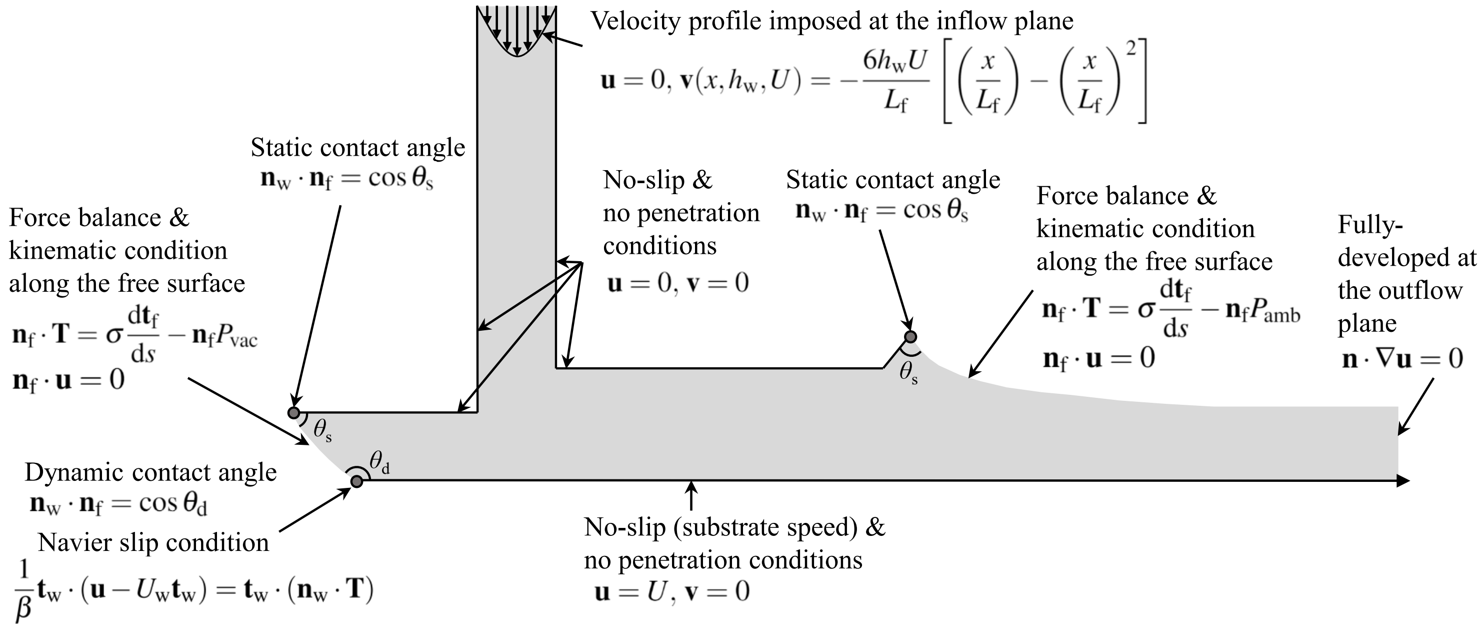

Figure 2.5: Boundary conditions used for numerical validation.

2.4 Results and discussion

As discussed earlier, the two operating limits considered in this chapter are characterized by the size of the upstream coating bead. More specifically, the upstream region of the coating bead is devoid of liquid flow at the bead-breakup limit, whereas the coating liquid occupies the entire upstream region of the coating bead at the weeping limit.

The simple model represents the two limiting states by setting the upstream bead length, x, to be either zero or the upstream die lip length, L_{u}. As with the 2-D computational model, the system of governing equations is first augmented with equations that describe the position of the static and dynamic contact lines at the onset of the operating limits. Subsequently, the operating conditions that lead to the two states, including the wet thickness, are obtained directly by solving the augmented system of equations. The details of the method are elaborated in Chapter 3.

The dependencies of the limiting wet thicknesses on the coating gap, obtained both analytically and numerically, are presented in the following subsections.

2.4.1 Minimum wet thickness (Bead-breakup limit)

Substituting $x = 0$ into Equation (2.6) yields the following expression for the derivative:

$$\left(\frac{\partial h_{\mathrm{w}}}{\partial H_{\mathrm{d}}}\right)_{\mathrm{B}} = \frac{1}{2}. \tag{2.9}$$

Subscript B denotes the bead-breakup limit. We find that the wet thickness at the bead-breakup limit depends linearly on the coating gap with a proportionality constant of 0.5, as depicted in Figure 2.6.

Figure 2.7 depicts the streamlines of the coating bead flow at the bead-breakup limit under a uniform configuration, obtained using the numerical methods described earlier. The dynamic contact line of the upstream meniscus is immediately beneath

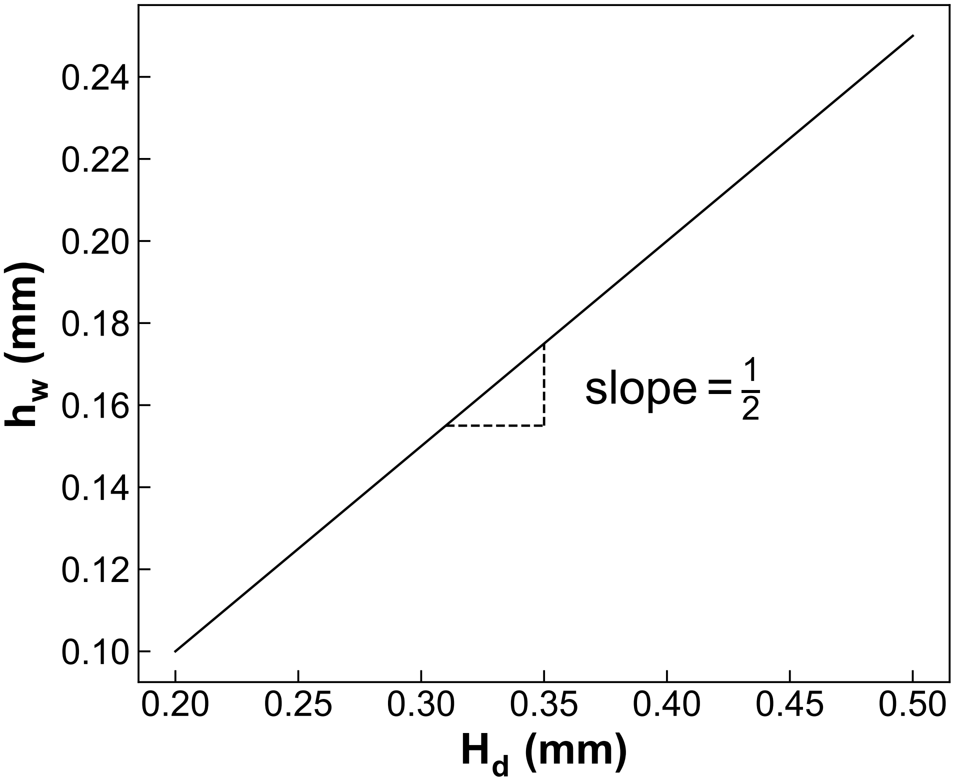

Figure 2.6: Dependence of the wet thickness, h_{w}, on coating gap, H_{d}, at bead-breakup limit derived by the simple model. Parameters used were $L_{\mathrm{d}} = L_{\mathrm{u}} = 1.0\,\mathrm{mm}$ and $\Delta H = 0$.

the feed slot corner, indicating that the bead-breakup limit has been reached.

The numerically obtained dependences of the minimum attainable wet thicknesses on the downstream coating gap are shown in Figure 2.8. The observed trend coincides with that obtained from the simple model; the wet thicknesses exhibit a nearly linear dependence on the coating gap for all three die lip configurations considered.

It is worth noting that both h_{w} and $\partial h_{\mathrm{w}}/\partial H_{\mathrm{d}}$ derived from the simple model (Equation (2.5) and Equation (2.6)) are independent of ΔH when $x = 0$, whereas

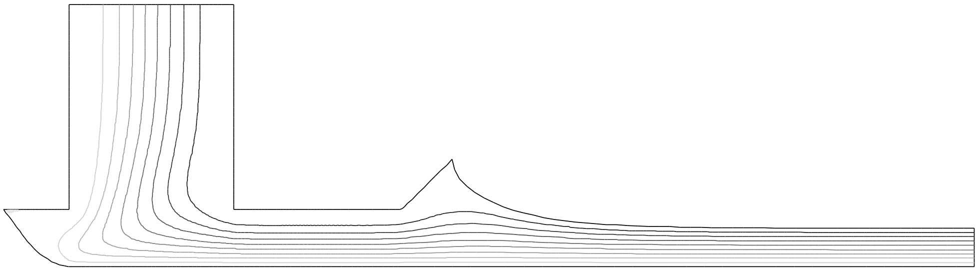

Figure 2.7: Streamline plot of coating bead flow at bead-breakup limit under the uniform configuration ($\Delta H = 0$). Coating gap of $H_{\mathrm{d}} = 0.35\,\mathrm{mm}$ is used.

those computed numerically differ for each slot-die configuration. It is most likely that the difference originates from the upstream meniscus present in the computational model, whose shape changes with varying die configurations, and is completely neglected in the simple model.

2.4.2 Maximum wet thickness (Weeping limit)

By substituting $x = L_{\mathrm{u}}$ into Equation (2.6), we obtain

$$\left(\frac{\partial h_{\mathrm{w}}}{\partial H_{\mathrm{d}}}\right)_{\mathrm{W}} = \frac{1}{2} + \frac{L_{\mathrm{u}} H_{\mathrm{d}}^2 (H_{\mathrm{d}} - 3\Delta H)}{2L_{\mathrm{d}}(H_{\mathrm{d}} - \Delta H)^3} = \frac{f(H_{\mathrm{d}})}{2L_{\mathrm{d}}(H_{\mathrm{d}} - \Delta H)^3}, \tag{2.10}$$

$$f(H_{\mathrm{d}}) = (L_{\mathrm{d}} + L_{\mathrm{u}})[H_{\mathrm{d}}^3 - 3(\Delta H) H_{\mathrm{d}}^2] + 3L_{\mathrm{d}}(\Delta H)^2 H_{\mathrm{d}} - L_{\mathrm{d}}(\Delta H)^3, \tag{2.11}$$

where subscript W denotes the weeping limit. Unlike the bead-breakup limit, the derivative is dependent on the slot-die configuration. In the following, we present a detailed discussion on how the sensitivity differs in each configuration.

Uniform configuration ($\Delta H = 0$)

First, we consider the *uniform configuration*, where $\Delta H = 0$. Subsequently, Equation (2.10) reduces to the following expression:

$$\left(\frac{\partial h_{\mathrm{w}}}{\partial H_{\mathrm{d}}}\right)_{\mathrm{W,uniform}} = \frac{1}{2}\left(1 + \frac{L_{\mathrm{u}}}{L_{\mathrm{d}}}\right). \tag{2.12}$$

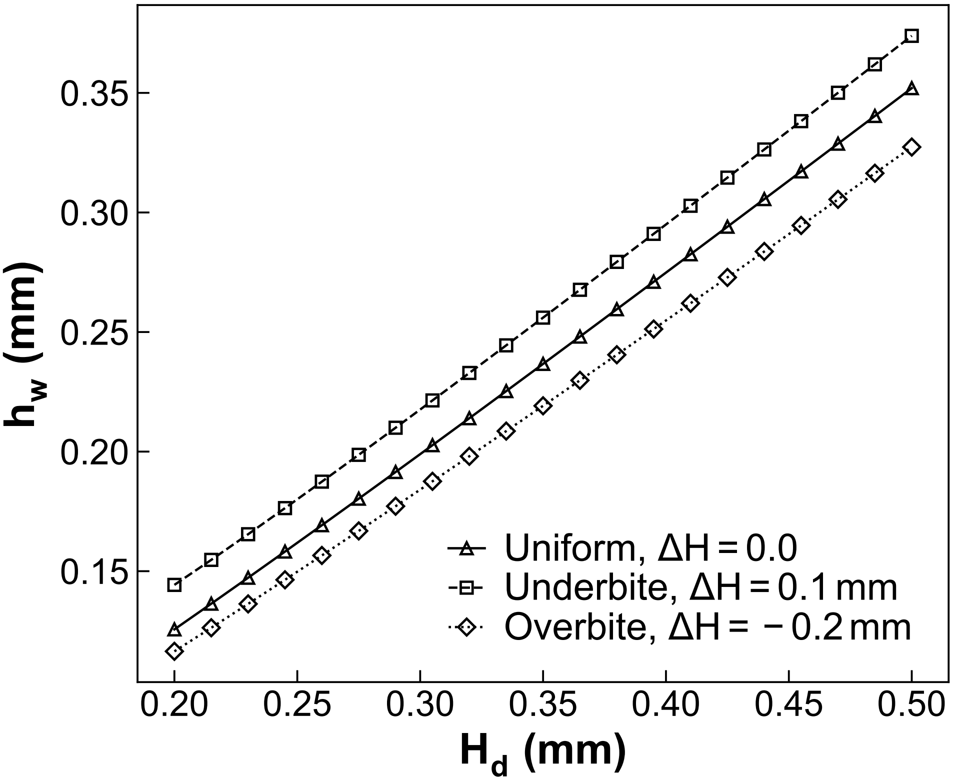

Figure 2.8: Dependence of wet thickness, h_{w}, on coating gap, H_{d}, at bead-breakup limit under three different slot-die configurations: uniform (solid line with triangle marker, $\Delta H = 0$), underbite (dashed line with square marker, $\Delta H = 0.1\,\mathrm{mm}$), and overbite (dotted line with diamond marker, $\Delta H = -0.2\,\mathrm{mm}$), computed using the 2-D computational model. Parameters used are summarized in Table 2.1.

Because the die lip lengths, L_{u} and L_{d}, are constants, h_{w} in this case is directly proportional to H_{d}, which is similar to the bead-breakup limit case, as shown in Figure 2.9. However, the proportionality constant in Equation (2.12) is greater than that of the bead-breakup limit case, as $L_{\mathrm{u}}/L_{\mathrm{d}}$ is always nonnegative. In addition, under the uniform configuration, the wet thickness at the weeping limit (maximum obtainable wet thickness) increases with the coating gap, as expected.

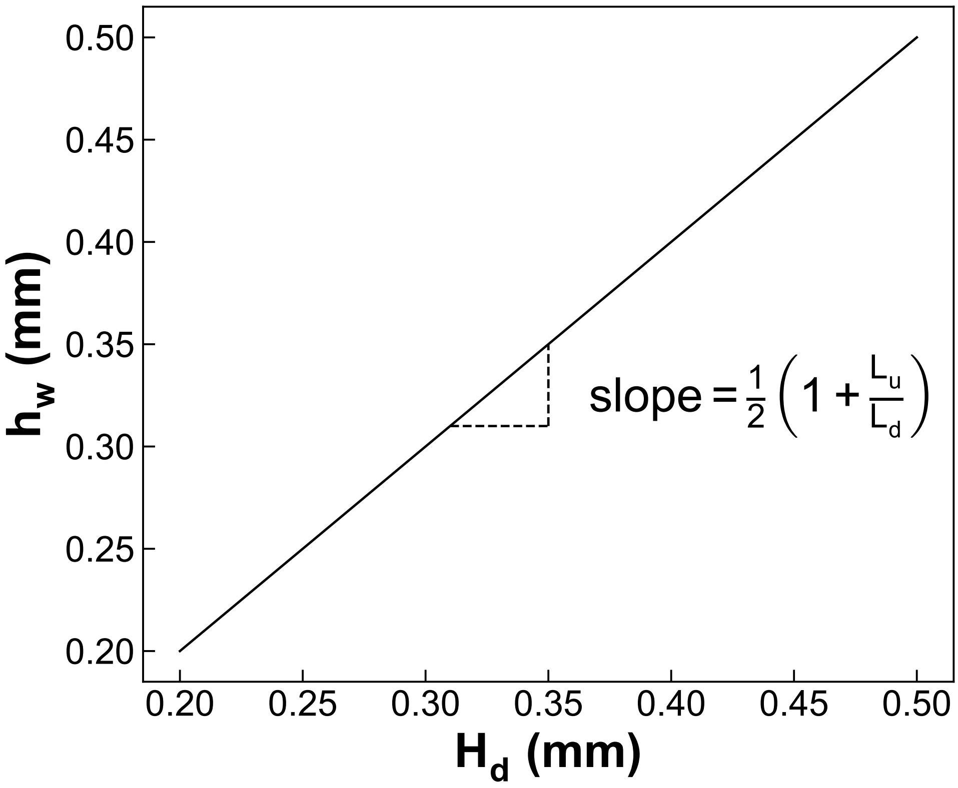

Figure 2.9: Dependence of wet thickness, h_w, on coating gap, H_d, at weeping limit under the uniform ($\Delta H = 0$) configuration, derived from the simple model. Other parameters were $L_\mathrm{d} = L_\mathrm{u} = 1.0\,\mathrm{mm}$.

Underbite configuration **($\Delta H > 0$)**

However, this trend differs significantly in the *underbite configuration*, where $\Delta H > 0$. In the following, we establish the existence of a local minimum for h_w.

In the underbite configuration, the downstream coating gap, H_d, must satisfy the constraint $H_\mathrm{d} > \Delta H$ for the upstream coating gap, H_u, to remain positive. Because L_d is positive, the denominator of Equation (2.10) takes on a positive value for all the possible values of H_d. In addition, because L_d, L_u, and ΔH are positive, the numerator of Equation (2.10), $f(H_\mathrm{d})$, has two limits of different signs as H_d approaches the limiting values, as follows:

$$\lim_{H_\mathrm{d}\to\Delta H+} f(H_\mathrm{d}) = -2L_\mathrm{u}(\Delta H)^3 < 0, \tag{2.13}$$

$$\lim_{H_\mathrm{d}\to\infty} f(H_\mathrm{d}) = \infty. \tag{2.14}$$

According to the intermediate value theorem, a zero of Equation (2.10) exists in the open interval $(\Delta H, \infty)$. Hence, in the underbite configuration, the wet thickness at the weeping limit experiences a local minimum, as depicted in Figure 2.10. This result is *counterintuitive* in that it suggests the existence of an interval where the wet thickness decreases, even with an increasing coating gap. This property differentiates the underbite configuration from other configurations.

Overbite configuration ($\Delta H < 0$)

Finally, we consider the *overbite configuration* in which $\Delta H < 0$. Similar to the underbite case, the denominator of Equation (2.10) is positive, and hence nonzero for all $H_\mathrm{d} > 0$. It can be shown that the numerator $f(H_\mathrm{d})$ is nonzero for all H_d based on the following argument: First, the derivative of f with respect to H_d is expressed as

$$f'(H_\mathrm{d}) = 3(L_\mathrm{d} + L_\mathrm{u})(H_\mathrm{d} - \Delta H)^2 - 3L_\mathrm{u}(\Delta H)^2, \tag{2.15}$$

which is positive at $H_\mathrm{d} > 0$ because $\Delta H < 0$ in the overbite configuration. Therefore, we find that $f(H_\mathrm{d})$ increases monotonically in the same half-interval. Moreover, because $f(H_\mathrm{d} = 0) = -L_\mathrm{d}(\Delta H)^3 > 0$, we conclude that $f(H_\mathrm{d}) > 0$ and has no zeros when $H_\mathrm{d} > 0$. Therefore, under the overbite configuration, the derivative in Equation (2.10) is always positive; hence, as shown in Figure 2.11 h_w at the weeping limit increases monotonically, but not linearly, with H_d.

As shown in Figure 2.12, the results obtained from the 2-D computational model also agree well with the above trends. The maximum attainable wet thickness increases monotonically when the coating gap increases under the uniform and overbite

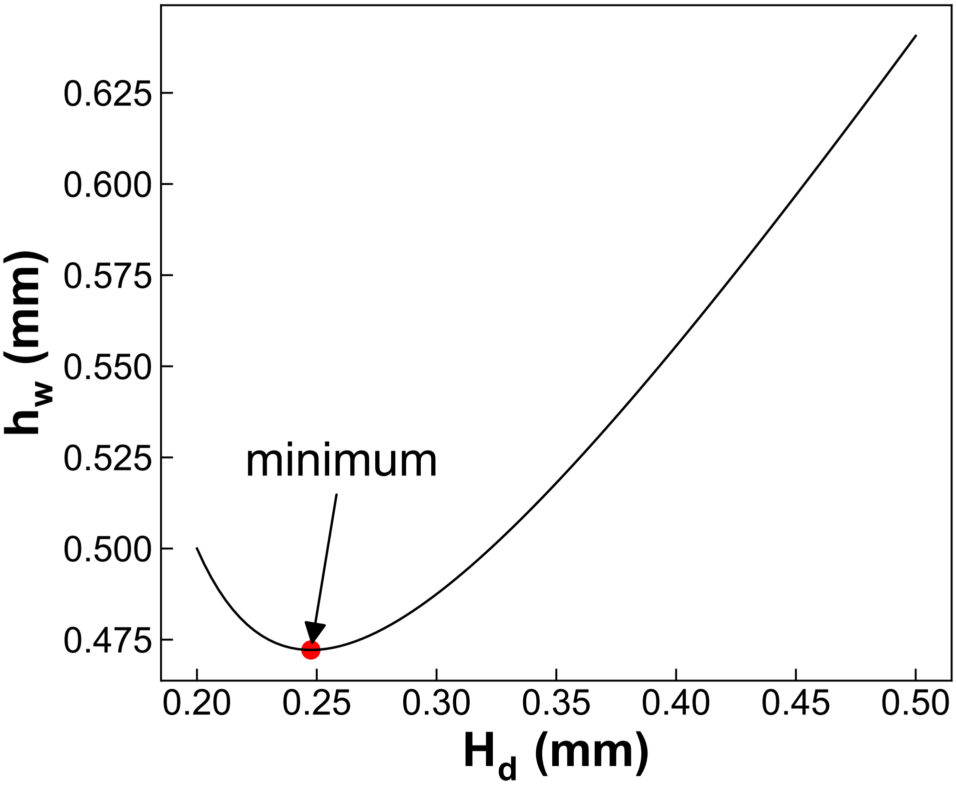

Figure 2.10: Dependence of wet thickness, h_{w}, on coating gap, H_{d}, at weeping limit under the underbite ($\Delta H = 0.1\,\mathrm{mm}$) configuration, derived from the simple model. Other parameters were $L_{\mathrm{d}} = L_{\mathrm{u}} = 1.0\,\mathrm{mm}$.

configurations, whereas it initially decreases when the coating gap increases before reaching a local minimum value under the underbite configuration.

The mean absolute relative errors of h_{w} at the weeping limit predicted by the simple model are 15.61%, 26.00%, and 4.965% for the uniform, underbite, and overbite configurations, respectively, under the given range of H_{d}. However, it should be noted that for all die configurations, the dependence of h_{w} on H_{d} is accurately captured by the simple model. For example, H_{d} at which the h_{w} experiences a local minimum under the overbite configuration is predicted as $0.2476\,\mathrm{mm}$ for the given

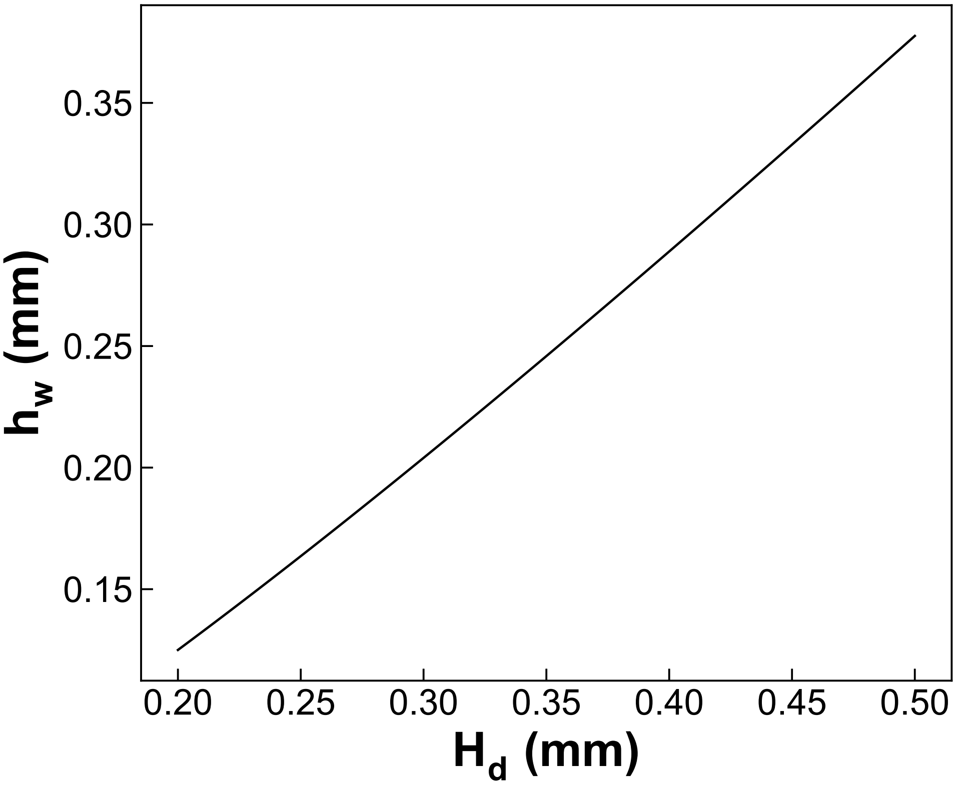

Figure 2.11: Dependence of wet thickness, h_{w}, on coating gap, H_{d}, at weeping limit under the overbite ($\Delta H = -0.2\,\mathrm{mm}$), derived from the simple model. Other parameters were $L_{\mathrm{d}} = L_{\mathrm{u}} = 1.0\,\mathrm{mm}$.

set of operating parameters, which is sufficiently close to the numerically computed value ($H_{\mathrm{d}} = 0.2450\,\mathrm{mm}$).

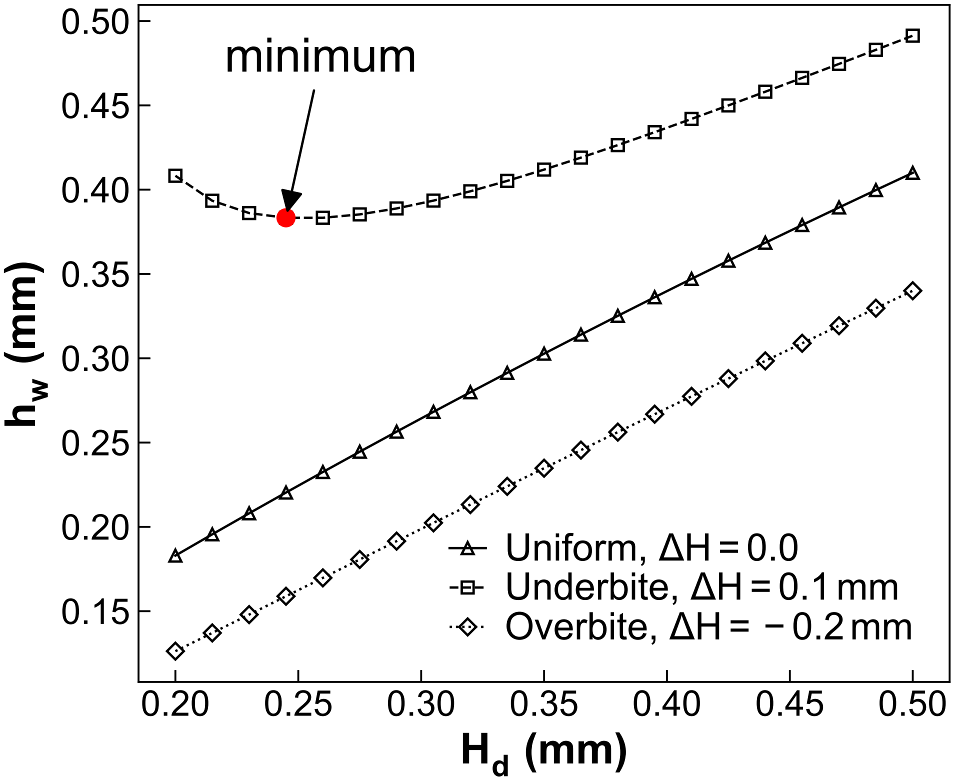

Figure 2.12: Dependence of wet thickness, h_{w}, on coating gap, H_{d}, at weeping limit under three different slot-die configurations: uniform (solid line with triangle marker, $\Delta H = 0$), underbite (dashed line with square marker, $\Delta H = 0.1\,\mathrm{mm}$), and overbite (dotted line with diamond marker, $\Delta H = -0.2\,\mathrm{mm}$), computed using the 2-D computational model. Parameters used are summarized in Table 2.1.

2.5 Conclusions

In this chapter, the coating gap dependencies of the maximum and minimum attainable wet thicknesses in the slot coating process under different slot-die configurations are studied and derived analytically. A simplified version of the viscocapillary model was used to derive an expression for the limiting wet thicknesses and their derivatives with respect to the coating gap.

It was revealed that the minimum wet thickness increases linearly with the coating gap, irrespective of the type of die configuration used. However, the dependence of the maximum wet thickness on the coating gap differed significantly for each configuration:

1. Uniform ($\Delta H = 0$): The wet thickness increases linearly with the coating gap, but with a different proportionality constant as compared with that in the minimum wet thickness case.
2. Underbite ($\Delta H > 0$): The wet thickness initially decreases as the coating gap increases. Eventually, it reaches a local minimum and then increases with the coating gap.
3. Overbite ($\Delta H < 0$): The wet thickness increases monotonically with the coating gap, but not linearly as it does in the uniform configuration case.

Since a wider coating gap allows a larger space between the slot-die and substrate, it is intuitive to expect a larger wet thickness with a wider coating gap. The significance of analysis presented in this chapter is that it demonstrates a case (underbite configuration) that contradicts this intuition.

Moreover, the 2-D governing equations were solved numerically for the wet thicknesses at the operating limits to verify the conclusions drawn from the simple model. The numerically computed dependence of the limiting wet thicknesses coincided with the trends observed in the analytically derived equations, proving the validity of the simple model.

Chapter 3

Conditions for vortex formation in slot coating flows

3.1 Introduction

As shown in Figure 3.1, vortices can form within the coating bead flow when certain operating conditions are met. Once formed, they can cause numerous problems such as particle aggregation, desorption of dissolved gas, and destruction of widthwise flow uniformity (Nam *et al.*, 2009), all of which severely interfere with the process operation and degrade the quality of final coated product. Vortices are also known to cause unwanted mixing of two layers in the two-layer slot coating process through a phenomenon known as the mid-gap invasion. (Nam & Carvalho, 2009) Thus it is important to figure out the range of operating conditions that lead to the formation of vortices in advance and avoid operating within that range.

Previous studies on the vortex formation condition in slot coating flows mostly focused on the flow of Newtonian fluids. For example, Sartor (1990) reported the evolution of vortices found in the coating bead flow as the flow rate, substrate speed, and coating gap are varied. Nam & Carvalho (2009) reported vortex formation near the interlayer of the two distinct coating fluids in the two-layer slot coating process as the flow rate of the bottom coating layer is changed. The two studies refer to a simple

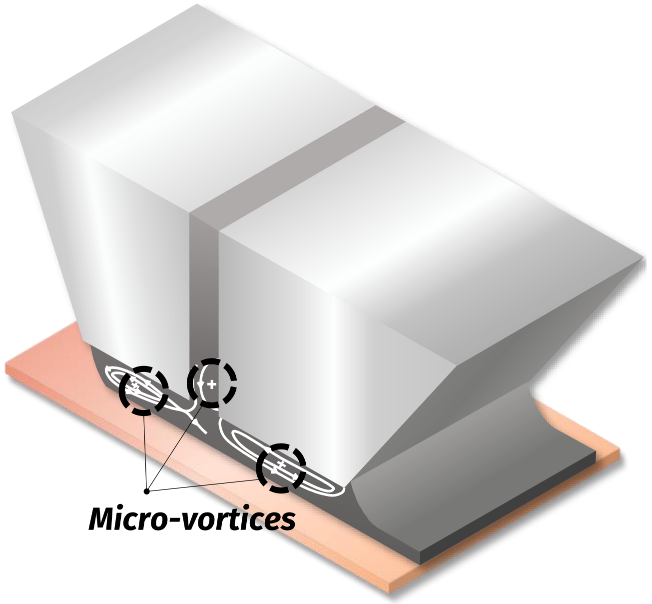

Figure 3.1: Microvortices found in the coating bead flow.

analytical criterion for the vortex formation, the so-called *one-third rule*. This rule indicates that, for the Newtonian coating fluids, vortices are found under the die-lip when the wet thickness is smaller than one-third of the coating gap.

The rheological properties of coating fluids used nowadays are becoming more and more complex with the growing demands on the higher performance of the film products. Thus, the Newtonian viscosity model alone is not enough to describe the complex behavior exhibited by the coating fluids exposed to high shear. For example, the lithium-ion battery electrode slurries are designed to exhibit different levels of viscosity under different range of shear rate (Li *et al.*, 2021). At low shear rates, high levels of viscosity slow down the rate of sedimentation and allow sharper edge to be formed in the wet film. At high shear rates, low viscosity is preferred to facilitate application of slurry to the substrate. To model this kind of fluid, a non-Newtonian constitutive equation has to be used to take account of the shear rate dependent viscosity.

In this chapter, we explore the vortex formation conditions for the slot coating flows of non-Newtonian fluids by using computational and analytical flow models. In the following sections, a two-dimensional (2-D) flow model is first introduced to compute the vortex formation conditions for the power-law fluids. One-dimensional (1-D) approximation of the coating flow is then applied to derive an analytical expression for the vortex formation in the downstream coating bead. Based on the derived expressions, an approximation method is developed and presented for the more general cases of generalized Newtonian fluids (GNFs). Finally, a semi-analytical method is introduced to compute the exact conditions for the GNFs. The problem of finding vortex formation condition is, under the definition from Section 1.2, of the second type, since specific conditions the flow has to follow are given and the goal is to find the operating parameters that induce those conditions.

3.2 Vortex formation condition in coating bead flow of power-law fluids

One of the simplest models that relates the shear rate and the viscosity is the power-law constitutive equation. It is used in this section to model the shear rate dependent viscosity of the given coating fluid. The viscosity, η, under power-law constitutive equation, can be expressed mathematically as follows:

$$\eta = K \left|\dot{\gamma}\right|^{n-1}, \tag{3.1}$$

where K and n are the flow consistency index and the power-law index, respectively. $|\dot{\gamma}|$ is the magnitude of the rate-of-strain tensor $\dot{\boldsymbol{\gamma}} = \nabla \mathbf{u} + (\nabla \mathbf{u})^\top$, given by $|\dot{\gamma}| = \sqrt{\frac{1}{2}\mathrm{II}_{\dot{\gamma}}}$, where $\mathrm{II}_{\dot{\gamma}}$ is the second invariant of $\dot{\boldsymbol{\gamma}}$, i.e., $\mathrm{II}_{\dot{\gamma}} = (\dot{\boldsymbol{\gamma}} : \dot{\boldsymbol{\gamma}}) = \sum_i \sum_j \dot{\gamma}_{ij}\dot{\gamma}_{ji}$.

In the following, we develop a two-dimensional flow model to track the vortex formation conditions in slot coating flows of power-law fluids.

3.2.1 Two-dimensional (2-D) computational flow model

Governing equations and boundary conditions

The steady flow of an incompressible fluid under negligible body forces is governed by the following mass and momentum balances:

$$\nabla \cdot \mathbf{u} = 0, \tag{3.2}$$

$$\rho \mathbf{u} \cdot \nabla \mathbf{u} = \nabla \cdot \mathbf{T}, \tag{3.3}$$

$$\mathbf{T} = -p\mathbf{I} + \eta(|\dot{\gamma}|)\dot{\boldsymbol{\gamma}}, \tag{3.4}$$

where $\mathbf{u}$, p, ρ, $\mathbf{I}$, and $\mathbf{T}$ are velocity, pressure, density, identity tensor, and total stress tensor, respectively.

Unlike the fixed die-lip surfaces or the moving substrate, the position of two menisci of the coating bead is not determined *a priori*. To pose the problem in a known domain so that standard measures for solving boundary value problems can be applied, the unknown physical domain, $\mathbf{x} = (x, y)$, is mapped into a fixed reference domain, $\boldsymbol{\xi} = (\xi, \eta)$, via a transformation $\mathbf{x} = \mathbf{x}(\boldsymbol{\xi})$. The inverse transformation is defined by the following system of elliptic partial differential equations as described by de Santos (1991)

$$\nabla \cdot D_\xi(\xi, \eta)\nabla\xi = 0, \quad \nabla \cdot D_\eta(\xi, \eta)\nabla\eta = 0, \tag{3.5}$$

where D_ξ and D_η are mesh diffusivities that control the distribution of nodes along the curves of constant ξ and η. These curves define the boundaries of elements that comprise the domain while the points where they intersect defines the position of the nodes. An instance of generated mesh determined by conducting a mesh convergence test, together with the number of elements, the number of nodes, and degree of freedom, is illustrated in Figure 3.2.

Geometrical parameters and boundary conditions associated with the governing equations are summarized in Figure 3.3. Note that a Dirichlet-type boundary con-

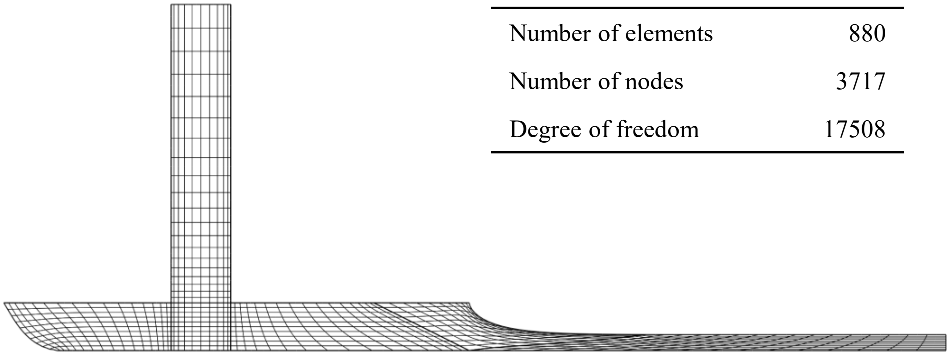

Number of elements	880
Number of nodes	3717
Degree of freedom	17508

Figure 3.2: Computational mesh used for 2-D flow model.

dition is applied at the inflow boundary by specifying the velocity profile. We used the Newtonian velocity profile obtained by prescribing the flow rate and imposing no-slip conditions on each side of the feed slot wall, instead of obtaining the fully developed velocity profile for each value of power-law index n. This choice ensures that an exact value of flow rate is specified at the inlet boundary. To guarantee that the parabolic profile reaches the fully-developed state before exiting the feed slot, we set the feed slot length L_{fl} to be five times that of the feed slot height L_{fh}, and verified the length to be sufficiently larger than the entrance length.

The operating conditions are summarized in Table 3.1. Base case parameters are used in the computations unless otherwise stated. Under these settings, with $K(U_{\mathrm{w}}/H_{\mathrm{g}})^{n-1}$ as the characteristic viscosity and H_{g} as the characteristic length, the Reynolds number of the system is calculated as 9.85. Therefore, the flow is deemed to be laminar and no eddies associated with turbulence is expected to be found.

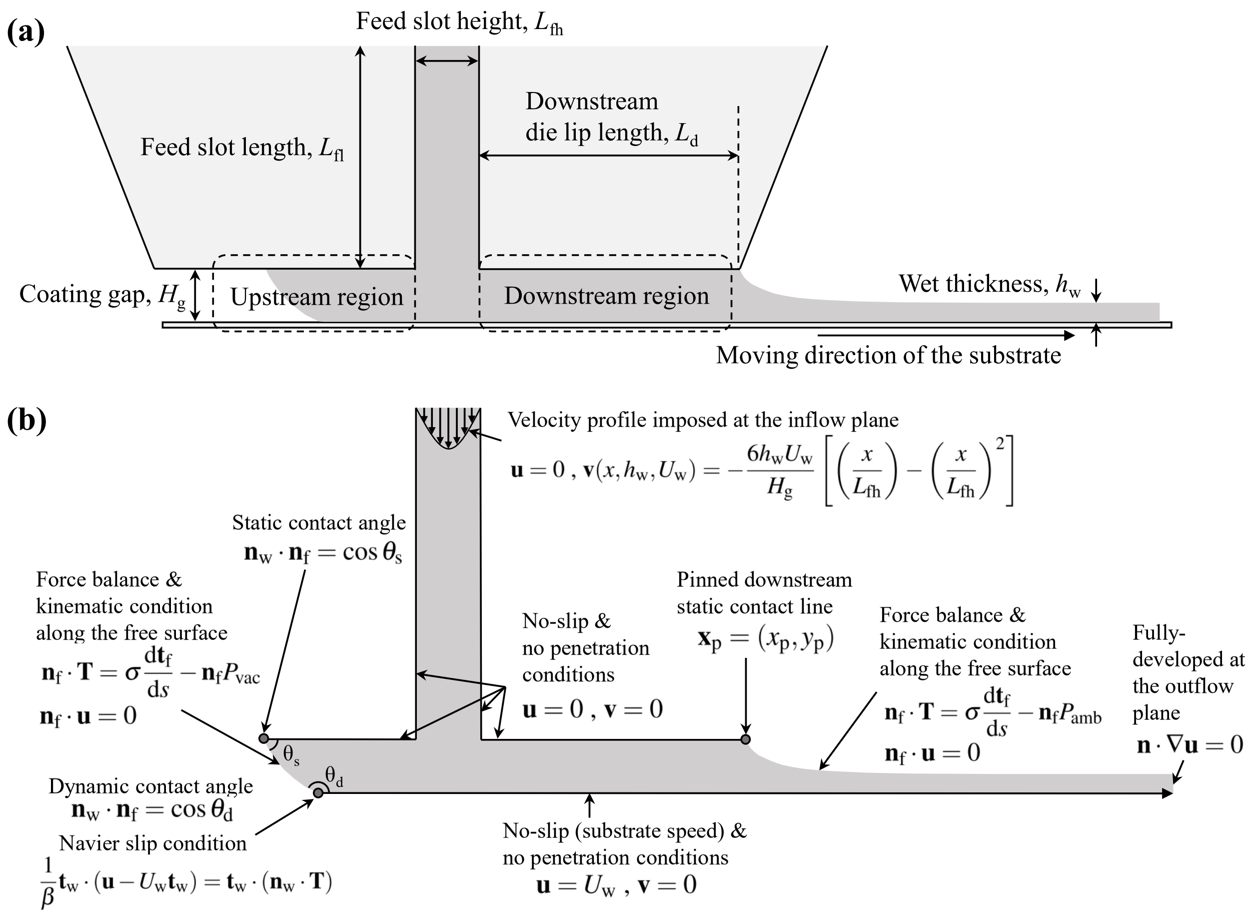

Figure 3.3: (a) Schematic diagram of the coating bead flow. (b) Boundary conditions associated with the governing equations.

Table 3.1: Operating conditions and geometric parameters used in 2-D computational flow model.

Operating parameters	Unit	Base case	Range
Density (ρ)	$\mathrm{g/cm^3}$	1.59	-
Surface tension (σ)	$\mathrm{mN/m}$	40	-
Substrate speed (U_w)	$\mathrm{mm/s}$	1200	-
Static contact angle (θ_s)	$^\circ$	60	-
Dynamic contact angle (θ_d)	$^\circ$	160	-
Flow rate per width (q)	$\mathrm{mm^2/s}$	-	88.98 - 142.0
Vacuum pressure (P_vac)	Pa	7000	0 - 7000
Flow consistency index (K)	$\mathrm{Pa \cdot s}^n$	$3.0 \times (1200/0.2)^{0.5-n}$	-
Power-law index (n)	dimensionless	-	0.5 - 1.5
Geometric parameters	Unit	Base case	Range
Downstream die lip length (L_d)	mm	1.0	-
Feed slot height (L_fh)	mm	0.25	0.1 - 0.5
Feed slot length (L_fl)	mm	1.25	0.5 - 2.5
Coating gap (H_g)	mm	0.2	-

Mathematical expressions for vortex birth

To solve the given problem, we additionally require the mathematical expressions that describe the vortices. According to Nam *et al.* (2009) with an appropriate choice of reference frame, the axis of rotation, or the vortex center, is at rest relative to the observer. For one to identify vortices in flows, it is required to examine the flow field in the vicinity of the stagnation points. Steady fluid parcel motion near the stagnation point $\mathbf{x}_0$ can be expressed using Taylor expansion as

$$\frac{\mathrm{D}\mathbf{x}}{\mathrm{D}t} = \mathbf{u}(\mathbf{x}) = \mathbf{u}(\mathbf{x}_0) + \delta\mathbf{x} \cdot \nabla\mathbf{u}(\mathbf{x}_0) + \frac{1}{2}\delta\mathbf{x}\delta\mathbf{x} : \nabla\nabla\mathbf{u}(\mathbf{x}_0) + \mathcal{O}(\delta\mathbf{x}^3), \tag{3.6}$$

where $\delta\mathbf{x} = \mathbf{x} - \mathbf{x}_0$ and $\mathbf{u}(\mathbf{x}_0) = 0$. If $\mathbf{x}_0$ is a saddle point from which liquids flow in and out, the determinant of the velocity gradient is negative, i.e., $\det \nabla\mathbf{u}(\mathbf{x}_0) < 0$. On the contrary, if $\mathbf{x}_0$ is a vortex center, $\det \nabla\mathbf{u}(\mathbf{x}_0) > 0$. Therefore, the vortex birth conditions are

$$\mathbf{u}(\mathbf{x}_0) = 0 \quad \text{and} \quad \det \nabla\mathbf{u}(\mathbf{x}_0) = 0. \tag{3.7}$$

However, $\mathbf{u}(\mathbf{x}_0) = 0$ holds by default for every point on an impermeable stationary wall, requiring one to examine the second-order term in Equation (3.6) when identifying the vortices born along the wall. With a proper choice of time unit, the singular character at the wall can be eliminated from the equation, allowing conditions for vortex generation along the wall to be derived as

$$\dot{\gamma}_\mathrm{s} = \frac{1}{2}\frac{\partial u_\mathrm{t}}{\partial s_\mathrm{n}} = 0 \quad \text{and} \quad \frac{\partial \dot{\gamma}_\mathrm{s}}{\partial s_t} = 0, \tag{3.8}$$

where the relative position and velocity are expressed in terms of the local orthogonal coordinate system, i.e., $\mathbf{x} = \mathbf{t}s_t + \mathbf{n}s_\mathrm{n}$ and $\mathbf{u} = \mathbf{t}u_\mathrm{t} + \mathbf{n}u_n$, where $\mathbf{t}$ and $\mathbf{n}$ are unit tangent and normal vector to the solid wall surface.

3.2.2 Solution methods

The Galerkin finite element method (G/FEM) is used to discretize and solve for Equations (3.2)-(3.4) coupled with (3.5), which serves as a mesh generation equation upon discretization. The field variables (velocity, pressure, and nodal position) are represented as finite linear combinations of known basis functions

$$\mathbf{u} = \sum_j \mathbf{u}_j \phi_j(\xi, \eta), \tag{3.9}$$

$$p = \sum_k P_k \psi_k(\xi, \eta), \tag{3.10}$$

$$\mathbf{x} = \sum_j \mathbf{x}_j \phi_j(\xi, \eta). \tag{3.11}$$

Lagrangian biquadratic basis functions ϕ_j are used to express velocity and nodal position, and linear discontinuous basis functions ψ_k to express the pressure. The unknown basis function coefficients $\mathbf{u}_j$, P_k, and $\mathbf{x}_j$ comprises the solution vector $\mathbf{z}$, and is obtained by solving the discretized governing equations.

Equations (3.2), (3.3), and (3.5) are multiplied with weighting functions and integrated over the flow domain, to obtain the following weighted residuals

$$\mathbf{R}_{\mathrm{c}} = \int_\Omega \psi_k \nabla \cdot \mathbf{u} \, \mathrm{d}\Omega, \tag{3.12}$$

$$\mathbf{R}_{\mathrm{m}} = \int_\Omega (\phi_j \rho \mathbf{u} \cdot \nabla \mathbf{u} + \nabla \phi_j \cdot \mathbf{T}) \, \mathrm{d}\Omega - \int_\Gamma \phi_j \mathbf{n} \cdot \mathbf{T} \, \mathrm{d}\Gamma, \tag{3.13}$$

$$\mathbf{R}_{\mathrm{x}} = -\int_\Omega \nabla \phi_j \cdot \mathbf{D} \cdot \nabla \boldsymbol{\xi} \, \mathrm{d}\Omega + \int_\Gamma \phi_j \mathbf{n} \cdot \mathbf{D} \cdot \nabla \boldsymbol{\xi} \, \mathrm{d}\Gamma. \tag{3.14}$$

Here, $\mathbf{D} = (D_\xi, D_\eta)$ and $\boldsymbol{\xi} = (\xi, \eta)$. Weighting functions are the same as basis functions in Galerkin's method. The divergence theorem was applied where possible, and Ω and Γ represent the flow domain and the domain boundary. The subscripts m, c, and x represent momentum, continuity, and mesh residuals, respectively.

The constructed weighted residuals can be viewed as a discretized and reduced version of the original partial differential equations governing the system. They form a system of nonlinear algebraic equations, in terms of the unknown basis function coefficients $\mathbf{z}$ and known system parameters $\boldsymbol{\lambda}$, as

$$\mathbf{R}(\mathbf{z}, \boldsymbol{\lambda}) = 0. \tag{3.15}$$

This system of equations is solved iteratively by linearizing the equations at each step (i.e., by Newton's method). In this analysis, the iteration is considered to have converged when the L_2-norm of the residual vector, $\|\mathbf{R}(\mathbf{z}, \boldsymbol{\lambda})\|_2$, falls below 10^{-7}.

Direct tracking of vortex birth conditions

The procedure described above are applicable in cases where the values for all the system parameters, $\boldsymbol{\lambda}$, are specified, and the goal is to obtain the solution vector $\mathbf{z}$; i.e. when the problem is of the first type, as described in Section 1.2. However, the problem covered in this chapter is of the second type, which requires a somewhat different approach.

We use the *direct tracking algorithm*, as described by Nam *et al.* (2009), to track the vortex birth condition under different system parameters (e.g., the prescribed flow rate or the vacuum pressure). In the following, the procedures involved in the algorithm is briefly outlined.

If the obtained solution is to meet specific, sought-after conditions (vortex birth for example), the solution must satisfy extra equations describing such conditions in addition to the original governing equations. These newly introduced equations are called the augmented equations. Some formerly fixed parameters must be "set free" so that the field variables can shift to meet the new requirements. These parameters serve as the new unknowns for the augmented equations. For the present study, Equations (3.7) and (3.8) are used as the augmented equation to seek vortex birth conditions. The extra unknowns are the position of the vortex center (or the stagnation point) and the operating parameter to adjust. The augmented equations, together with the weighted residuals of the governing equations, Equation (3.15), form an augmented system of equations:

$$\begin{cases} \mathbf{R}(\mathbf{z}, \boldsymbol{\lambda}, \mathbf{p}) = 0, \\ \mathbf{A}(\mathbf{z}, \boldsymbol{\lambda}, \mathbf{p}) = 0, \end{cases} \tag{3.16}$$

where $\mathbf{A}$ and $\mathbf{p}$ denote augmented equations and the set of auxiliary parameters for the system to satisfy given conditions. Once again, this system of nonlinear equations is solved iteratively by Newton's method for the basis function coefficients $\mathbf{z}$ and the extra auxiliary parameters $\mathbf{p}$.

After obtaining the solution with a fixed set of parameters $\boldsymbol{\lambda}$, the algorithm moves on to the next stage to seek solutions under other sets of parameters. This multiparameter continuation stage consists of three smaller steps. First, the parameter, whose effect we are interested in, is changed, i.e., $\beta_{(i+1)} = \beta_{(i)} + \delta\beta$, where $\delta\beta$ is the increment or the decrement made on the parameter and the index i indicates the i-th continuation step. Next, in the predictor step, the sensitivities of $\mathbf{z}$ and $\mathbf{p}$ to the parameter β are computed and a "good" initial guess is obtained by a tangent predictor as $\mathbf{A}_{(i+1)} = \mathbf{A}_{(i)} + \delta\beta(\partial\mathbf{A}_{(i)}/\partial\beta)$, where $\mathbf{A}$ stands for either $\mathbf{z}$ or $\mathbf{p}$. Lastly, in the corrector step, Equation (3.16), now with changed β, is solved using Newton's method with the initial guess obtained from the previous step. For this analysis, the tolerance on the L_2-norm of the augmented residual vector is set as 10^{-7}. We relaxed the tolerance up to 10^{-6} for low values of n near 0.5. With the multiparameter continuation performed over the entire range of β that we are interested in, we obtain the complete set of solutions that satisfy the given conditions with different values of β.

3.2.3 Results and discussion

Vortices found in the coating bead flow are classified into two categories according to the location of their births: (i) on the stationary wall and (ii) within the flow, as illustrated in Figure 3.4. The former is observed in the downstream region of the coating bead with non-zero flow rate (Sartor, 1990; Nam *et al.*, 2009), while the latter is usually encountered in the upstream region where the net flow rate is zero (Nam *et al.*, 2009). In the following, we present the results of applying the direct tracking algorithm to both regions and discuss the effect of shear dependent viscosity on the vortex formation conditions.

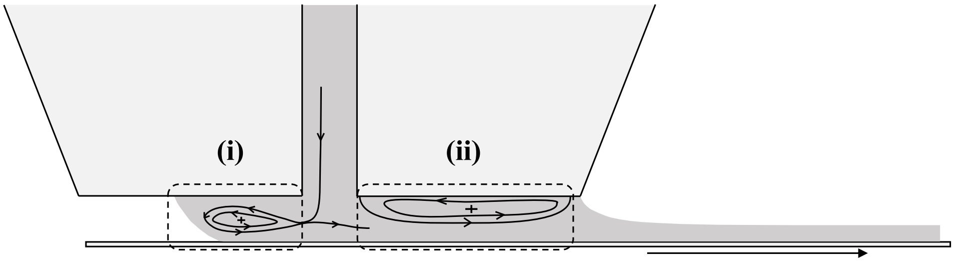

Figure 3.4: Two different types of vortices found in the slot coating flow: (i) within the flow and (ii) on the die-lip surface.

Vortex birth in upstream region

It is a common practice to apply vacuum pressure to the liquid-gas interface in the upstream region to stabilize the coating bead flow by pulling the interface away from the feed slot (Sartor, 1990; Carvalho & Kheshgi, 2000). Increasing the flow rate shows a similar effect, by pushing the interface toward the upstream direction. Higher vacuum and flow rate both results in a larger pressure difference between the interface and the exit of the feed slot. Thus, an increase in both parameters lead to an increased length of the upstream coating bead. It is reported that a vortex in the upstream bead is born from the cusp point within the flow when the bead length grows sufficiently long (Nam *et al.*, 2009).

Vortices formed in the upstream region are born within the flow. Consequently, we choose Equation (3.7) to be the augmented equation. Since both vacuum pressure and prescribed flow rate can lead to the birth of vortex in the upstream region, either of the two operating conditions can serve as one of the auxiliary parameters. In this section, we choose vacuum pressure to be the auxiliary parameter, i.e., its magnitude is automatically determined through the direct tracking algorithm. Therefore, the set of auxiliary parameters $\mathbf{p}$ in Equation (3.16) is comprised of the vacuum pressure and the coordinates of the stagnation point $\mathbf{x}_0$, which coincide with the location of vortex birth. The continuation was performed on the power-law index n and the dimensionless flow rate to examine their effects on the vortex birth in the upstream region.

Figure 3.5(a) illustrates the result of the parameter continuation on the dimensionless flow rate. Under a fixed value of power-law index n, the dimensionless flow rate decreases as the dimensionless vacuum pressure increases, as both conditions have a similar effect on the length of the upstream coating bead. From an engineering point of view, this means that the use of vacuum pressure restricts the maximum thickness of the film produced, if the vortices are to be avoided in the upstream coating bead flow.

Under a fixed value of the flow rate, the vacuum pressure required for vortex birth generally increases with the increasing power-law index n, as depicted in Figure 3.5(b). However, as the dimensionless flow rate approaches the critical value of approximately 0.62, the vacuum pressure at the moment of vortex birth vanishes regardless of the power-law index n, as shown in curve (iii) of Figure 3.5(b). This observation implies that the vortices are likely to be found in coating flows with a flow rate above this critical value, even in the absence of vacuum pressure. Note that Figures 3.5(a) and (b) both represent hyperplanes of the same surface residing in the three-dimensional parametric space consisted of dimensionless vacuum pressure, flow rate, and power-law index n.

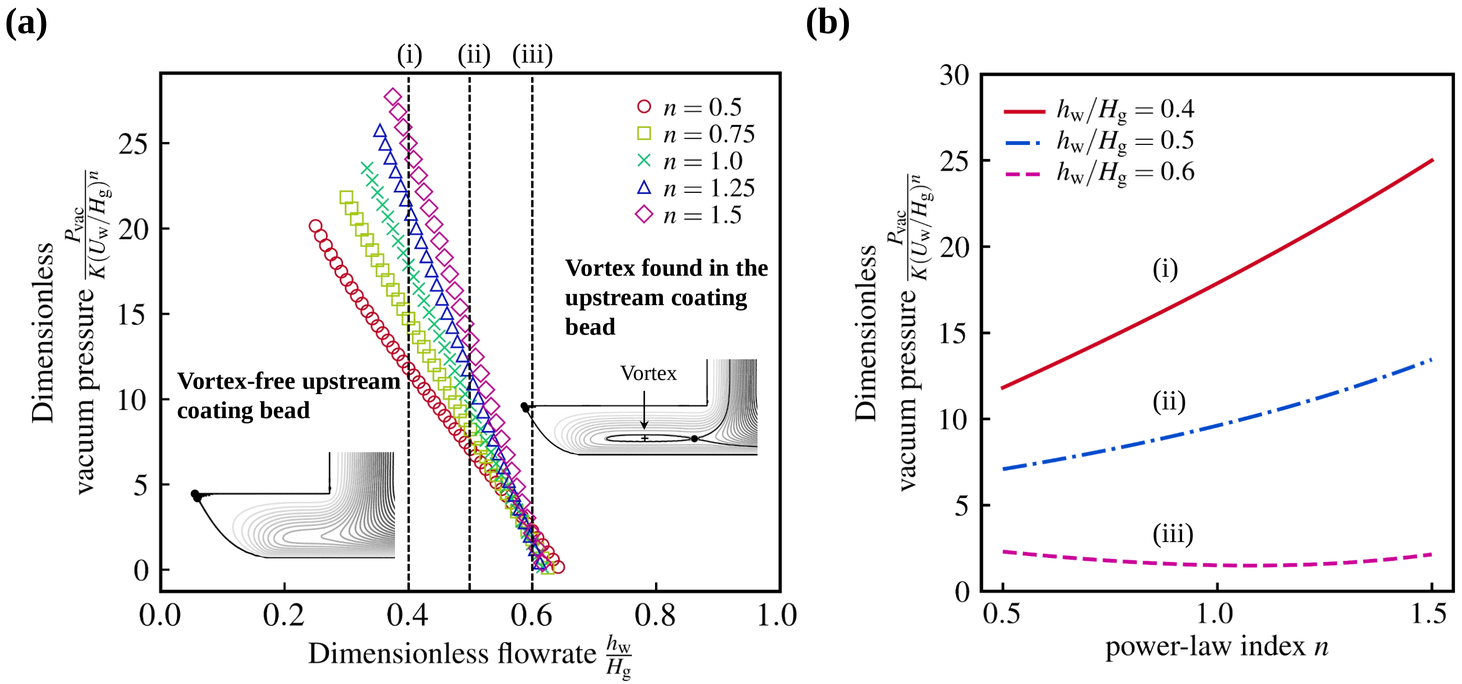

Figure 3.5: Dimensionless vacuum pressure at the moment of vortex birth in the upstream region (a) as a function of dimensionless flow rate at different values of power-law index n and (b) as a function of power-law index n at different values of dimensionless flow rates.

Vortex birth in downstream region

In the downstream region, the net flow rate is equal to the predetermined flow rate per unit width, $q = h_{\mathrm{w}}U_{\mathrm{w}}$, assuming that no coating liquid is lost through evaporation or leakage during the process. Since vortices are formed on the stationary downstream die lip, Equation (3.8) is used as the augmented equation appearing in Equation (3.16). Since the vacuum pressure plays no role in determining the onset of vortex formation in this region, we choose only the prescribed flow rate q and the location of the vortex birth to be the extra auxiliary parameters $\mathbf{p}$ in Equation (3.16). To examine the effect of shear-rate dependent viscosity on the vortex birth condition, n is used as the continuation parameter, i.e., $\beta = n$.

Figure 3.6 illustrates the dimensionless flow rate $h_{\mathrm{w}}/H_{\mathrm{g}}$ at the moment of vortex birth, as predicted by the direct tracking algorithm when the power-law index n is varied from 0.5 to 1.5. It is evident from the plot that there is a clear relationship between the vortex formation condition, expressed in terms of the dimensionless flow rate, and the power-law index n. Also, it should be noted that the *one-third rule* discussed in Section 3.1 is verified by the numerical results when $n = 1$, as marked in Figure 3.6.

These observations motivated us to search for an analytical expression that can predict the vortex formation conditions in the downstream region for the slot coating flows of the power-law fluids, just like what *one-third rule* does for the Newtonian fluids. The derivation and findings are presented in the following section.

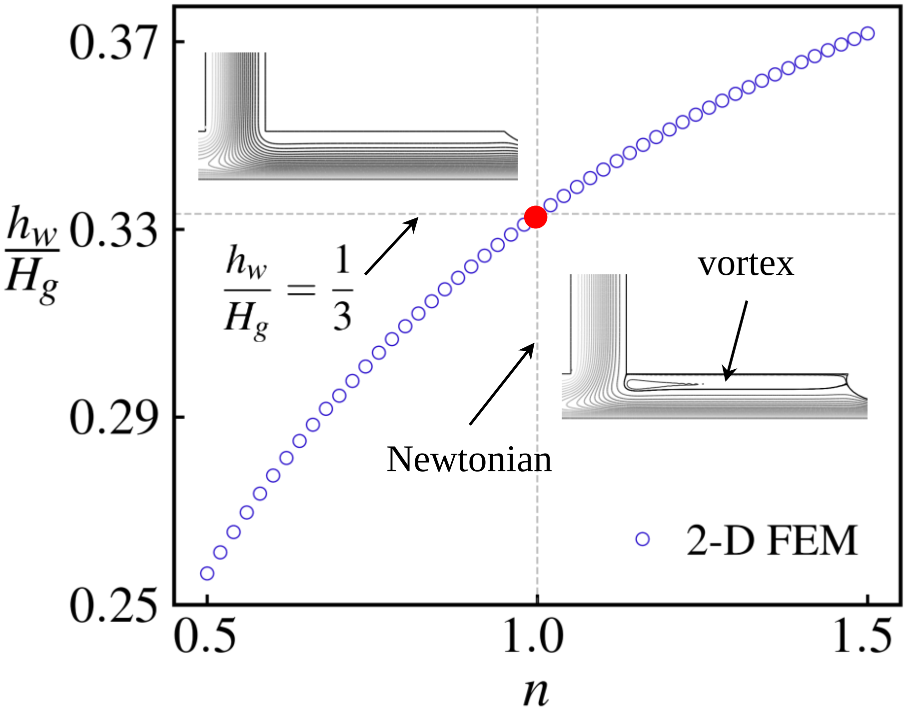

Figure 3.6: Dimensionless flow rate $h_{\mathrm{w}}/H_{\mathrm{g}}$ at the moment of vortex birth (from 2-D FEM computations) plotted against the power-law index n. Note that the *one-third rule* is recovered when $n = 1$.

3.3 Flow reversal condition in one-dimensional flow model

The flow in the downstream region is highly rectilinear in nature, which allows it to be approximated as a fully-developed one-dimensional (1-D) rectilinear flow between a pair of moving and stationary walls. This type of flow is often referred to as Couette–Poiseuille flow (C-P), owing to the two distinct driving forces for the fluid motion: the viscous force due to the shearing motion between the moving and stationary plate and the pressure gradient imposed along the streamwise direction. With these assumptions, the approximated 1-D C-P flow becomes tractable for analysis in a coordinate system as depicted in Figure 3.7.

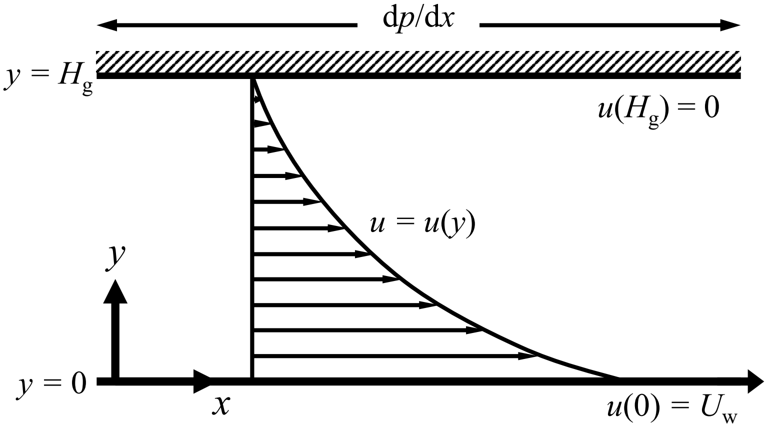

Figure 3.7: Configuration of the planar Couette–Poiseuille (C-P) flow considered in 1-D flow analysis.

Vortices, in a 1-D flow domain, are characterized by the presence of flow reversal. The description of motion in such a space is limited due to the lack of cross-flow component, and a flow reversal is indistinguishable from a vortex in the flow domain. Therefore, in this section, the goal is to search for the onset condition of flow reversal in 1-D C-P flow which, hopefully, provides an useful prediction of the actual vortex birth conditions in the 2-D flow.

3.3.1 Mathematical formulation

Since the flow is fully-developed, the fluid velocity u is independent of the flow direction and only dependent on y. The pressure gradient dp/dx, as a result, is also constant along the flow direction. The plate located at $y = 0$ is moving in the x-direction with a constant velocity U_{w}, while the plate at $y = H_{\mathrm{g}}$ remains still. Here, H_{g} is the channel height.

We introduce the following dimensionless variables,

$$\tilde{u} = \frac{u}{U_{\mathrm{w}}}, \quad \tilde{y} = \frac{y}{H_{\mathrm{g}}}, \quad P = \frac{\mathrm{d}\tilde{p}}{\mathrm{d}\tilde{x}} = \frac{\mathrm{d}p}{\mathrm{d}x}\frac{H_{\mathrm{g}}}{K(U/H_{\mathrm{g}})^n}. \tag{3.17}$$

With these variables substituted and tilde sign omitted, Equations (3.2)-(3.4), and (3.1) are reduced to

$$\frac{\mathrm{d}}{\mathrm{d}y}\left(\left|\frac{\mathrm{d}u}{\mathrm{d}y}\right|^{n-1}\frac{\mathrm{d}u}{\mathrm{d}y}\right) = P, \tag{3.18}$$

which is subject to the following no-slip boundary conditions

$$\begin{aligned} u &= 1 \quad \text{at} \quad y = 0, \\ u &= 0 \quad \text{at} \quad y = 1. \end{aligned} \tag{3.19}$$

Note that the scaling factor $K(U_{\mathrm{w}}/H_{\mathrm{g}})^n$ in Equation (3.17) is the characteristic stress under a simple shearing motion. The unknown pressure gradient P is determined by the following mass conservation equation:

$$\int_0^1 u \,\mathrm{d}y = \frac{q}{U_{\mathrm{w}}H_{\mathrm{g}}} = Q. \tag{3.20}$$

Here, q is the prescribed flow rate per unit width and Q is the dimensionless flow rate.

By integrating Equation (3.18) we obtain

$$\left|\frac{\mathrm{d}u}{\mathrm{d}y}\right|^{n-1}\frac{\mathrm{d}u}{\mathrm{d}y} = (y - c_1)P, \tag{3.21}$$

where c_1 is the constant of integration and also the vertical position where the flow exhibits a zero shear-rate.

As mentioned by Ross *et al.* (1999), differential equations involving absolute values should be dealt with carefully, as different signs may yield distinct solutions. Therefore, two remarks must be considered to solve Equation (3.21). A close inspection of the equation reveals that the sign of shear rate $\mathrm{d}u/\mathrm{d}y$ coincides with that of $(y-c_1)P$. Moreover, $\mathrm{d}u/\mathrm{d}y$ is an odd function with respect to $y = c_1$, which implies that $u(y)$ is an even function (as shown in Figure 3.8).

To make use of this property, in this analysis, we assume $\mathrm{d}u/\mathrm{d}y \geq 0$ and solve for Equation (3.21) in a single side of the symmetry plane, $y > c_1$ or $y < c_1$, depending on the sign of P. Since $u(y)$ is symmetric with respect to $y = c_1$, the other half (where $\mathrm{d}u/\mathrm{d}y < 0$) is obtained effortlessly by reflection. The boundary conditions are then applied to restrict the flow to the appropriate domain. Note that in the absence of the pressure gradient, i.e., $P = 0$, the solution is a pure Couette type flow $u(y) = 1 - y$, with a dimensionless flow rate of $Q = 1/2$.

Previous studies, e.g., Flumerfelt *et al.* (1969), adopted two different approaches to derive the velocity profile depending on the existence of a maximum or minimum of the velocity profile within the flow domain. Our approach differs in that a single expression is derived for the velocity profile, regardless of the position of c_1.

When the prescribed dimensionless flow rate is less than $1/2$, there exists an adverse pressure gradient ($P > 0$) along the channel, and Equation (3.21) is rearranged as

$$\frac{\mathrm{d}u}{\mathrm{d}y} = P^{\frac{1}{n}}(y - c_1)^{\frac{1}{n}}. \tag{3.22}$$

Upon integration and application of the symmetry condition, the velocity profile is obtained as

$$u(y) = P^{\frac{1}{n}} \frac{n}{n+1} |y - c_1|^{\frac{1}{n}} + c_2, \tag{3.23}$$

where c_2 is another constant of integration. Note that with the symmetry condition applied, this profile is valid throughout the entire domain. Two unknowns, P and c_2, are eliminated from the equation by applying boundary conditions, Equation (3.19):

$$u(y) = \frac{|1 - c_1|^{\frac{n+1}{n}} - |y - c_1|^{\frac{n+1}{n}}}{|1 - c_1|^{\frac{n+1}{n}} - |c_1|^{\frac{n+1}{n}}}. \tag{3.24}$$

The dimensionless pressure gradient P is also expressed in terms of c_1,

$$P^{\frac{1}{n}} = \frac{(n+1)/n}{|c_1|^{\frac{n+1}{n}} - |1 - c_1|^{\frac{n+1}{n}}}. \tag{3.25}$$

The velocity profile and the pressure gradient are expressed in terms of an undetermined constant c_1. It is finally determined through Equation (3.20) numerically, with a given dimensionless flow rate Q.

A same mathematical formulation for the case of forward pressure gradient, i.e., $P < 0$, leads to the velocity profile identical to Equation (3.24) and the pressure gradient expressed in terms of c_1 as

$$-(-P)^{\frac{1}{n}} = \frac{(n+1)/n}{|c_1|^{\frac{n+1}{n}} - |1-c_1|^{\frac{n+1}{n}}}. \tag{3.26}$$

With the velocity profile and pressure gradient obtained, it is possible to classify the flow into four states, as depicted in Figure 3.8. The sign of P separates flow states into two groups, I-II ($P > 0$) and III-IV ($P < 0$). The value of c_1 is used to distinguish different states within each group. Consequently, c_1, the location of zero shear rate, uniquely determines flow states.

In this analysis, explicit expressions for the limiting flow rate conditions are established and used as the criteria for distinguishing different flow states. Flumerfelt *et al.* (1969) and Malik & Shenoy (1991) classified the C-P flow into different states in a similar manner, but only in terms of the dimensionless pressure gradients. Since P is uniquely determined by Q through Equations (3.20) and (3.24)-(3.26), the same criteria that distinguish between different flow states can be expressed in terms of Q as well.

To obtain the conditions for limiting cases, c_1, the location of zero shear rate, in Equation (3.24) is set to the boundary of the domain, i.e., $c_1 = 0$ and $c_1 = 1$. The velocity profile is then substituted into Equation (3.20) to obtain the dimensionless flow rate in each case. The resultant limiting flow rate and pressure gradient pairs are

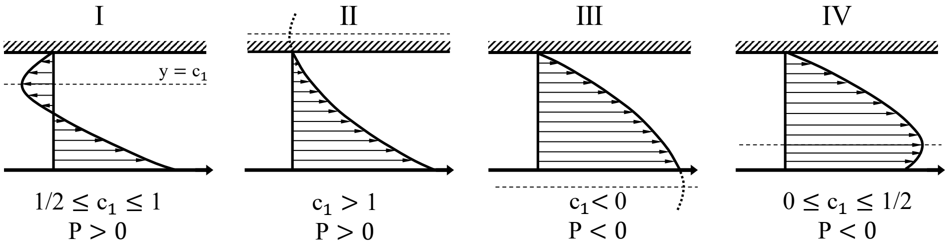

Figure 3.8: Four distinguishing flow states, dependent on operating conditions. Here, $y = c_1$, shown as the dashed line, is the position of zero shear rate, and P is the dimensionless pressure gradient.

expressed as

$$Q = \frac{n}{2n+1} \quad \text{and} \quad P = \left(\frac{n+1}{n}\right)^n \qquad \text{(Adverse pressure gradient)}, \tag{3.27}$$

$$Q = \frac{n+1}{2n+1} \quad \text{and} \quad P = -\left(\frac{n+1}{n}\right)^n \qquad \text{(Forward pressure gradient)}. \tag{3.28}$$

Note that the pressure gradient condition is identical to that derived in the previous study (Flumerfelt *et al.*, 1969). Following these criteria, the conditions for each flow state are developed and are listed in Table 3.2, and are depicted in Figure 3.9.

Equation (3.27) sets the boundary between flow states I and II, and is the most important to the present analysis as it marks the onset of the flow reversal. As previously mentioned, this may imply the generation of vortices in the downstream region of the slot coating flow. It is also clear from Equations (3.27) and (3.28) that the critical conditions are dependent solely on the power-law index n, as illustrated in Figure 3.9.

3.3.2 Comparison with 2-D model

In the downstream region of the coating bead flow, $q = h_\mathrm{w} U_\mathrm{w}$ holds by mass conservation, where h_w stands for the wet thickness of the coated film and q is the

Table 3.2: Dimensionless velocity profile, pressure gradient, and flow rate conditions for different flow states in 1-D C-P flow of power-law fluids.

Flow state	I	II
Velocity profile	$\frac{(1-c_1)^{\frac{n+1}{n}}-\lvert y-c_1\rvert^{\frac{n+1}{n}}}{(1-c_1)^{\frac{n+1}{n}}-c_1^{\frac{n+1}{n}}}$	$\frac{(c_1-1)^{\frac{n+1}{n}}-(c_1-y)^{\frac{n+1}{n}}}{(c_1-1)^{\frac{n+1}{n}}-c_1^{\frac{n+1}{n}}}$
Flow rate	$Q < \frac{1}{2} - \frac{1}{2(2n+1)}$	$\frac{1}{2} - \frac{1}{2(2n+1)} < Q < \frac{1}{2}$
Pressure gradient	$P > \left(\frac{n+1}{n}\right)^n$	$0 < P < \left(\frac{n+1}{n}\right)^n$
Flow state	**III**	**IV**
Velocity profile	$\frac{(1-c_1)^{\frac{n+1}{n}}-(y-c_1)^{\frac{n+1}{n}}}{(1-c_1)^{\frac{n+1}{n}}-(-c_1)^{\frac{n+1}{n}}}$	$\frac{(1-c_1)^{\frac{n+1}{n}}-\lvert y-c_1\rvert^{\frac{n+1}{n}}}{(1-c_1)^{\frac{n+1}{n}}-c_1^{\frac{n+1}{n}}}$
Flow rate	$\frac{1}{2} < Q < \frac{1}{2} + \frac{1}{2(2n+1)}$	$\frac{1}{2} + \frac{1}{2(2n+1)} < Q$
Pressure gradient	$-\left(\frac{n+1}{n}\right)^n < P < 0$	$P < -\left(\frac{n+1}{n}\right)^n$

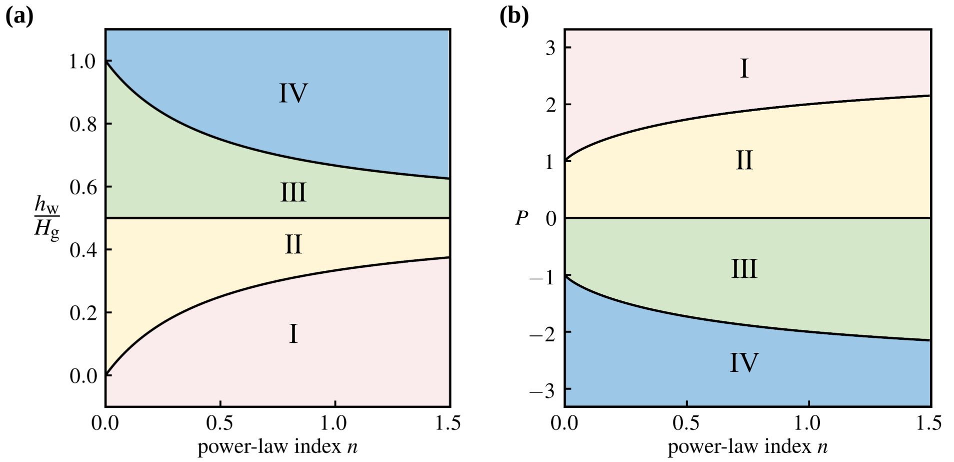

Figure 3.9: (a) Dimensionless flow rate and (b) dimensionless pressure gradient that divides the flow states in the C-P flow of power-law fluids, plotted against the power-law index n.

prescribed flow rate per unit width through the downstream channel (as defined in

Equation (3.20)). Substituting the relation into the Equation (3.20), we obtain

$$Q = \frac{q}{U_{\mathrm{w}} H_{\mathrm{g}}} = \frac{h_{\mathrm{w}}}{H_{\mathrm{g}}}. \tag{3.29}$$

This implies that for slot coating flows, the dimensionless wet thickness coincides with the dimensionless prescribed flow rate. Based on this fact, we use Equation (3.27), the flow reversal condition, to predict the vortex formation conditions computed by 2-D flow model.

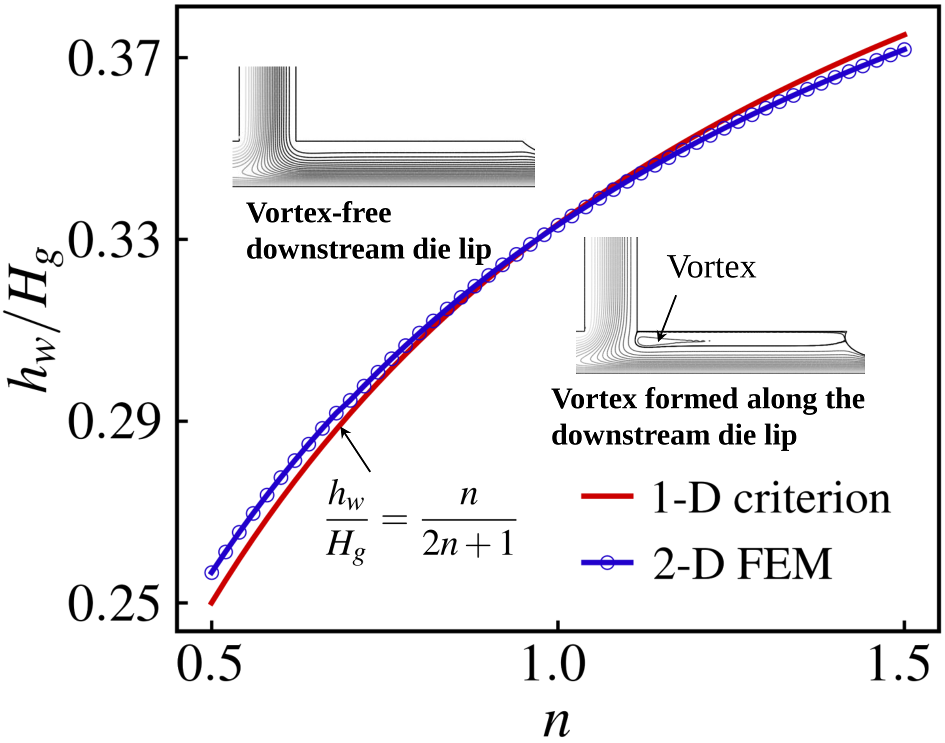

Figure 3.10: Dimensionless flow rate $h_{\mathrm{w}}/H_{\mathrm{g}}$ at the moment of vortex birth (2-D FEM computations) and flow reversal (1-D model prediction) plotted together against the power-law index n.

Figure 3.10 shows the dimensionless flow rate at the onset of flow reversal (Equation (3.27)) derived from the 1-D rectilinear flow model, plotted as a function of n, along with the vortex formation conditions computed using 2-D model (previously presented in Figure 3.6). The two results shows reasonable agreement, with the maximum relative error being less than 4% under the range of n considered in this analysis. This shows that the analytical flow reversal condition derived from the simple rectilinear flow model is fairly accurate at predicting the birth of vortex in the downstream slot coating flow of the power-law fluid.

What is also worth noting is that the dimensionless flow rate at the onset of both conditions decreases as n decreases, which means that the shear-thinning property helps suppress the vortex birth under the downstream slot-die lip. From an engineering point of view, this implies that a wider range of operating conditions can be exploited while preventing downstream vortex formation, by using coating liquids with a higher degree of shear-thinning behavior. In other words, it is possible to coat a thinner film at a fixed coating gap H_{g} or coat at a larger coating gap with a fixed flow rate in a vortex-free environment.

A qualitative explanation regarding this trend can be explored by examining the kinematics along the stationary wall. For a vortex bubble to occur, the flow must detach from the wall, which can be identified by a change in the sign of the shear rate $\partial u_{\mathrm{t}}/\partial s_{\mathrm{n}}$ along the wall. Figure 3.11 illustrates the velocity profile obtained from the 1-D model at different values of n (varied from 0.5 to 1.5) and dimensionless flow rate $h_{\mathrm{w}}/H_{\mathrm{g}}$ (varied from $3/8$ to $1/4$). At a fixed $h_{\mathrm{w}}/H_{\mathrm{g}}$, the flow with the lowest value of n exhibits the most negative shear rate at the upper wall. As the dimensionless flow rate decreases, the magnitude of the adverse pressure gradient across the channel grows, causing the shear rate to increase toward a positive value. At some point, the sign of the shear rate is changed and flow reversal is observed. This point of transition occurs at the lowest dimensionless flow rate for the shear-thinning fluid ($n < 1$) and at the highest for the shear-thickening fluids ($n > 1$). This suggests that the shear-thinning property of the fluid makes it less vulnerable to the adverse pressure gradient generated under the reduced flow rate. Thus, the onset of flow reversal and the birth of vortex on the wall are delayed by this fluid property.

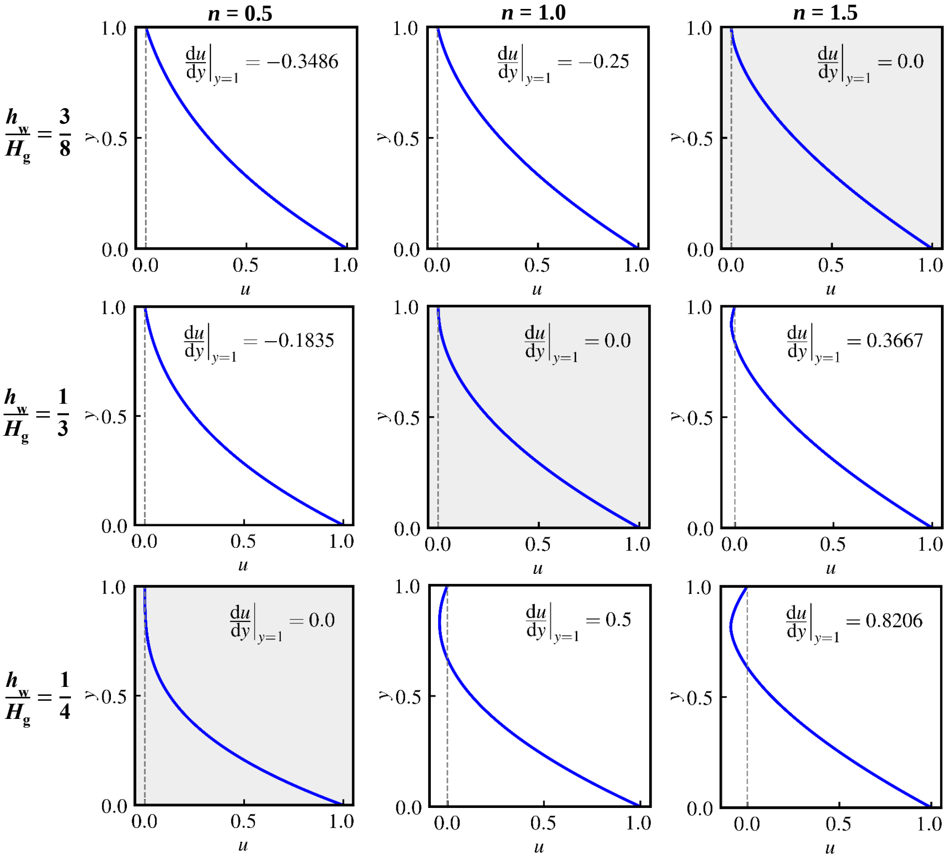

Figure 3.11: Velocity profiles under the downstream die lip, as predicted by the 1-D rectilinear flow model with dimensionless flow rate of $h_{\mathrm{w}}/H_{\mathrm{g}} = 3/8,\ 1/3$, and $1/4$; and power-law index taking values of $n = 0.5$ (shear-thinning), $n = 1.0$ (Newtonian), and $n = 1.5$ (shear-thickening).

3.4 Local power-law approximation method

By rearranging the flow reversal conditions (Equation (3.27)) into their dimensional forms, we obtain following critical conditions in terms of the pressure gradient $p_{\mathrm{x,c}}$ and flow rate per width q_{c} as:

$$p_{\mathrm{x,c}} = \left(\frac{n+1}{n}\right)^n \frac{K(U_{\mathrm{w}}/H_{\mathrm{g}})^n}{H_{\mathrm{g}}}, \tag{3.30}$$

$$q_{\mathrm{c}} = \frac{n}{2n+1} U_{\mathrm{w}} H_{\mathrm{g}}. \tag{3.31}$$

A closer inspection of Equations. (3.30) and (3.31) reveals that the critical conditions for power–law fluids are explicitly expressed in terms of the system parameters (U_{w} and H_{g}) and fluid properties (K and n). Hence, in this section, we propose the *local power–law approximation (LPLA) method*, which approximates a fluid as a power–law fluid locally around a representative shear rate $\dot{\gamma}_{\mathrm{r}}$, as shown in Figure 3.12. With this method, it is possible to extend the results obtained in Section 3.3 for power-law fluids to the more general cases of generalized Newtonian fluids (GNFs), whose viscosities depend on the shear rate arbitrarily.

Cruz *et al.* (2012) adopted the same methodology to estimate the Nusselt number and friction factor of a fully developed laminar flow in circular pipes with a constant wall heat flux. They used the Newtonian wall shear rate as the representative shear rate of the system and reported maximum estimation errors of 6% and 8% for the friction factor and Nusselt number, respectively. In the analysis covered in this section, we applied the method to a different system (parallel channel flow between stationary and moving walls) using a different representative shear rate to estimate the critical flow reversal conditions.

For the flow curve in the log–log scale, a tangent line parameterized by two variables, $\hat{K}$ and $\hat{n}$, can be constructed at $\dot{\gamma}_{\mathrm{r}}$. From the slope of the curve and the viscosity

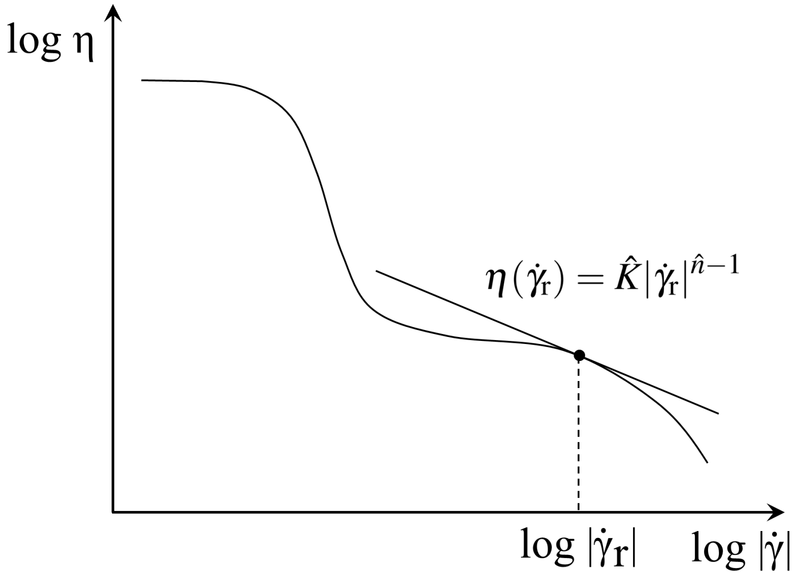

Figure 3.12: Flow curve plotted in log–log scale. Fluid is approximated as power–law fluid, parameterized by $\hat{K}$ and $\hat{n}$, at a representative shear rate $\dot{\gamma}_{\rm r}$.

evaluated at $\dot{\gamma}_{\rm r}$, $\hat{K}$ and $\hat{n}$ are obtained as follows:

$$\hat{K} = \eta(\dot{\gamma}_{\rm r})\dot{\gamma}_{\rm r}^{1-\hat{n}}, \tag{3.32}$$

$$\hat{n} = n_{\rm loc}(\dot{\gamma}_{\rm r}) = \left.\frac{{\rm d}\log\eta}{{\rm d}\log\dot{\gamma}}\right|_{\dot{\gamma}=\dot{\gamma}_{\rm r}} + 1 = \frac{\dot{\gamma}_{\rm r}}{\eta(\dot{\gamma}_{\rm r})}\left.\frac{{\rm d}\eta}{{\rm d}\dot{\gamma}}\right|_{\dot{\gamma}=\dot{\gamma}_{\rm r}} + 1. \tag{3.33}$$

Here, $n_{\rm loc}(\dot{\gamma}) = \frac{{\rm d}\log\eta}{{\rm d}\log\dot{\gamma}} + 1$ is the local power–law index of the viscosity curve, η, obtained by constructing a tangent line at $\dot{\gamma}$. Upon replacing n in Equation (3.31) by $\hat{n}$, the approximate value of the critical flow rate per width $\hat{q}_{\rm c}$ is obtained as follows:

$$\hat{q}_{\rm c} = \frac{\hat{n}}{2\hat{n}+1}U_{\rm w}H_{\rm g}. \tag{3.34}$$

Meanwhile, two approaches can be used to the approximate the critical pressure gradient. In one approach, we first obtain the approximate wall shear rate $\hat{\dot{\gamma}}_{\rm w}$ by replacing n in the expression derived for the wall shear rate of power-law fluid by $\hat{n}$.

$$\hat{\dot{\gamma}}_{\rm w} = \frac{\hat{n}+1}{\hat{n}}\frac{U_{\rm w}}{H_{\rm g}}. \tag{3.35}$$

Also, by the macroscopic force balance on the 1-D C-P flow at the onset of the flow reversal, the wall shear stress, τ_{w}, can be related to the critical pressure gradient, $p_{\mathrm{x,c}}$, as:

$$\frac{\tau_{\mathrm{w}}}{H_{\mathrm{g}}} = \frac{\tau(y)}{y} = \frac{\mathrm{d}\tau}{\mathrm{d}y} = p_{\mathrm{x,c}}. \tag{3.36}$$

By substituting Equation (3.35) into the derived expression, the approximate value for the critical pressure gradient is computed as follows:

$$(\hat{p}_{\mathrm{x,c}})_1 = \frac{\hat{\tau}_{\mathrm{w}}}{H_{\mathrm{g}}} = \frac{\eta(\hat{\dot{\gamma}}_{\mathrm{w}})\hat{\dot{\gamma}}_{\mathrm{w}}}{H_{\mathrm{g}}}. \tag{3.37}$$

In the other approach, we replace K and n in Equation (3.30) by $\hat{K}$ and $\hat{n}$, respectively, to obtain the following expression:

$$(\hat{p}_{\mathrm{x,c}})_2 = \left(\frac{\hat{n}+1}{\hat{n}}\right)^{\hat{n}} \frac{\hat{K}(U_{\mathrm{w}}/H_{\mathrm{g}})^{\hat{n}}}{H_{\mathrm{g}}} = \left(\frac{\hat{n}+1}{\hat{n}}\frac{U_{\mathrm{w}}/H_{\mathrm{g}}}{\dot{\gamma}_{\mathrm{r}}}\right)^{\hat{n}} \frac{\eta(\dot{\gamma}_{\mathrm{r}})\dot{\gamma}_{\mathrm{r}}}{H_{\mathrm{g}}}. \tag{3.38}$$

This approach can be considered as the approximation of the wall shear stress instead of the wall shear rate.

The accuracy of Equations (3.34), (3.37), and (3.38) in predicting the actual critical conditions depend significantly on the choice of $\dot{\gamma}_{\mathrm{r}}$. In this study, we select the apparent shear rate

$$\dot{\gamma}_{\mathrm{a}} = \frac{U_{\mathrm{w}}}{H_{\mathrm{g}}}, \tag{3.39}$$

to represent a specific system. At the onset of the flow reversal, $\dot{\gamma}_{\mathrm{a}}$ coincides with the average of the magnitude of shear rate, and is thus an appropriate representative of the system considered in this study. Note that this is not the case for general plane C–P flows, where the sign of the shear rate may change depending on the operating conditions. Furthermore, $\dot{\gamma}_{\mathrm{a}}$ can be easily computed from the system parameters without any numerical procedure, allowing the method to be fully analytical.

3.4.1 Results and discussion

In the following, we present the approximate values of the critical conditions for flow reversal obtained using the LPLA method. The Carreau–Yasuda (C–Y) and Bingham–Carreau–Yasuda (B–C–Y) models (Kistler & Schweizer, 1997) were selected as viscosity models for the fluids involved in the computations. The constitutive equations are as follows:

$$\text{C–Y: } \eta(\dot{\gamma}) = \eta_\infty + (\eta_0 - \eta_\infty)\left[1 + (\lambda|\dot{\gamma}|)^a\right]^{\frac{n-1}{a}}, \tag{3.40}$$

$$\text{B–C–Y: } \eta(\dot{\gamma}) = \eta_\infty + \left(\eta_0 - \eta_\infty + \tau_Y \frac{1 - e^{-F|\dot{\gamma}|}}{|\dot{\gamma}|}\right)\left[1 + (\lambda|\dot{\gamma}|)^a\right]^{\frac{n-1}{a}}. \tag{3.41}$$

Here, η_∞, η_0, λ, n, a, τ_Y, and F are the model parameters determined by fitting the experimental data. To analyze the accuracy of the LPLA method, we adjusted the values of the parameters such that the resulting flow curves exhibited different values of $\hat{n}$ over the shear rate range of interest. The parameter values are summarized in Table 3.3, and the corresponding flow curves are shown in Figure 3.13.

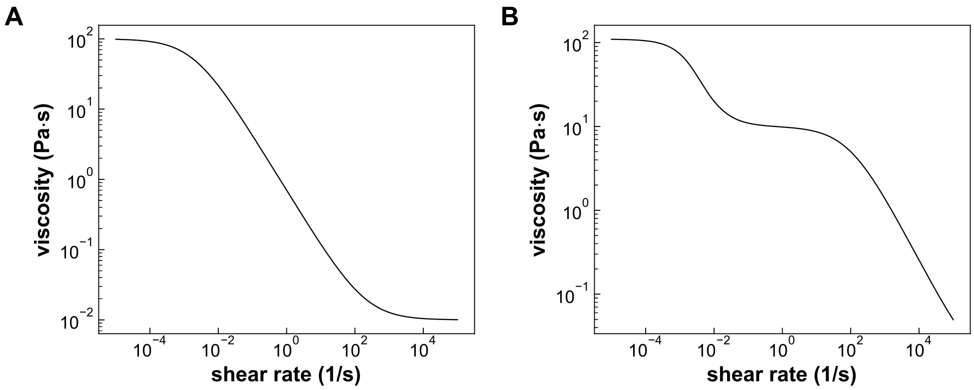

Figure 3.13: Flow curves of A. Carreau–Yasuda (C–Y) fluid and B. Bingham–Carreau–Yasuda (B–C–Y) fluid.

The LPLA method was used to predict the critical flow rate per width, q_c, and critical pressure gradient, $p_\mathrm{x,c}$. The approximate values were computed for the C–P flows of both the C–Y and B–C–Y fluids. In addition, two different approaches were used to approximate $p_\mathrm{x,c}$, either by approximating the wall shear rate ($(\hat{p}_\mathrm{x,c})_1$) or by approximating the wall shear stress ($(\hat{p}_\mathrm{x,c})_2$) as that of the power-law fluid. The

Table 3.3: Values of model parameters.

Model	η_∞ / Pa $\cdot$ s	η_0 / Pa $\cdot$ s	λ / s	n	a	τ_Y / Pa	F / s
C–Y	0.01	100	500	0.2	0.8	-	-
B–C–Y	0.01	10	0.01	0.2	0.8	0.1	1000

different cases of approximation considered in this section and the corresponding figure numbers are summarized in Figure 3.14.

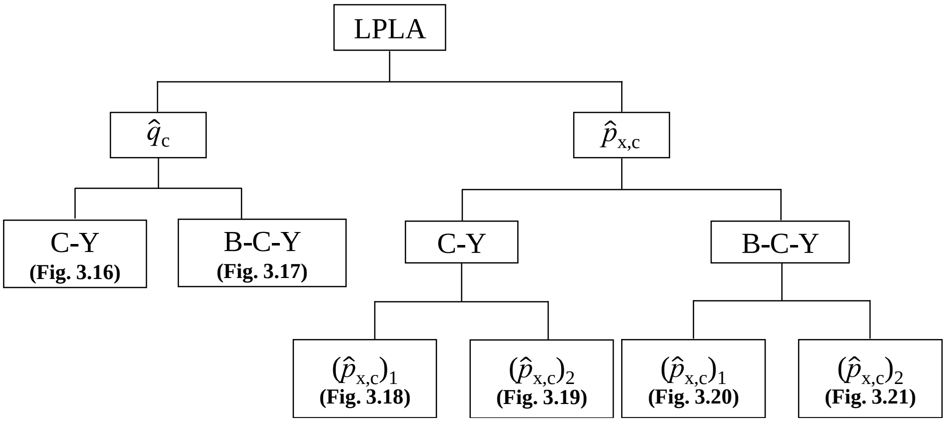

Figure 3.14: Tree diagram showing cases where LPLA method is applied to approximate critical flow reversal conditions. Figure number corresponding to each case is also presented.

U_{w} and H_{g} are two controllable operating parameters of the system presented herein. The critical conditions, in their dimensionless form, remain constant as the two variables are increased or decreased by the same factor. Therefore, the critical conditions were computed under different ratios of the two variables, $U_{\mathrm{w}}/H_{\mathrm{g}}$, ranging from 10^{-5} to $10^{5}\,\mathrm{s}^{-1}$, instead of changing the value of each variable independently.

The normalized velocity profiles of C-Y and B-C-Y at the onset of flow reversal are presented in Figure 3.15. It is clear from the figure that the profile depends strongly on the operating conditions. Note that the velocity profile closely resembles that of the Newtonian fluid when the flow curve (refer to Figure 3.13) around $U_\mathrm{w}/H_\mathrm{g}$ is in the Newtonian plateau region. On the other hand, when it resides in the power-law region, the corresponding velocity profile exhibits typical traits of a shear-thinning power law fluid flow, such as the “flat” profile observable near the stationary wall.

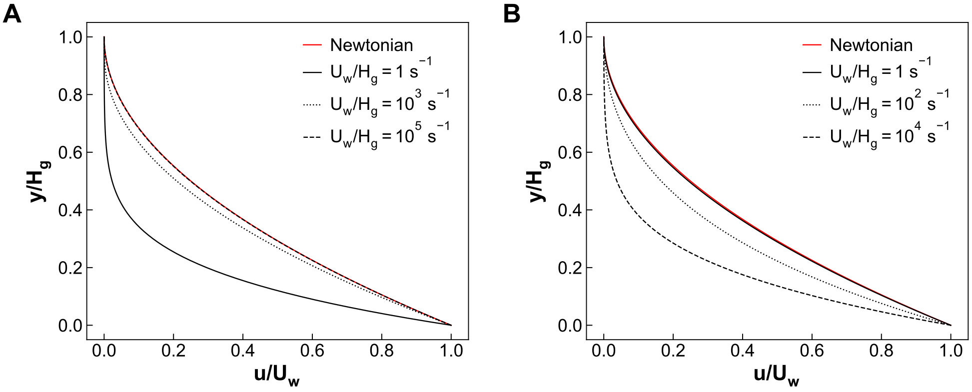

Figure 3.15: Normalized velocity profiles of Couette–Poiseuille (C–P) flow of A. Carreau–Yasuda (C–Y) fluid and B. Bingham–Carreau–Yasuda (B–C–Y) fluid at the onset of flow reversal, under different values of operating conditions. Newtonian counterpart (red solid line) is presented together as a reference.

Lastly, the values predicted by the LPLA method are compared against the exact values computed using the *semi-analytical method*, which will be discussed in detail in Section 3.5. The relative errors are computed using the following formula to evaluate the prediction accuracy of the approximation method:

$$\varepsilon_\mathrm{rel}(\%) = \left| \frac{A_\mathrm{exact} - A_\mathrm{approx}}{A_\mathrm{exact}} \right| \times 100\ (\%), \tag{3.42}$$

where A_exact is the exact value of the critical condition and A_approx is the approximate value predicted by the LPLA method.

Because the LPLA method approximates a given fluid as a power–law fluid locally around $\dot{\gamma}_{\mathrm{r}}$, the error is likely to be small when $\dot{\gamma}_{\mathrm{r}}$ lies in the log–linear region of the flow curve. We define the curvature κ of the log–log flow curve using the following equation and used it to quantify the log–linearity of the curve:

$$\kappa = \frac{\left| \frac{\mathrm{d}^2 \log \eta}{\mathrm{d}\,(\log \dot{\gamma})^2} \right|}{\left\{ 1 + \left(\frac{\mathrm{d} \log \eta}{\mathrm{d} \log \dot{\gamma}} \right)^2 \right\}^{\frac{3}{2}}}. \tag{3.43}$$

Critical flow rate

Figure 3.16A presents the critical flow rate per width q_{c} scaled by $U_{\mathrm{w}} H_{\mathrm{g}}$ computed under varying operating conditions, $U_{\mathrm{w}}/H_{\mathrm{g}}$, for the C–Y fluid. Despite the variation in the error with changing operating conditions, the magnitude of the error, computed using Equation (3.42), remained reasonably low throughout the entire operating condition ($U_{\mathrm{w}}/H_{\mathrm{g}}$) range, with the maximum being 3.98$\%$. What is also noteworthy is that no numerical method was involved when using the LPLA method with $\dot{\gamma}_{\mathrm{r}} = \dot{\gamma}_{\mathrm{a}}$ to obtain the approximate value of the critical flow rate per width $\hat{q}_{\mathrm{c}}$, making it a fully-analytical method. By examining the curvature of the viscosity curve and the relative error depicted in Figure 3.16B, we find that the error trend does not follow that of the curvature. The reason for this will be discussed in detail in Section 3.5.1.

The critical flow rates per width computed for the B–C–Y fluid are shown in Figure 3.17A. Similar to the case of the C–Y fluid, the LPLA methods satisfactorily predicted the critical condition under most of the interesed $U_{\mathrm{w}}/H_{\mathrm{g}}$ ranges. However, large level of relative error (13.49$\%$) was observed when the curvature of the viscosity curve is large around the given operating conditions. The mismatch between the error and curvature trends was also observable in this case (refer to Figure 3.17B).

It is also interesting to notice for both C-Y and B-C-Y cases that the critical dimensionless flow rate approaches one-third when the operating condition corresponds to the Newtonian plateau of the viscosity curve, whereas the flow rate falls

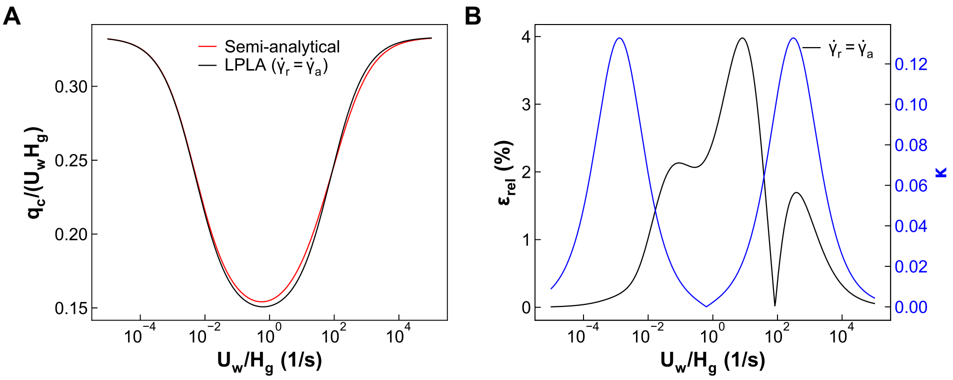

Figure 3.16: A. Dimensionless critical flow rate per width for C–Y fluid predicted using LPLA method (solid black line) along with exact values computed by using semi-analytical method (solid red line), B. Relative error of the LPLA method. Solid blue line represents curvature of corresponding log–log flow curve.

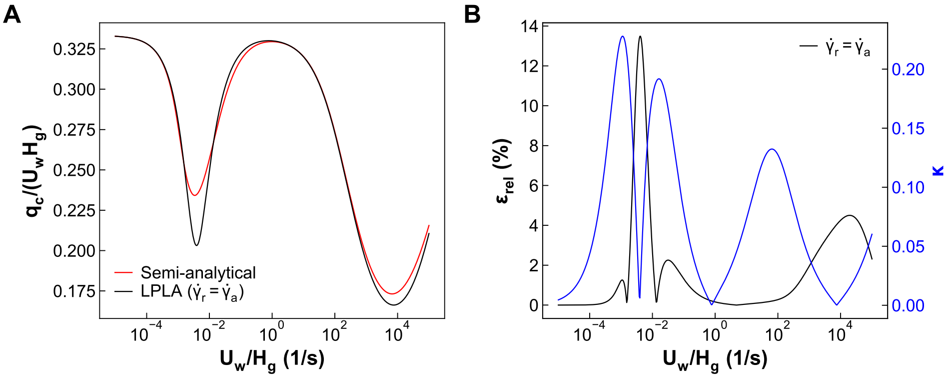

Figure 3.17: A. Dimensionless critical flow rate per width for B-C–Y fluid predicted using LPLA method (solid black line) along with exact values computed by using semi-analytical method (solid red line), B. Relative error of the LPLA method. Solid blue line represents curvature of corresponding log–log flow curve.

below one-third when the operating condition moves on to the power-law (shear-thinning) region of the viscosity curve. This trend agrees with the observation we have made in Section 3.3.2, where it was observed that the flow reversal occurs at a smaller flow rate when the fluid becomes more shear-thinning.

Critical pressure gradient

As described above, the approximate values of the critical pressure gradient, denoted by $(\hat{p}_{\mathrm{x,c}})_1$ and $(\hat{p}_{\mathrm{x,c}})_2$, were obtained using two different approaches for applying the LPLA method. $(\hat{p}_{\mathrm{x,c}})_1$ and $(\hat{p}_{\mathrm{x,c}})_2$ of the C–Y fluid, as well as the exact values obtained using the semi-analytical method, are presented in Figures 3.18A and 3.19A. The pressure gradient was scaled by $\eta(\dot{\gamma}_{\mathrm{a}})\dot{\gamma}_{\mathrm{a}}/H_{\mathrm{g}}$, which is the apparent shear stress divided by the channel height. It is evident from the figures that both approaches of the LPLA method approximate the exact value as accurately as the LPLA method did in predicting q_{c}.

The relative errors of $(\hat{p}_{\mathrm{x,c}})_1$ and $(\hat{p}_{\mathrm{x,c}})_2$ of the C–Y fluid are shown in Figs. 3.18B and 3.19B. The maximum relative error of $(\hat{p}_{\mathrm{x,c}})_1$ in predicting the critical pressure gradient was 6.59%, whereas the corresponding values of $(\hat{p}_{\mathrm{x,c}})_2$ was 4.76%. The error magnitudes were comparable, rendering both LPLA methods feasible for approximating $p_{\mathrm{x,c}}$ of C-Y fluids analytically. Unlike the error of $\hat{q}_{\mathrm{c}}$, those of $(\hat{p}_{\mathrm{x,c}})_1$ and $(\hat{p}_{\mathrm{x,c}})_2$ resembled the curvature variation of the flow curve.

$(\hat{p}_{\mathrm{x,c}})_1$ and $(\hat{p}_{\mathrm{x,c}})_2$ of the B–C–Y fluid, along with their relative errors, are shown in Figures 3.20 and 3.21, respectively. The approximate values were reasonably close to the actual $p_{\mathrm{x,c}}$ under most operating condition ranges, with the exception of $(\hat{p}_{\mathrm{x,c}})_1$ near the operating condition where the viscosity curve exhibited a large curvature. The relative error as high as 14.82% was observed for $(\hat{p}_{\mathrm{x,c}})_1$. That of the $(\hat{p}_{\mathrm{x,c}})_2$ remained relatively low throughout the entire operating condition ranges, with the maximum being 8.00%. The reason behind the high error of $(\hat{p}_{\mathrm{x,c}})_1$ is suspected to be the discrepancy between the wall shear rate $\dot{\gamma}_{\mathrm{w}}$, which is approximated as a power-law fluid, and the viscosity curve η, which belongs to the original GNF. Once again, the error trends of both $(\hat{p}_{\mathrm{x,c}})_1$ and $(\hat{p}_{\mathrm{x,c}})_2$ resembled that of the curvature, unlike that of $\hat{q}_{\mathrm{c}}$.

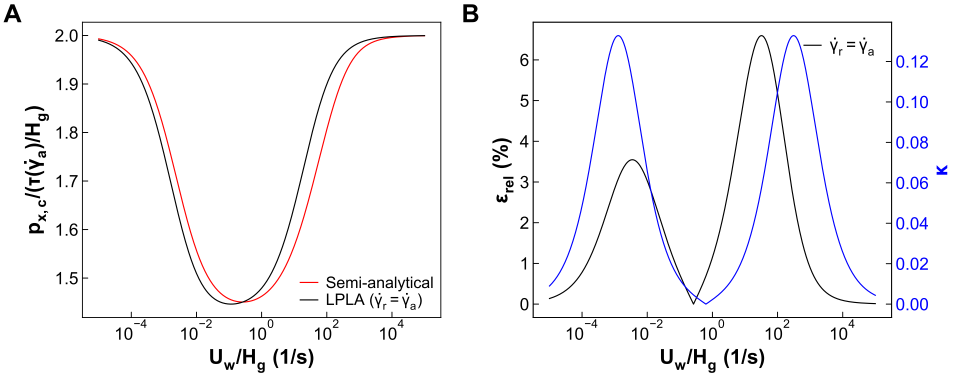

Figure 3.18: A. Dimensionless critical pressure gradient of C–Y fluid and its approximate value, $(\hat{p}_{\mathrm{x,c}})_1$, computed using LPLA method (solid black line) along with exact values computed by using semi-analytical method (solid red line), B. Relative error of the LPLA method. Solid blue line represents curvature of corresponding log–log flow curve.

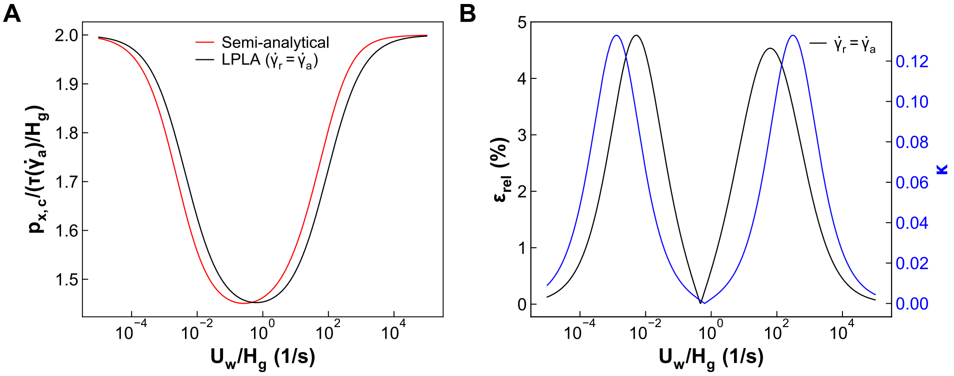

Figure 3.19: A. Dimensionless critical pressure gradient of C–Y fluid and its approximate value, $(\hat{p}_{\mathrm{x,c}})_2$, computed using LPLA method (solid black line) along with exact values computed by using semi-analytical method (solid red line), B. Relative error of the LPLA method. Solid blue line represents curvature of corresponding log–log flow curve.

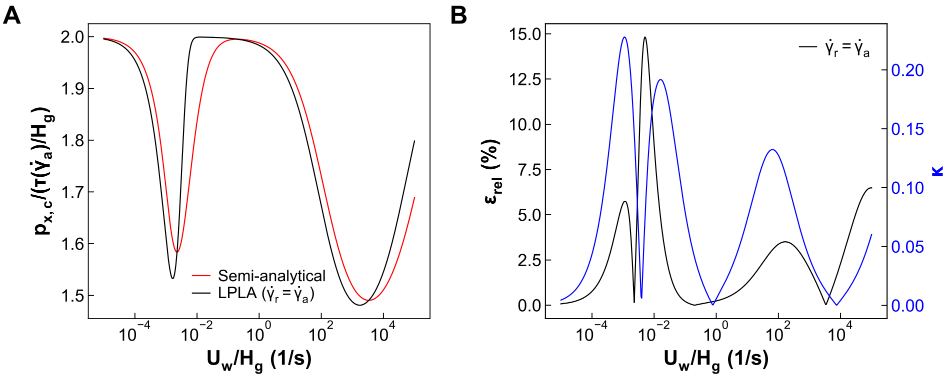

Figure 3.20: A. Dimensionless critical pressure gradient of B-C–Y fluid and its approximate value, $(\hat{p}_{\mathrm{x,c}})_1$, computed using LPLA method (solid black line) along with exact values computed by using semi-analytical method (solid red line), B. Relative error of the LPLA method. Solid blue line represents curvature of corresponding log–log flow curve.

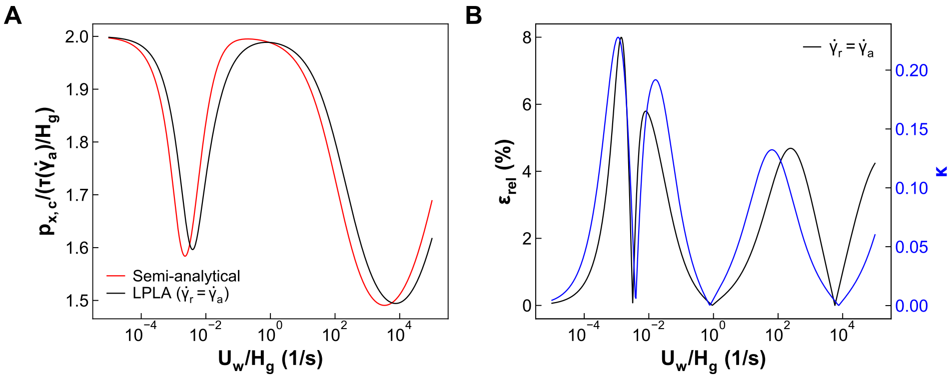

Figure 3.21: A. Dimensionless critical pressure gradient of B-C–Y fluid and its approximate value, $(\hat{p}_{\mathrm{x,c}})_2$, computed using LPLA method (solid black line) along with exact values computed by using semi-analytical method (solid red line), B. Relative error of the LPLA method. Solid blue line represents curvature of corresponding log–log flow curve.

3.5 Semi-analytical method

In this section, we present a systematic procedure for computing the exact values of the critical conditions at the onset of flow reversal, whose approximate values were predicted using the LPLA method in the previous section.

The system of interest is a one-dimensional fully-developed laminar C–P flow of an incompressible generalized Newtonian fluid between two parallel plates, with one moving at velocity U_w and the other stationary at distance H_g from the moving plate. At the onset of flow reversal, the flow is under an additional constraint, i.e., the shear rate is zero on the stationary wall. The detailed flow configuration is shown in Figure 3.22. The configuration is basically the same as that depicted in Figure 3.7, but the direction of increasing y is inverted for the sake of simplicity during the derivation.

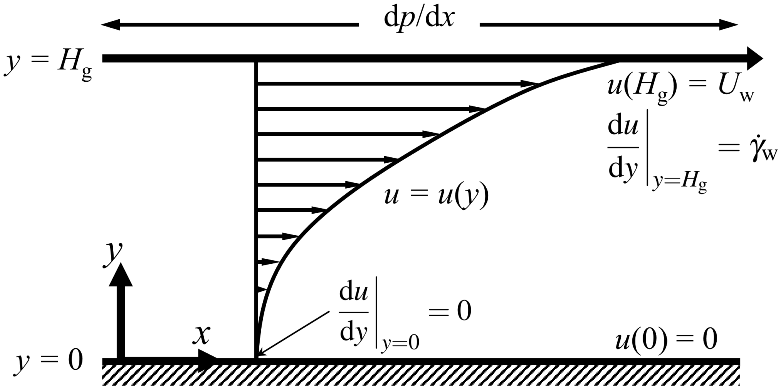

Figure 3.22: Configuration of flow considered in the derivation of semi-analytical method.

When the system parameters (U_w and H_g) and fluid properties are specified, the abovementioned flow state can be fully determined based on a pair of critical flow rate and pressure gradient conditions. We propose a method to obtain the two critical conditions directly using U_w and H_g as well as the flow curve, instead of obtaining the velocity profile as an intermediate, which would otherwise require solving a (non)linear differential equation. This method is named as the *semi-analytical method* because it may or may not require the use of numerical methods depending on the type of constitutive equation involved. However, the only numerical procedures involved in this method are a convergence-guaranteed root-finding algorithm and a numerical integration scheme, which are generally more computationally efficient than solving differential equations.

We referred to the derivation of the Weissenberg–Rabinowitsch equation (Macosko, 1994; Sochi, 2015), which is used extensively in the field of capillary rheometry, to obtain an expression that relates the flow rate to the pressure gradient.

The flow rate per width up to a height of y can be expressed as

$$q(y) = \int_0^y u(y^*)\,\mathrm{d}y^*, \tag{3.44}$$

where u is the velocity in x–direction, and y^* is a dummy variable for integration. Such variables are denoted with asterisks hereinafter.

By integrating Equation (3.44) by parts, changing the integration variable using the relation given in Equation (3.36), and applying the zero shear stress condition on the stationary wall (at $y = 0$), we obtain the following expression for $q(y)$:

$$q(y) = u(y)y - I(y), \tag{3.45}$$

$$I(y) = \left(\frac{H_\mathrm{g}}{\tau_\mathrm{w}}\right)^2 \int_0^{\tau(y)} \dot{\gamma}\tau^*\,\mathrm{d}\tau^*, \tag{3.46}$$

where $\dot{\gamma} = \mathrm{d}u/\mathrm{d}y$ is the shear rate. The expression for the critical flow rate per width q_c can be obtained as:

$$q_\mathrm{c} = U_\mathrm{w}H_\mathrm{g} - I(H_\mathrm{g}), \tag{3.47}$$

by substituting H_g into Equation (3.45).

Because the distance between the walls (H_g) and the wall velocity (U_w) are specified, the only unknowns are the wall shear stress τ_w and critical flow rate q_c. The additional equation to render the problem fully determined is the no-slip condition at the stationary wall, which is the only unused condition thus far.

For the additional equation, we use the integral equation for the velocity,

$$u(y) - u(0) = \int_0^{u(y)} \mathrm{d}u^*. \tag{3.48}$$

By the change of variable and applying zero shear rate condition on the stationary wall (at $y = 0$), we obtain the following expression for $u(y)$.

$$u(y) - u(0) = I_2(y), \tag{3.49}$$

$$I_2(y) = \frac{H_\mathrm{g}}{\tau_\mathrm{w}} \int_0^{\tau(y)} \dot{\gamma} \mathrm{d}\tau^*. \tag{3.50}$$

By substituting H_g into Equation (3.49) and applying the unused no-slip condition, $u(0) = 0$, we obtain the second equation to make the problem fully determined as follows:

$$U_\mathrm{w} = I_2(H_\mathrm{g}). \tag{3.51}$$

By solving Equations (3.47) and (3.51), one can obtain the exact value of the wall shear stress τ_w (which is directly related to the critical pressure gradient $p_\mathrm{x,c}$ by Equation (3.36)) and the critical flow rate per width q_c at the onset of flow reversal. The detailed procedure is as follows:

1. Using the wall velocity U_w, channel height H_g, and flow curve ($\eta = \eta(\dot{\gamma})$), Equation (3.51) is solved for the wall shear rate $\dot{\gamma}_\mathrm{w}$. Numerical methods are used for integration and root-finding, where necessary.

2. The wall shear stress is calculated from $\tau_\mathrm{w} = \eta(\dot{\gamma}_\mathrm{w})\dot{\gamma}_\mathrm{w}$ and substituted into Equations (3.36) and (3.47) to obtain the critical pressure gradient $p_\mathrm{x,c}$ and the flow rate per width q_c.

When computing the exact values presented in Section 3.4.1, we used the `QAGS` routine of the `QUADPACK` library for numerical integration, as well as the bisection method with increasing interval for root-finding.

3.5.1 Source of error in local power-law approximation method revisited

In Section 3.4.1, we have observed the discrepancy between the error and the curvature of the viscosity curve when LPLA method is applied to predict the critical flow rate, q_{c}. An equation derived for the semi-analytical method provides possible reasons behind this observation.

By nondimensionalizing Equation (3.47), we can obtain an expression for the dimensionless critical flow rate as follows:

$$\frac{q_{\mathrm{c}}}{U_{\mathrm{w}} H_{\mathrm{g}}} = 1 - \left(\frac{1}{\dot{\gamma}_{\mathrm{a}}}\right) \int_0^{\dot{\gamma}_{\mathrm{w}}} \left\{\frac{\tau(\dot{\gamma}^*)}{\tau_{\mathrm{w}}}\right\}^2 n_{\mathrm{loc}}(\dot{\gamma}^*)\, \mathrm{d}\dot{\gamma}^*. \tag{3.52}$$

Here, n_{loc} is the local power–law index as defined in Equation (3.33). Because the integrand, $(\tau/\tau_{\mathrm{w}})^2 n_{\mathrm{loc}}$, is a continuous function of $\dot{\gamma}$, according to the mean value theorem, $0 < \dot{\gamma}_{\mathrm{m}} < \dot{\gamma}_{\mathrm{w}}$ exists such that the following relation holds:

$$\frac{q_{\mathrm{c}}}{U_{\mathrm{w}} H_{\mathrm{g}}} = 1 - \left(\frac{\dot{\gamma}_{\mathrm{w}}}{\dot{\gamma}_{\mathrm{a}}}\right) \left\{\frac{\tau(\dot{\gamma}_{\mathrm{m}})}{\tau_{\mathrm{w}}}\right\}^2 n_{\mathrm{loc}}(\dot{\gamma}_{\mathrm{m}}) = 1 - \left(\frac{\dot{\gamma}_{\mathrm{w}}}{\dot{\gamma}_{\mathrm{a}}}\right) \left(\frac{\tau_{\mathrm{m}}}{\tau_{\mathrm{w}}}\right)^2 n_{\mathrm{loc,m}}. \tag{3.53}$$

For power–law fluids, analytical expressions can be obtained for each term in Equation (3.53) in terms of the power–law index n.

$$\frac{\dot{\gamma}_{\mathrm{w}}}{\dot{\gamma}_{\mathrm{a}}} = \frac{n+1}{n}, \tag{3.54}$$

$$\frac{\tau_{\mathrm{m}}}{\tau_{\mathrm{w}}} = \sqrt{\frac{1}{2n+1}}, \tag{3.55}$$

$$n_{\mathrm{loc,m}} = n. \tag{3.56}$$

Applying the LPLA method to obtain the approximate value of the critical flow rate per width, $\hat{q}_{\mathrm{c}}$, is equivalent to replacing n in the equations above with $\hat{n}$, as defined in Equation (3.33). This can be verified by substituting Equations (3.54) through (3.56), where n is replaced by $\hat{n}$, into Equation (3.53) and comparing the resulting expression with Equation (3.34).

The errors generated in the approximation of each term add up to the final error of $\hat{q}_{\mathrm{c}}$ in approximating q_{c}. Therefore, their contribution to the final error can be analyzed by comparing the exact and approximate values term by term.

Figure 3.23 presents the ratios of the approximate to exact values of $\dot{\gamma}_{\mathrm{w}}/\dot{\gamma}_{\mathrm{a}}$, $\tau_{\mathrm{m}}/\tau_{\mathrm{w}}$, and $n_{\mathrm{loc,m}}$ for the C–Y fluid. A ratio larger than unity indicates an overestimation of the approximate values, whereas a ratio less than unity corresponds to underestimation. The semi-analytical method was used to obtain the exact value of $\dot{\gamma}_{\mathrm{w}}/\dot{\gamma}_{\mathrm{a}}$, whereas those of the remaining terms were evaluated numerically using the secant method. The approximate values were obtained by replacing n in Equations (3.54) through (3.56) with the local power–law index, $\hat{n}$, evaluated at $\dot{\gamma}_{\mathrm{r}} = \dot{\gamma}_{\mathrm{a}}$. The approximate values of $\tau_{\mathrm{m}}/\tau_{\mathrm{w}}$ indicated the least deviation from the exact values, with ratios ranging from 0.980 to 1.028. The deviation of the approximate values of the remaining terms was relatively large, with the ratio of $\dot{\gamma}_{\mathrm{w}}/\dot{\gamma}_{\mathrm{a}}$ ranging from 0.891 to 1.145 and that of $n_{\mathrm{loc,m}}$ ranging from 0.839 to 1.154. However, their deviations were opposite; when the ratio of $\dot{\gamma}_{\mathrm{w}}/\dot{\gamma}_{\mathrm{a}}$ was larger than unity (overestimation), the ratio of $n_{\mathrm{loc,m}}$ tended to be smaller than unity (underestimation), and vice versa. Because each term was multiplied together to obtain the final $\hat{q}_{\mathrm{c}}$, as shown in Equation (3.53), individual errors were canceled and a low overall estimation error was obtained, as depicted in Figure 3.16. Moreover, it was observed that the estimation error was small (ratios tend to unity) near the operating conditions where the flow curve was highly log–linear (see Figure 3.16B). However, the exact value of the operating condition, $U_{\mathrm{w}}/H_{\mathrm{g}}$, at which the ratio equals unity, differed for each term. This may have contributed to the deviation of the relative error of the LPLA method with $\dot{\gamma}_{\mathrm{r}} = \dot{\gamma}_{\mathrm{a}}$ from the curvature trend, as observed from Figure 3.16.

The ratios for the B–C–Y fluid are shown in Fig. 3.24 and a similar trend to that of the C–Y fluid case was observed. The ratio of the approximate to exact value of $\tau_{\mathrm{m}}/\tau_{\mathrm{w}}$ remained close to unity, whereas those of the other terms deviated significantly

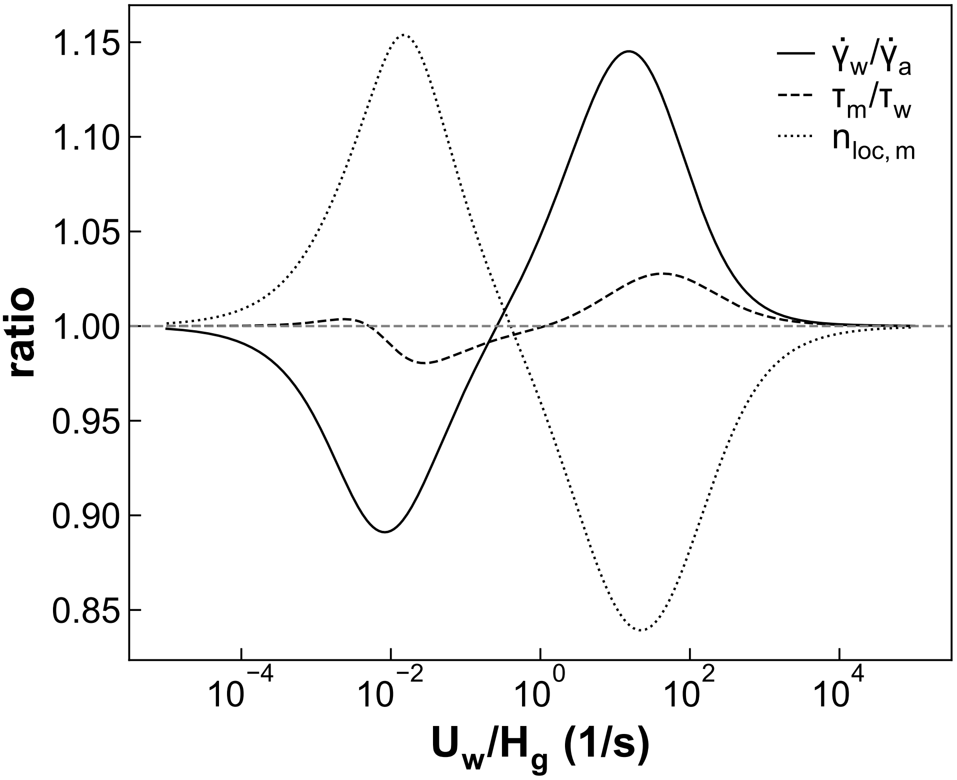

Figure 3.23: (C–Y fluid) Ratio of approximate to exact value of terms constituting $q_c/(U_w H_g)$: solid line, $\dot{\gamma}_w/\dot{\gamma}_a$; dashed line, τ_m/τ_w; dotted line, $n_{loc,m}$.

at the operating conditions where the flow curve exhibited a large curvature. The deviation from unity was relatively larger than that observed in the C–Y fluid case, thereby resulting in the larger relative error of the LPLA method in approximating q_c for the B–C–Y fluid when compared with the C–Y fluid.

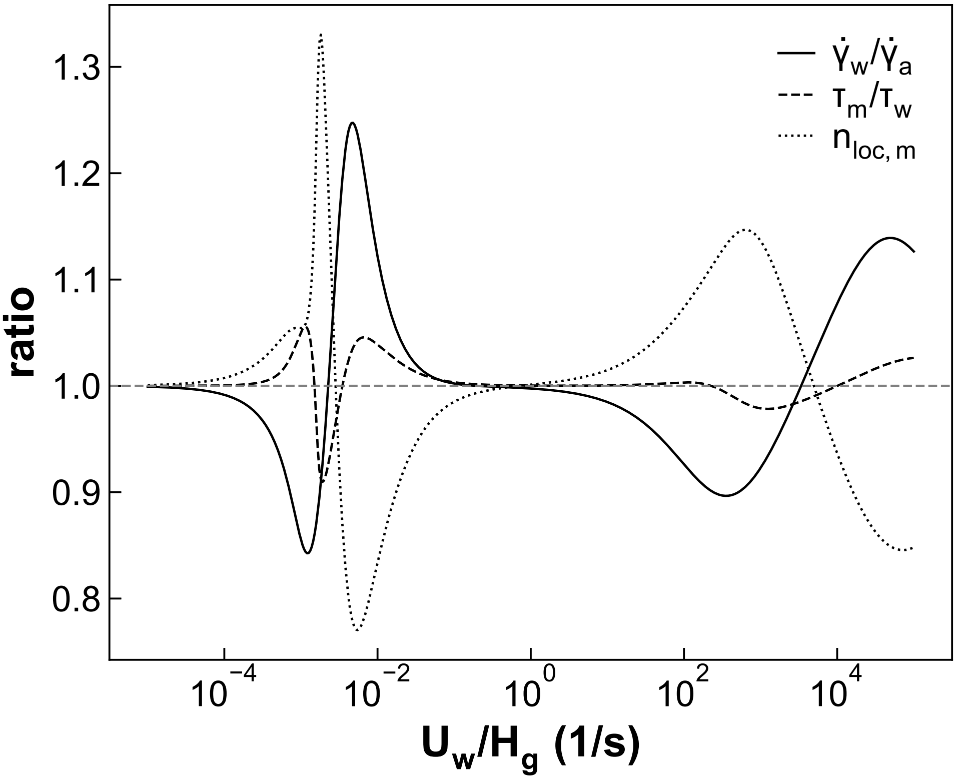

Figure 3.24: (B–C–Y fluid) Ratio of approximate to exact value of terms constituting $q_c/(U_w H_g)$: solid line, $\dot{\gamma}_w/\dot{\gamma}_a$; dashed line, τ_m/τ_w; dotted line, $n_{loc,m}$.

3.6 Conclusions

In this chapter, the problem of obtaining vortex formation conditions in the slot coating flows was solved by using different types of computational and analytical models. The previously unknown behaviors of fluids with shear rate dependent viscosities were explored by using two-dimensional (2-D) computational flow model, together with an automated algorithm for finding the vortex formation conditions. The power-law fluids were the first to be examined, and analytical criteria for vortex birth in the downstream region could be developed through the use of an analytical one-dimensional (1-D) flow model. By using the 1-D model, it was possible to change the original problem of finding the vortex formation condition to a simpler problem of finding the onset condition for the flow reversal in a 1-D Couette-Poiseuille flow. The derived expressions for the power-law fluid were extended to the generalized Newtonian fluids (GNFs) by using the local power-law approximation (LPLA) method. The LPLA method requires no numerical evaluation, thereby providing a quick and fairly accurate prediction of the vortex formation conditions for the given GNF, just as the one-third rule does for the Newtonian fluids. Also, a systematical procedure for obtaining the exact values for the GNFs was presented as well, and the results were used to evaluate the accuracy of the LPLA method.

The results of the analysis show that there exists a significant difference between the flow reversal condition for different types of fluids. The critical flow rate condition for the Newtonian fluids, in its dimensionless form, is a constant regardless of the fluid viscosity and the operating conditions. The same condition for the power-law fluids, however, is a function of power-law index n, which is the material property. Lastly, for GNFs, the dimensionless critical condition is a function of both fluid properties and the operating conditions (e.g. H_{g} and U_{w}). This implies that as the viscosity of the coating fluid exhibits more "complex" behavior, there is a wider choice available for maintaining a vortex-free flow during the process operation.

Chapter 4

Physics-informed machine learning of slot coating flows

4.1 Introduction

With the advancement in the measurement technology, computing powers, and data storage capabilities, the accessability and availability of big data have never been greater. Many industries have been utilizing the big data acquired from the production line for fault detection, quality control, and process optimization (Yin & Kaynak, 2015; Wamba *et al.*, 2015).

Slot coating process is not an exception, and different sources of data exists in the slot coating flow. For example, position of contact lines relative to that of the feed slot can be detected and obtained under varying operating conditions by visualizing the coating bead flow from under a transparent substrate (Hong & Nam, 2017). A side-view visualization of the coating bead flow is also possible through the experimental setup described by Yoon *et al.* (2022), from which the shape and position of the meniscus can be obtained. Pressure transducers can also be mounted to the slot-die, such that the data on the pressure drop can be readily collected (Schmitt *et al.*, 2015). It is also possible to obtain the topology of the wet film through the use of a laser displacement sensor (Schmitt *et al.*, 2014). It provides valuable information on the thickness variation along the film width, making it possible to quantify the widthwise uniformity of the film. Furthermore, simple imaging of the coated film can also provide data on different types of film defects that occur when the operating conditions are not optimized (Schoo *et al.*, 2023).

In contrast to the data described above, which are physically observed or measured, coating flow data can also be collected virtually through the use of high fidelity computational models. Slot coating flows have been modeled by using the finite element method (Gates, 1999) or the finite volume method (Ji *et al.*, 2016) to accurately predict the velocity and pressure fields and the meniscus shapes of the flow. Provided that all the necessary physics for describing the flow accurately are taken into account, computational models are capable of producing large amount of useful coating flow data that are difficult to obtain experimentally (such as the velocity field), at a considerably lower cost.

In this context, the governing equations and boundary conditions used in modeling the slot coating flow can also be treated as, in a broad sense, data, since they provide the information on the physics that governs the flow. For example, as described in Section 2.2, Landau-Levich film coating theory is applied at the downstream meniscus of the slot coating flow to model the pressure jump. Also, the Navier-slip boundary condition is typically applied to the dynamic contact line of the upstream meniscus such that a physical solution can be obtained (Gates, 1999).

However, in many occasions these data may not exist in their complete form. Due to the lack of time and resources, limitation of measurement technologies, and existence of unknown physics, the data may be available only partially. In this chapter, a new machine learning based approach, named *physics-informed machine learning*, is applied to the modeling of slot coating flow for the first time to solve to solve flow problems when the given data is missing in parts. The method uses a network named *physics-informed neural network* (PINN) to accurately predict the domain and flow field of the slot coating flow. As the name suggests, during the training process, the network not only incorporates the field variable data, but also the knowledge of the governing equations. Since its first appearance in Raissi *et al.* (2019) for solving different kinds of nonlinear partial differential equations (PDEs), PINNs have been applied to solve problems in numerous scientific and engineering fields, such as fluid dynamics (Jin *et al.*, 2021), heat transfer (Cai *et al.*, 2021), solid mechanics (Haghighat *et al.*, 2021), and electrophysiology (Sahli Costabal *et al.*, 2020), to name a few.

In the sections that follow, we first compare the physics-informed machine learning with conventional machine learning techniques to show how it differs from solving regression problems. Next, the network architecture used in this study, which is specialized for modeling free surface flows, is presented. After a brief overview on how the loss functions are constructed, the method for choosing the right weights for the terms constituting the loss function is presented. Finally, two illustrative problems are solved using the proposed method to demonstrate its flexibility in dealing with problems with partly missing data.

4.2 Comparison with regression problems

Figure 4.1 depicts a conventional machine learning approach of solving a regression problem, using a neural network (NN) to model the function under interest. The parameters of the NN are tuned through an optimization process called the *training*. The goal of the training is to find the optimal parameters which, if they exist, will result in the NN model that best “explains” the given data.

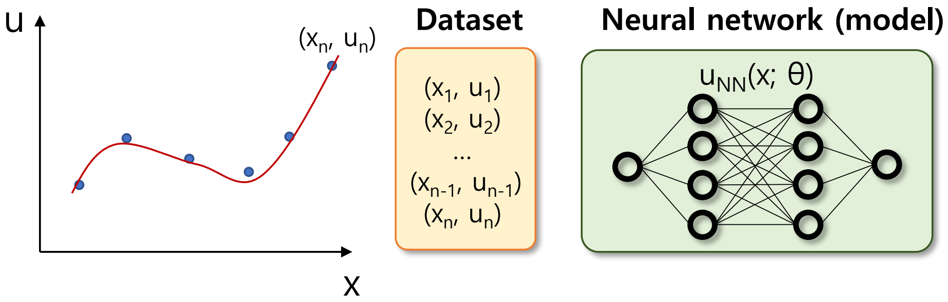

Figure 4.1: Schematic diagram of solving a regression problem using a neural network.

The training is driven by minimizing the following loss function:

$$\mathcal{L}(\boldsymbol{\theta}) = \frac{1}{N}\sum_{i=1}^{N} |u_i - u_{\mathrm{NN}}(x_i; \boldsymbol{\theta})|^2. \tag{4.1}$$

Here, $\{(x_i, u_i)\}$ are the given N data points, and u_{NN} and $\boldsymbol{\theta}$ are the output of NN and the parameters of NN, respectively. As can be seen from the loss function, the training is solely guided by the given data points. The trained NN, despite its ability to “mimic” the trend of the data, is ignorant of the physics that governs the data.

Physics-informed machine learning and physics-informed neural networks (PINN) can be thought as a method which embeds the physics behind the provided data into the network itself during the training process. Figure 4.2 shows the physics-informed machine learning approach for solving an engineering problem expressed in terms of a differential equation, $\mathcal{F}(u, u', u'', x) = 0$. The data are now given only at the boundary or initial points, and the intermediate values are determined such that the NN satisfies the given governing equation.

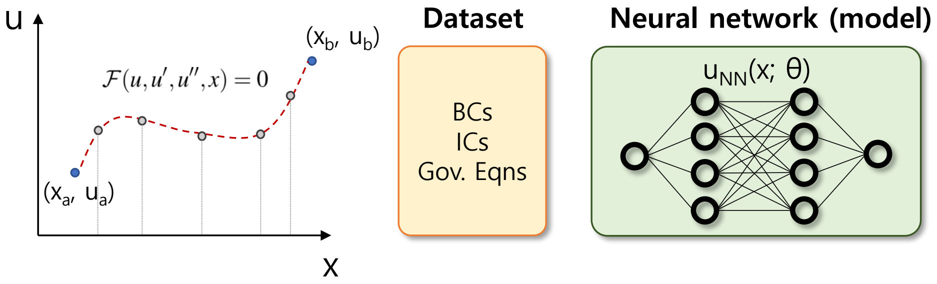

Figure 4.2: Schematic diagram of solving a differential equation using physics-informed machine learning technique.

The loss function is expressed as:

$$\begin{aligned}\mathcal{L}(\boldsymbol{\theta}) &= \mathrm{MSE}_u + \mathrm{MSE}_f \\ &= \frac{1}{N_u}\sum_{i=1}^{N_u}|u_i - u_{\mathrm{NN}}(x_i^u, t_i^u; \boldsymbol{\theta})|^2 + \frac{1}{N_f}\sum_{i=1}^{N_f}|\mathcal{F}[u_{\mathrm{NN}}(x_i^f, t_i^f; \boldsymbol{\theta})]|^2. \qquad (4.2)\end{aligned}$$

Here, $\{(x_i^u, t_i^u, u_i)\}$ are the N_u points specifying boundary or initial conditions and $\{(x_i^f, t_i^f)\}$ are the N_f sampling points within the domain of interest where the governing equation residuals are evaluated. The difference with the loss function of the regression problem case, Equation (4.1), is the regularization term, MSE_f. This term serves as a guide for the NN to follow the governing equations of the given system. Thus through a successful optimization, it is possible to embed the knowledge of the physics of the given system into the NN.

By examining Equation (4.2), we find that in order to evaluate the value of $\mathcal{F}[u_{\mathrm{NN}}(x_i^f, t_i^f; \boldsymbol{\theta})]$, one need to compute the derivative of the NN output u_{NN} with respect to the NN input x or t. This can be done with ease by using the `autograd` functionality of the existing libraries for machine learning such as $TensorFlow$ or $PyTorch$.

4.3 Network architecture

In this section, we discuss the network architecture adopted in this chapter to model the slot coating flow. As discussed in previous sections and depicted in several figures, the slot coating flow is bounded by two liquid-gas interfaces in the upstream and downstream regions, respectively (refer to Sections 1.1, 2.1, and 3.2.1 and Figures 1.3, 2.1, and 3.3).

In terms of process operation, these menisci may pose a threat to stable operation if they become unstable and undermine the widthwise uniformity of the film, when the operating parameters are not carefully chosen. Computationally, the existence of menisci cause difficulty when modeling the flow because the flow domain and its boundary are not determined *a priori*.

To handle this difficulty we use two separate NNs to model the coating flow. The first NN, named `net_xy` is responsible for mapping a known reference domain (ξ, η) to the unknown physical domain (x, y). The other NN, named `net_uvp`, maps the physical domain (x, y) to the field variables (u, v, p) of the flow. The points in the reference domain can be thought as a label for each points in the actual flow domain. When successfully trained, it is possible to determine the shape and position of the liquid-gas interfaces by calling `net_xy` on the corresponding reference domain points. The schematic diagram of the two NNs is shown in Figure 4.3.

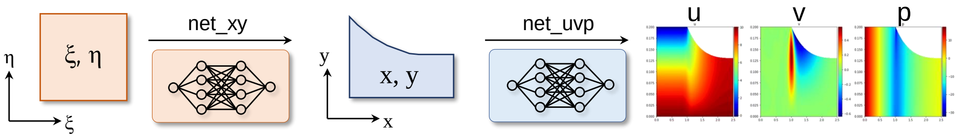

Figure 4.3: Schematic diagram of two separate neural networks for modeling the flows with liquid-gas interfaces.

The mapping from the reference to physical domain for the entire slot coating flow is not trivial due to the existence of several sharp corners. To make it more tractable for the NNs to learn the mapping, we decompose the given domain into several subdomains as shown in Figure 4.4. According to Jagtap & Karniadakis (2021), it is possible to assign NNs to each domain separately, with each NN responsible for modeling the system restricted to each subdomain only. We adopt the same methodology, but with two NNs, `net_xy` and `net_uvp`, responsible for modeling each subdomain. The connectivity between the subdomains is taken care of by adding terms responsible for the continuity of field variables and the governing equation residuals into the loss function. This will be discuss in more detail in Section 4.4.

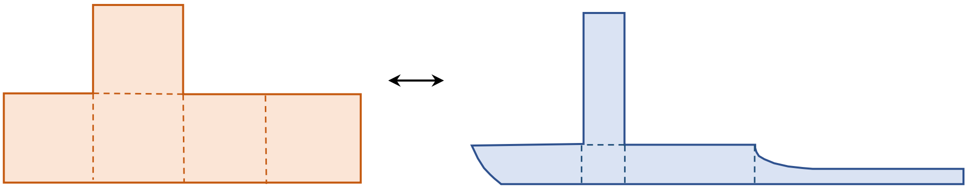

Figure 4.4: Domain decomposition applied to the reference domain (shaded in orange) and the physical domain (shaded in blue).

Different types of neural networks can be used in physics-informed machine learning, depending on the nature of the problem and the system of interest. For example, various types of existing NNs such as the feedforward neural networks (FNNs), convolutional neural networks (CNNs), autoencoders, recurrent neural networks (RNNs), and generative adversarial networks (GANs) have been employed in PINN-related research (Cuomo *et al.*, 2022).

In this chapter, we use one of the simplest NNs, the feedforward NNs, to model the given system, because the purpose of the analysis is to demonstrate the possibility of applying machine learning framework to the problem solving associated with slot coating flows. We leave the study of the best choice of NN design for slot coating flows to future work.

Each networks were designed to have two hidden layers with 64 and 128 nodes each depending on the type of problem solved. Note that these hyperparameters were chosen from a limited number of case studies, and thus are also subject to an extended study for finding optimal values. Swish function $f(x) = x\,\mathrm{sigmoid}(\beta x) = x/(1 + \exp(-\beta x))$, as shown in Figure 4.5, is used as the activation function instead of the ReLU function which is widely used in machine learning frameworks. This choice guarantees the regularity of the NN output, u_{NN}, which is an important characteristic in the physics-informed machine learning as the derivatives of u_{NN} are required for the evaluation of the governing equation (most likely PDE) residuals.

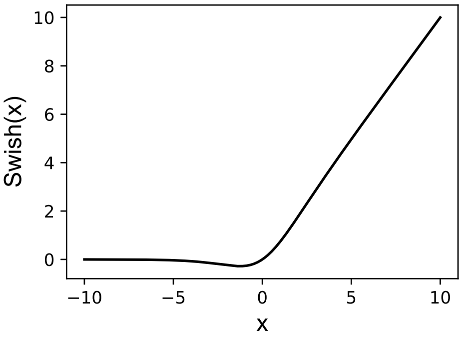

Figure 4.5: Swish activation function (with $\beta = 1$).

4.4 Loss function

To determine the values of the parameters that parameterize the NNs proposed in the previous section, a loss function is required to serve as a guide during the optimization process. As can be seen from Equation (4.2), the terms consistuting the PINN loss function can be categorized into two main groups: those associated with the boundary and initial conditions, and those derived from the governing equations.

To take care a more general case of solving a slot coating flow problem, we modify Equation (4.2) as follows:

$$\begin{aligned}\mathcal{L}(\boldsymbol{\theta}) &= \mathrm{MSE}_b + \mathrm{MSE}_f \\ &= \sum_i^{M^b} \frac{w_i^b}{N_i^b} \sum_j^{N_i^b} \left| \mathcal{B}_i \left[u_{\mathrm{NN}}(\boldsymbol{\xi}_j^b; \boldsymbol{\theta}), \boldsymbol{\lambda} \right] \right|^2 + \sum_i^{M^f} \frac{w_i^f}{N_i^f} \sum_j^{N_i^f} \left| \mathcal{F}_i \left[u_{\mathrm{NN}}(\boldsymbol{\xi}_j^f; \boldsymbol{\theta}), \boldsymbol{\lambda} \right] \right|^2 .\end{aligned} \tag{4.3}$$

Here, $\mathcal{B}_i$ and $\mathcal{F}_i$ represent the individual boundary (or initial) condition and governing equation terms, and superscripts b and f denote the terms related to boundary (or initial) and governing equation terms, respectively. M and N are the number of separate terms and sampled points, respectively, and $\boldsymbol{\lambda}$ denotes the system parameters.

The governing equations of the slot coating flow are listed in Equations (3.2), (3.3), and (3.4). The fluid under consideration in this chapter is a Newtonian fluid, and therefore $\eta(|\dot{\gamma}|)$ in Equation (3.4) is simply a constant. Following equations, which resemble mesh generation equations (Equations (3.5)), are added to the loss function as governing equation residual terms to guarantee a smooth mapping from the reference domain to the physical domain.

$$\nabla^2 \xi = 0, \quad \nabla^2 \eta = 0. \tag{4.4}$$

The same boundary conditions as illustrated in Figure 3.3(b) are used to evaluate the values of $\mathcal{B}_i$ in Equation (4.3).

For the domain decomposition technique to work, boundary conditions defined on the subdomain boundaries have to be included in the total loss function as well. Following terms were evaluated at the points sampled on subdomain boundaries that connect two subdomains and added to the loss function to ensure the connectivity between the two subdomains, (k) and $(k+1)$.

$$\sum_{i}^{M} \frac{w_i}{N_i} \sum_{j}^{N_i} \left| \mathcal{F}_i \left[u_{\mathrm{NN}}^{(k+1)}(\boldsymbol{\xi}_j; \boldsymbol{\theta}^{(k+1)}), \boldsymbol{\lambda} \right] - \mathcal{F}_i \left[u_{\mathrm{NN}}^{(k)}(\boldsymbol{\xi}_j; \boldsymbol{\theta}^{(k)}), \boldsymbol{\lambda} \right] \right|^2, \tag{4.5}$$

$$\frac{w_k}{N_k} \sum_{j}^{N_k} \left| u_{\mathrm{NN}}^{(k+1)}(\boldsymbol{\xi}_j; \boldsymbol{\theta}^{(k+1)}) - u_{\mathrm{NN}}^{(k)}(\boldsymbol{\xi}_j; \boldsymbol{\theta}^{(k)}) \right|^2. \tag{4.6}$$

Equation (4.5) evaluates the governing equation loss terms at the same points on the boundary of the neighboring subdomains and ensures the two values to equal each other. The continuity of the field variables are guaranteed by Equation (4.6), which computes the mean squared errors of the difference between the field variable values.

Additional terms to ensure the prescribed flow rate are also added to the total loss function. Several cross sections are first sampled in the reference domain, (ξ, η), which are mapped to the cross sections in the actual flow domain, (x, y), via `net_xy`, as shown in Figure 4.6. Following residual is evaluated along the cross section in the flow domain, and their mean squared error terms are added to the loss function.

$$\mathcal{B}[u_{\mathrm{NN}}] = q - \int u_{\mathrm{NN}} \cdot n \, \mathrm{d}s \tag{4.7}$$

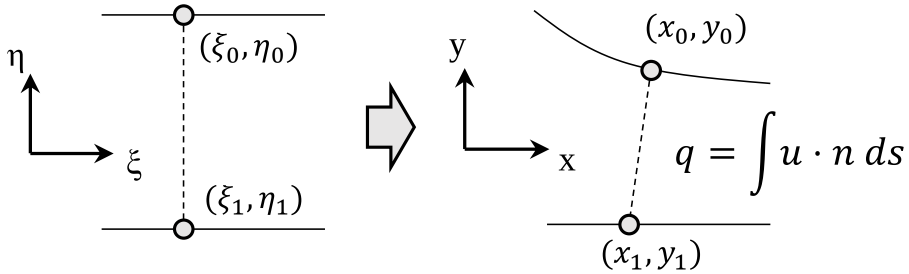

Figure 4.6: Application of flow rate conditions.

The loss function described in Equation (4.3) is for solving problems of the first type as defined in Section 1.2, when all the values consisting $\boldsymbol{\lambda}$ are known. To establish a loss function for the problems of the second type, only a small modification is required.

The modified loss function can be expressed as follows:

$$\begin{aligned}\mathcal{L}(\boldsymbol{\theta}, \boldsymbol{\lambda}) =& \mathrm{MSE}_b + \mathrm{MSE}_f + \mathrm{MSE}_{\mathrm{data}} \\ =& \sum_i^{M^b} \frac{w_i^b}{N_i^b} \sum_j^{N_i^b} \left| \mathcal{B}_i \left[u_{\mathrm{NN}}(\boldsymbol{\xi}_j^b; \boldsymbol{\theta}), \boldsymbol{\lambda} \right] \right|^2 + \sum_i^{M^f} \frac{w_i^f}{N_i^f} \sum_j^{N_i^f} \left| \mathcal{F}_i \left[u_{\mathrm{NN}}(\boldsymbol{\xi}_j^f; \boldsymbol{\theta}), \boldsymbol{\lambda} \right] \right|^2 \\ &+ \frac{w^d}{N^d} \sum_j^{N^d} \left| u_{NN}(\boldsymbol{\xi}_j^d; \boldsymbol{\theta}) - \hat{u}_j \right|^2, \end{aligned} \tag{4.8}$$

where the terms with superscript d represent those associated with the given observed data $\{\hat{u}_j\}$.

The only difference between Equations (4.3) and (4.8) is the inclusion of the data loss term. Also, part of the system parameters, $\boldsymbol{\lambda}$ are now freed as trainable variables such that the resulting model output describes the observed data $\{\hat{u}_j\}$ well. This ease of switching between the two types of problems by simply modifying the loss function is another advantage of using the PINN framework.

The number of sampled points per domain varied from 250 to 1250 for those sampled along the boundary, and from 500 to 1500 for those sampled within the domain.

4.5 Optimization method

The parameters that minimize the loss functions defined in Section 4.4 are found by using the Adam optimizer (Kingma & Ba, 2014). However, a closer examination of the loss functions reveals a serious problem that complicates the optimization process – the problem of choosing the right weights.

The loss functions, Equations (4.3) and (4.8), are constructed as the weighted sum of various terms coming from different boundary (or initial) conditions, governing equations, and observed data. The weight of each term can be thought as deciding the priority during the optimization process. A term with relatively small weight may be sacrificed in favor of other terms with relatively large weights. This is because in the gradient-based optimization algorithm, the weight serves as a sort of individual learning rate for each of the terms that make up the overall loss function. Therefore, the choice of weight values is critical to successful optimization. Since there are tens to hundreds of different weight terms, it is almost impossible to find the optimal set of weights by trial and error.

To solve this problem, we used an adaptive weighting scheme based on the *neural tangent kernels* (NTKs), as suggested by Wang *et al.* (2021). The essence of the method is in the NTKs' ability to capture the training dynamics of NNs. According to the authors, the eigenvalues of NTKs are directly related to the convergence rate of each component in the loss function. By using those values to determine the weight for each term, it is possible to obtain a similar convergence rate for all of the terms, leading to a successful optimization.

Figure 4.7 shows the y-component of the velocity as predicted by the trained PINNs. It is evident from the figure that when fixed weight values are used, the trained PINN fails to satisfy the given boundary conditions. When adaptive weighting scheme is applied, the boundary conditions are satisfied more strictly.

4.6 Results and discussion

To demonstrate the effectiveness of the method developed in this chapter, we solve two illustrative problems with partially missing data.

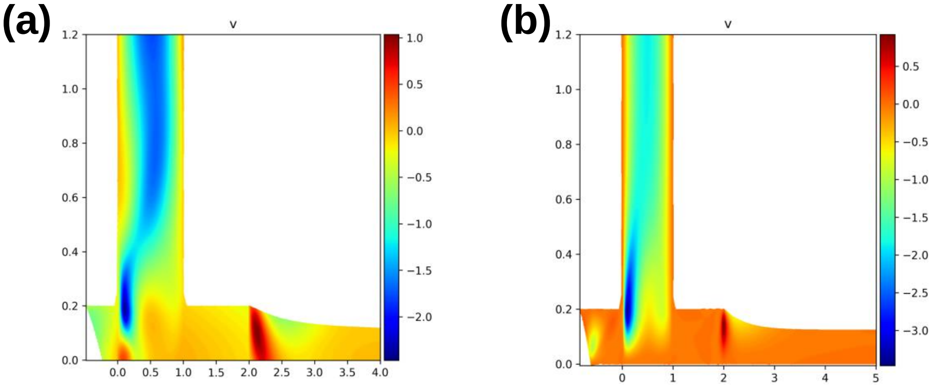

Figure 4.7: y-component of the velocity predicted by the trained PINN after the same number of iterations (a) with a fixed weights, (b) with an adaptive weight based on NTKs.

4.6.1 Problem 1: missing physics

As shown in Figures 2.5 and 3.3(b), a Navier-slip boundary condition is applied at the dynamic contact line, which is expressed as follows:

$$\frac{1}{\beta}\mathbf{t}_{\mathrm{w}} \cdot (\mathbf{u} - U\mathbf{t}_{\mathrm{w}}) = \mathbf{t}_{\mathrm{w}} \cdot (\mathbf{n}_{\mathrm{w}} \cdot \mathbf{T}), \tag{4.9}$$

where $\mathbf{t}_{\mathrm{w}}$ and $\mathbf{n}_{\mathrm{w}}$ are the local unit basis vectors parallel and normal to the moving substrate.

Without this boundary condition, a contradiction occurs because the upstream meniscus has to be stationary with respect to the slot-die, while being attached to the moving substrate on the dynamic contact line. This makes the slot coating flow problem impossible to solve using conventional methods without the slip condition.

In this section, we assume that we are unaware of the physics that occurs in this region. To model this situation, the Navier-slip condition is deliberately neglected while solving the given problem. We use physics-informed machine learning framework to train a PINN to model the given flow, since the framework can still be applied even when some boundary terms are missing from the total loss function. Rest of the boundary conditions, together with the governing equations are correctly included into the corresponding loss function, Equation (4.3). The parameters used in this analysis are summarized in Table 4.1.

Table 4.1: Operating parameters considered in the analysis.

Operating parameters	Unit	Value
Density (ρ)	$\mathrm{g/mm^3}$	0.001
Surface tension (σ)	$\mathrm{mN/m}$	70
Substrate speed (U_{w})	$\mathrm{mm/s}$	10
Static contact angle (θ_{s})	$^\circ$	30
Dynamic contact angle (θ_{d})	$^\circ$	120
Wet thickness(h)	mm	0.125
Viscosity (μ)	$\mathrm{Pa \cdot s}$	0.1
Geometric parameters	**Unit**	**Value**
Upstream die lip length (L_{u})	mm	1.0
Downstream die lip length (L_{d})	mm	1.0
Feed slot height (L_{fh})	mm	1.0
Feed slot length (L_{fl})	mm	1.0
Coating gap (H_{g})	mm	0.2

To assess the accuracy of the PINN prediction, we solved the problem with the Navier-slip condition included, by using 2-D finite element method (FEM) based computational model. The result of two models are compared along the horizontal cross-section of $y = h_{\mathrm{w}}/2$, as shown in Figure 4.8.

The prediction of field variables made by PINN, along with the reference from 2-D FEM computation are shown in Figure 4.9. The PINNs are trained for 25,000 it-

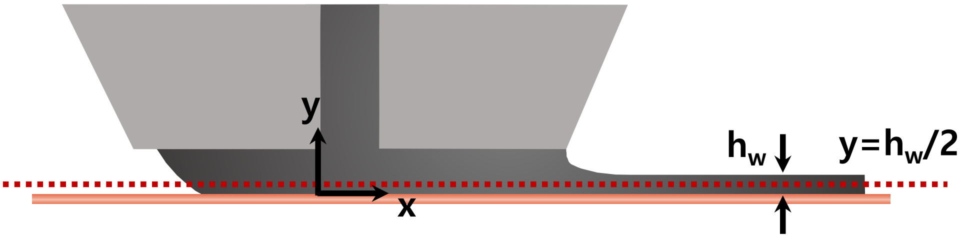

Figure 4.8: Cross-section for assessing the accuracy of predicted field variables.

erations, and the results were averaged from the networks trained with 5 independent parameter initialization using a Glorot normal initializer (Glorot & Bengio, 2010). Despite a slight deviation observed near the upstream meniscus region, the results generally show a good agreement between the two models, despite the absence of Navier-slip condition during the training of PINNs. This observation demonstrates the potential of PINN framework in solving slot coating flow problems, even when the physics governing the flow is not fully understood. However, caution should still be exercised when applying this method to other cases of missing physics, as the result may vary depending on the significance of the missing term in the system of interest.

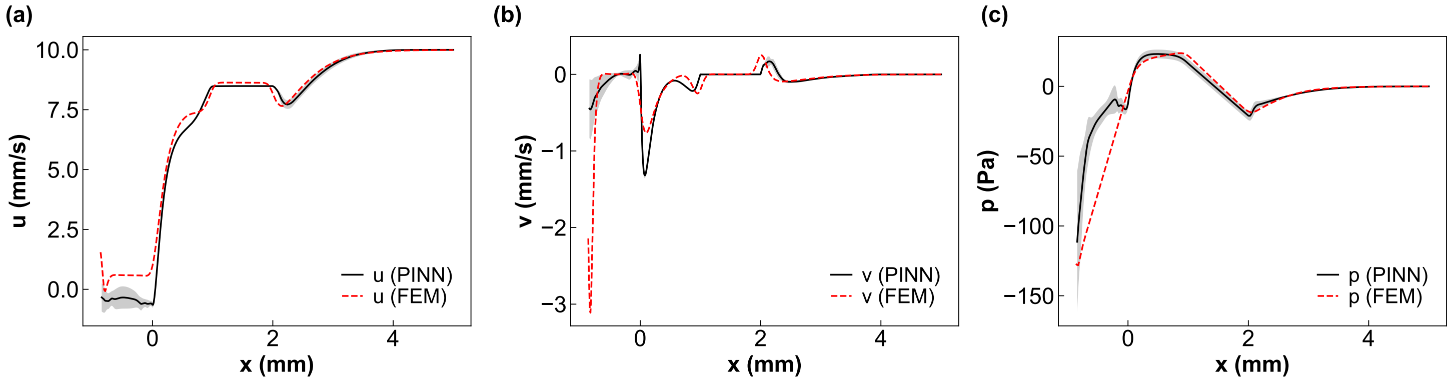

Figure 4.9: (a) x-component of velocity, (b) y-component of velocity, and (c) pressure fields predicted by using PINN (black solid line) and 2-D FEM (red dashed line). The solid line represents the average of results from 5 independent initializations of network parameters, and the shaded area represents one standard deviation away from the mean.

4.6.2 Problem 2: missing data

In this section, we turn our attention to solving the problem with partially missing data. Figure 4.10(a) shows a schematic of visualizing the coating bead flow from the side-view. A clear image of the side-view of a coating bead flow obtained experimentally can provide many valuable information on the flow, such as the contact angle values and the curvature of liquid-gas interfaces. However, due to the fluctuation in the coating gap and flow rate as well as the variation in the widthwise direction, it is often hard to determine the values of interests out of the obtained image, as shown in Figure 4.10(b).

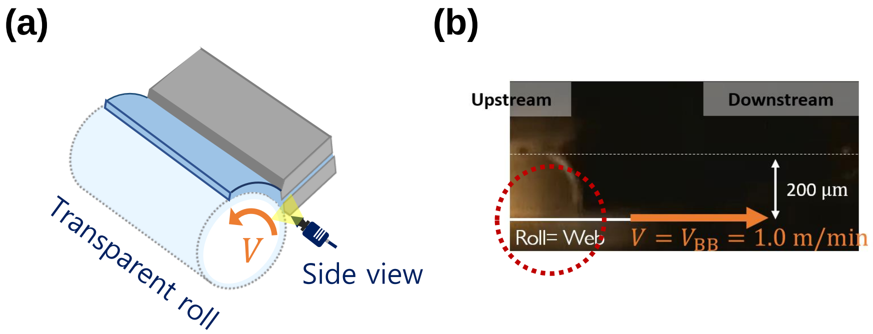

Figure 4.10: (a) Flow visualization setup for obtaining side-view images of coating bead flows. (b) Side-view of coating bead flow showing the upstream region of the flow (Photo courtesy of Jihwan Yoon).

In this section, we apply physics-informed machine learning to solve a slot coating flow problem when given the observed data. The goal is to obtain the dynamic contact angle from the given image data on the meniscus shape and position. The experimental image data is replaced by the artificial data of upstream meniscus shape and position, computed by solving a slot coating flow with all the parameters values given. The uncertainty in the experimental image data is modeled by deliberately omitting the given data in parts, as depicted in Figure 4.11. We varied the amount of data that is omitted during the training, in order to examine the effect of uncertainty in the data on the performance of PINNs.

Associated boundary conditions and governing equations, as described in Section 4.4 are substituted into Equation (4.8) to form the loss function. The given data on the shape and position of the meniscus is substituted into the data loss term of the same equation. In this case, the system parameter, $\boldsymbol{\lambda}$, subject to optimization is the dynamic contact angle, which is initialized as 90°.

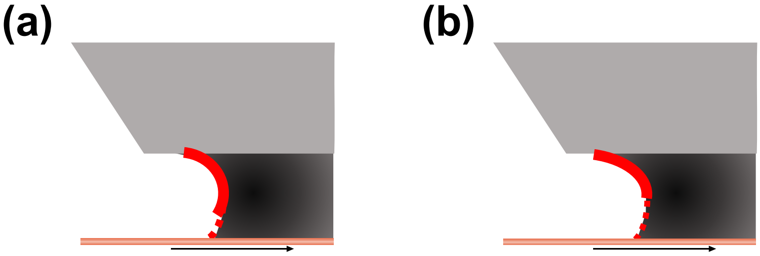

Figure 4.11: Uncertainty in the image data is modeled by deliberately omitting (a) 25% and (b) 50% of the given data on meniscus shape and position.

The prediction of the dynamic contact angle as optimization proceeds is shown in Figure 4.12. As with the problem considered in the previous section, the result is obtained as an average of 5 PINNs initialized independently. When 25% of the given data was missing, the relative errors of the prediction at the end of the iterations was 7.8%, showing that the PINN solved the given problem satisfactorily, even with the given data partially missing. Moreover, as can be seen from the shaded area in Figure 4.12, the predictions made by the PINNs with different initializations of the network parameters all converge to a single value, demonstrating the robustness of the method. The relative error for the 50% of data missing case was 17.2% at the end of the training. This can be viewed as a large error, but considering that half of the data needed to solve the problem is missing, this magnitude of error may be acceptable in certain cases where obtaining high quality data is challenging.

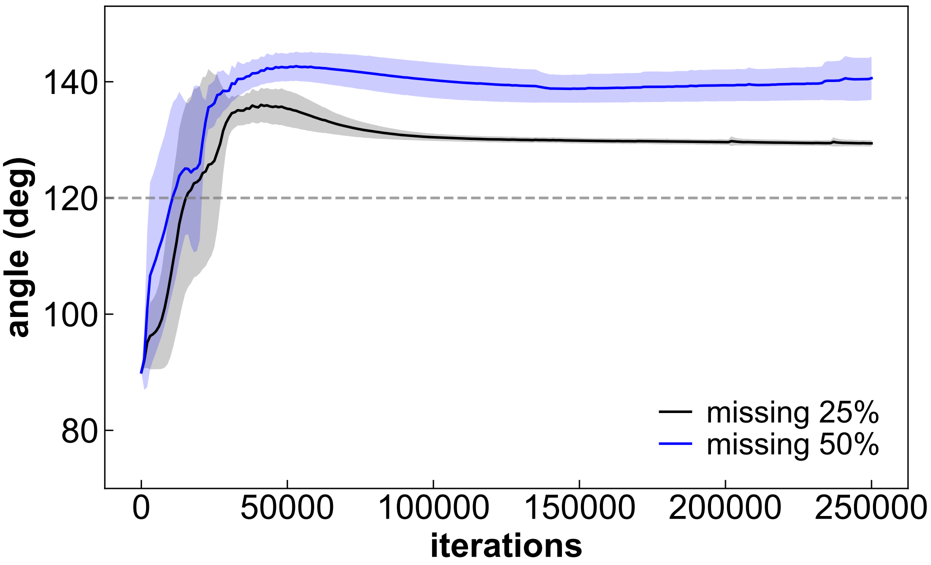

Figure 4.12: Dynamic contact angle predicted by PINN when only a part of the data is given. The solid line represents the average of results from 5 independent initializations of network parameters, and the shaded area represents one standard deviation away from the mean.

4.7 Conclusions

In this chapter, the slot coating flow problems posed under situations where the given data is missing, were solved by using physics-informed machine learning. To model the slot coating flow, which is a free-surface flow, a specialized neural network architecture, comprised of two separate networks was used. The domain was also decomposed into several subdomains modeled by individual neural networks. The values of the weights for individual terms comprising the total loss function were determined automatically through a neural tangent kernel based adaptive weighting scheme, such that the rate of convergence of each terms were maintained at a similar level throughout the optimization.

The method was first applied to solving a problem when the physics governing the slot coating flow is partially missing. To model such a situation, the Navier-slip condition at the dynamic contact line was deliberately omitted from the loss function. The results showed that the trained networks were able to capture the dynamics of the flow even with the absence of the boundary condition.

The method was then applied to solving a problem of obtaining the dynamic contact angle from the given data on the meniscus. Part of the data was intentionally excluded to model the obscurity often observed in the image data. The results showed that the networks were able to predict the dynamic contact angle to a satisfactory degree even with the partially missing data.

Despite the success in solving the two illustrative problems, caution should be exercised when applying the proposed method in other cases, as the performance may vary depending on the significance of the missing parts of the data. In addition, optimization of hyperparameters such as the network width and depth, initialization scheme, and activation functions, needs to be performed in future works, in order to explore the room for improvement in the performance of the proposed method.

Chapter 5

Concluding remarks

In this thesis, a number of slot coating flow problems are solved by using various methods and flow models. The main objective of the thesis was to broaden the scope of the techniques available for solving problems in slot coating flows by tackling previously unsolved problems and applying previously unexplored methods. The new findings and novelties in each of the chapters can be summarized as follows.

In Chapter 2, we explored the effect of varying the coating gap on the maximum and minimum wet thicknesses under three different slot-die configurations. A previously unobserved trend was highlighted during the analysis, and the reason behind it was explained analytically through the use of a simple one-dimensional flow model.

In Chapter 3, an analytical criterion for the vortex formation in slot coating flows previously only known for the Newtonian fluids was extend to the power-law fluids through a one-dimensional flow analysis. The derived expression could successfully explain the trend observed in the two-dimensional finite element method based computation results. The method was further generalized to the cases of generalized Newtonian fluids, and a systematic procedure for obtaining the exact values of the criteria was also developed and presented.

In Chapter 4, a machine learning method was applied to the analysis of slot coating flow for the first time, and its potential for solving various problems with missing data was explored through illustrative examples. A specialized network architecture was applied to take care of the liquid-gas interfaces of the coating bead flow. The results showed that the proposed novel method was capable of solving the problems to a satisfactory degree even when the physics governing the problem or the given data for solving the problem is partially missing.

Bibliography

CAI, SHENGZE, WANG, ZHICHENG, WANG, SIFAN, PERDIKARIS, PARIS & KARNIADAKIS, GEORGE EM 2021 Physics-informed neural networks for heat transfer problems. *Journal of Heat Transfer* **143** (6).

CARVALHO, MARCIO S & KHESHGI, HAROON S 2000 Low-flow limit in slot coating: Theory and experiments. *AIChE Journal* **46** (10), 1907–1917.

CHIN, CHIH-PING, WU, HO-SHING & WANG, SHAW S 2010 Improved coating window for slot coating. *Industrial & Engineering Chemistry Research* **49** (8), 3802–3809.

COX, R. G. 1986 The dynamics of the spreading of liquids on a solid surface. part 1. viscous flow. *Journal of Fluid Mechanics* **168**, 169–194.

CRUZ, DA, COELHO, PM & ALVES, MA 2012 A simplified method for calculating heat transfer coefficients and friction factors in laminar pipe flow of non-newtonian fluids. *Journal of Heat Transfer* **134** (9).

CUOMO, SALVATORE, DI COLA, VINCENZO SCHIANO, GIAMPAOLO, FABIO, ROZZA, GIANLUIGI, RAISSI, MAZIAR & PICCIALLI, FRANCESCO 2022 Scientific machine learning through physics–informed neural networks: where we are and what's next. *Journal of Scientific Computing* **92** (3), 88.

DIEHM, RALF, KUMBERG, JANA, DÖRRER, CHRISTOPHER, MÜLLER, MARCUS, BAUER, WERNER, SCHARFER, PHILIP & SCHABEL, WILHELM 2020 In situ investigations of simultaneous two-layer slot die coating of component-graded anodes for improved high-energy li-ion batteries. *Energy Technology* **8** (5), 1901251.

DING, XIAOYU, LIU, JIANHUA & HARRIS, TEQUILA AL 2016 A review of the operating limits in slot die coating processes. *AIChE Journal* **62** (7), 2508–2524.

FLUMERFELT, RW, PIERICK, MW, COOPER, STUART L & BIRD, RB 1969 Generalized plane Couette flow of a non-Newtonian fluid. *Industrial & Engineering Chemistry Fundamentals* **8** (2), 354–357.

GATES, IAN D. 1999 Slot coating flows: feasibility, quality. PhD thesis, University of Minnesota, MN, USA.

GLOROT, XAVIER & BENGIO, YOSHUA 2010 Understanding the difficulty of training deep feedforward neural networks. In *Proceedings of the thirteenth international conference on artificial intelligence and statistics*, pp. 249–256. JMLR Workshop and Conference Proceedings.

HAGHIGHAT, EHSAN, RAISSI, MAZIAR, MOURE, ADRIAN, GOMEZ, HECTOR & JUANES, RUBEN 2021 A physics-informed deep learning framework for inversion and surrogate modeling in solid mechanics. *Computer Methods in Applied Mechanics and Engineering* **379**, 113741.

HIGGINS, BRIAN G & SCRIVEN, LAWRENCE E 1980 Capillary pressure and viscous pressure drop set bounds on coating bead operability. *Chemical Engineering Science* **35** (3), 673–682.

HONG, HYEYOUNG & NAM, JAEWOOK 2017 Automatic detection of contact lines in slot coating flows. *AIChE Journal* **63** (6), 2440–2450.

JAGTAP, AMEYA D & KARNIADAKIS, GEORGE E 2021 Extended physics-informed neural networks (xpinns): A generalized space-time domain decomposition based deep learning framework for nonlinear partial differential equations. In *AAAI Spring Symposium: MLPS*, pp. 2002–2041.

JI, HO SUK, AHN, WON-GI, KWON, ILYOUNG, NAM, JAEWOOK & JUNG, HYUN WOOK 2016 Operability coating window of dual-layer slot coating process using viscocapillary model. *Chemical Engineering Science* **143**, 122–129.

JIN, XIAOWEI, CAI, SHENGZE, LI, HUI & KARNIADAKIS, GEORGE EM 2021 Nsfnets (navier-stokes flow nets): Physics-informed neural networks for the incompressible navier-stokes equations. *Journal of Computational Physics* **426**, 109951.

KIM, ONYU & NAM, JAEWOOK 2017 Confinement effects in dip coating. *Journal of Fluid Mechanics* **827**, 1–30.

KINGMA, DIEDERIK P & BA, JIMMY 2014 Adam: A method for stochastic optimization. *arXiv preprint arXiv:1412.6980* .

KISTLER, STEPHAN F. & SCHWEIZER, PETER M. 1997 *Liquid Film Coating*. Chapman & Hall.

KOH, HYUN JUNG, KWON, ILYOUNG, JUNG, HYUN WOOK & HYUN, JAE CHUN 2012 Operability window of slot coating using viscocapillary model for carreau-type coating liquids. *Korea-Australia Rheology Journal* **24**, 137–141.

LANDAU, L. & LEVICH, B. 1942 Dragging of a liquid by a moving plate. *Acta Physicochim. URSS* **17**, 42.

LEE, KWONG-YANG, LIU, LI-DAH & LIU, TA-JO 1992 Minimum wet thickness in extrusion slot coating. *Chemical Engineering Science* **47** (7), 1703–1713.

LEE, SEMI & NAM, JAEWOOK 2015*a* Analysis of slot coating flow under tilted die. *AIChE Journal* **61** (5), 1745–1758.

LEE, SEMI & NAM, JAEWOOK 2015*b* Response of slot coating flow to gap disturbances: effects of fluid properties, operating conditions, and die configurations. *Journal of Coatings Technology and Research* **12**, 949–958.

LEE, SI HYUNG, KOH, HYUN JUNG, RYU, BO KYUNG, KIM, SEE JO, JUNG, HYUN WOOK & HYUN, JAE CHUN 2011 Operability coating windows and frequency response in slot coating flows from a viscocapillary model. *Chemical Engineering Science* **66** (21), 4953–4959.

LI, JIANLIN, FLEETWOOD, JAMES, HAWLEY, W BLAKE & KAYS, WILLIAM 2021 From materials to cell: State-of-the-art and prospective technologies for lithium-ion battery electrode processing. *Chemical Reviews* **122** (1), 903–956.

LIM, SANGHYUK, AHN, KYUNG HYUN & YAMAMURA, MASATO 2013 Latex migration in battery slurries during drying. *Langmuir* **29** (26), 8233–8244.

MACOSKO, CHRISTOPHER W. 1994 *Rheology: Principles, Measurements, and Applications*. Wiley-VCH.

MALIK, RAJEEV & SHENOY, UDAY V 1991 Generalized annular couette flow of a power-law fluid. *Industrial & Engineering Chemistry Research* **30** (8), 1950–1954.

NAM, JAEWOOK & CARVALHO, MARCIO S 2009 Mid-gap invasion in two-layer slot coating. *Journal of Fluid Mechanics* **631**, 397–417.

NAM, JAEWOOK, SCRIVEN, LE & CARVALHO, MARCIO S 2009 Tracking birth of vortex in flows. *Journal of Computational Physics* **228** (12), 4549–4567.

PATIDAR, RAHUL, BURKITT, DANIEL, HOOPER, KATHERINE, RICHARDS, DAVID & WATSON, TRYSTAN 2020 Slot-die coating of perovskite solar cells: An overview. *Materials Today Communications* **22**, 100808.

RAISSI, MAZIAR, PERDIKARIS, PARIS & KARNIADAKIS, GEORGE E 2019 Physics-informed neural networks: A deep learning framework for solving forward and inverse problems involving nonlinear partial differential equations. *Journal of Computational physics* **378**, 686–707.

ROMERO, OJ & CARVALHO, MS 2008 Response of slot coating flows to periodic disturbances. *Chemical Engineering Science* **63** (8), 2161–2173.

ROSS, AB, WILSON, SK & DUFFY, BR 1999 Blade coating of a power-law fluid. *Physics of Fluids* **11** (5), 958–970.

RUSCHAK, KENNETH J 1976 Limiting flow in a pre-metered coating device. *Chemical Engineering Science* **31** (11), 1057–1060.

SAHLI COSTABAL, FRANCISCO, YANG, YIBO, PERDIKARIS, PARIS, HURTADO, DANIEL E & KUHL, ELLEN 2020 Physics-informed neural networks for cardiac activation mapping. *Frontiers in Physics* **8**, 42.

DE SANTOS, J.M. 1991 Two-phase cocurrent downflow through constricted passages. PhD thesis, University of Minnesota, MN, USA.

SARTOR, LUIGI 1990 Slot coating: Fluid mechanics and die design. PhD thesis, University of Minnesota, MN, USA.

SCHMITT, MARCEL, DIEHM, RALF, SCHARFER, PHILIP & SCHABEL, WILHELM 2015 An experimental and analytical study on intermittent slot die coating of viscoelastic battery slurries. *Journal of Coatings Technology and Research* **12**, 927–938.

SCHMITT, MARCEL, SCHARFER, PHILIP & SCHABEL, WILHELM 2014 Slot die coating of lithium-ion battery electrodes: investigations on edge effect issues for stripe and pattern coatings. *Journal of Coatings Technology and Research* **11** (1), 57–63.

SCHOO, ALEXANDER, MOSCHNER, ROBIN, HÜLSMANN, JENS & KWADE, ARNO 2023 Coating defects of lithium-ion battery electrodes and their inline detection and tracking. *Batteries* **9** (2), 111.

SOCHI, TAHA 2015 Analytical solutions for the flow of carreau and cross fluids in circular pipes and thin slits. *Rheologica Acta* **54** (8), 745–756.

WAMBA, SAMUEL FOSSO, AKTER, SHAHRIAR, EDWARDS, ANDREW, CHOPIN, GEOFFREY & GNANZOU, DENIS 2015 How 'big data'can make big impact: Findings from a systematic review and a longitudinal case study. *International Journal of Production Economics* **165**, 234–246.

WANG, SIFAN, TENG, YUJUN & PERDIKARIS, PARIS 2021 Understanding and mitigating gradient flow pathologies in physics-informed neural networks. *SIAM Journal on Scientific Computing* **43** (5), A3055–A3081.

YANG, CK, WONG, DSH & LIU, T-J 2004 The effects of polymer additives on the operating windows of slot coating. *Polymer Engineering & Science* **44** (10), 1970–1976.

YIN, SHEN & KAYNAK, OKYAY 2015 Big data for modern industry: challenges and trends [point of view]. *Proceedings of the IEEE* **103** (2), 143–146.

YOON, JIHWAN, KIM, DONGJAE, LEE, SEUNG-HYUN, KANG, DONGJOON & NAM, JAEWOOK 2022 Simplified model for operability window of slot coating without vacuum. *Chemical Engineering Science* **259**, 117766.

ZANG, YONG-HUA, DU, JUAN, DU, YANFEN, WU, ZHENJUAN, CHENG, SHAOLING & LIU, YUPING 2010 The migration of styrene butadiene latex during the drying of coating suspensions: when and how does migration of colloidal particles occur? *Langmuir* **26** (23), 18331–18339.

국문 초록

슬롯 코팅 공정은 움직이는 기판 위에 얇은 액체 필름 층을 높은 정밀도로 코팅하기 위한 대표적인 방법으로, 그 다재다능함 덕분에 광학 필름, 태양 전지, 배터리 전극 등 다양한 고부가가치 필름 제품을 제조하기 위한 많은 산업에서 이용되고 있다. 슬롯 코팅 공정은 크게 용액 준비, 도포, 그리고 건조의 세 가지 주요 단계로 이루어져 있으며, 본 논문에서는 이 중 도포 단계에서 발생하는 코팅 유동에 초점을 맞추어 진행한 연구들을 다루고자 한다.

슬롯 코팅 유동은 2차원으로 근사가능한 유동으로 두개의 기-액 계면으로 둘러쌓여 있는 형태를 띤다. 해당 유동은 다양한 조절 가능한 인자를 가지고 있는데, 이러한 인자들에 대해 적절한 제어가 이루어져야 공정을 안정적으로 운용하여 불량 없이 높은 품질의 필름 제품을 생산할 수 있다. 공정 관련 인자들의 최적값을 알아내는 과정은 슬롯 코팅 유동과 관련된 다양한 설계 문제를 해결하는 것으로부터 시작된다.

슬롯 코팅 공정의 유동 문제를 푸는 첫번째 목적은 공정 관련 인자값들이 주어졌을 때 해당 인자들로 인하여 발생하는 유동의 양상이 어떠한지를 파악하는 것이다. 이를 통해 특정 공정 인자값 하에서 발생하는 유동의 유불리를 판단할 수 있게 된다. 이와 반대로 유동 양상과 관련된 정보나 제약조건이 미리 주어져 있는 상황에서 해당 유동 양상을 보이도록 하는 공정 인자값을 찾는 것을 목표로 할 수도 있다. 이렇듯 다양한 설계 문제 해결을 통해 슬롯 코팅 공정에 대한 높은 이해를 얻을 수 있고, 이를 바탕으로 높은 품질의 필름 제품을 생산하기 위한 공정을 설계할 수 있게 된다.

본 논문에서는 기존에 다루지 않았던 문제들과 사용되지 않았던 분석 방법들을 제시함으로써 슬롯 코팅 공정의 다양한 설계문제 해결을 위한 시각을 넓히고자 한다. 본 논문의 2장에서는 슬롯 다이의 형상에 따라 최대 최소 젖음두께가 코팅 갭에 의존하는 양상이 어떻게 달라지는지를 단순 유동 모델을 통해 분석하고자

한다. 이러한 분석을 통해 코팅갭이 증가함에도 최대 코팅 가능 두께가 오히려 감소하는 특수한 현상이 일어나는 이유에 대해서 파악해본다. 본 논문의 3장에서는 슬롯 코팅 유동 내부에 발생하는 와류의 생성 조건을 얻고자 한다. 해당 연구에서는 다양한 유동 모델을 사용하여 전단율에 비례하는 점도를 가진 코팅액이 사용되었을 때 와류 발생 조건이 어떻게 되는지를 수치적 그리고 해석적으로 분석해본다. 마지막으로 4장에서는 슬롯 코팅 유동을 모델링하기 위한 물리 정보 신경망 기반 기계학습 방법에 대하여 다루고자 한다. 해당 방법을 이용하여 몇가지 대표적인 예시 문제들을 해결함으로써 주어진 데이터가 일부 누락된 상황에서도 유연하게 잘 작동하는 분석 방법에 대해 알아본다.

주요어: 슬롯 코팅 공정, 일반 뉴턴 유체, 유한요소법, Couette-Poiseuille 유동, 물리 정보 신경망

학번: 2018-28363